Plasma Sources Science and
Technology

PAPER

Comparison of laser induced breakdown spectroscopy and fast ICCD imaging for spatial and time resolved measurements of atmospheric pressure helium plasma jet

To cite this article: Dejan Maletić *et al* 2022 *Plasma Sources Sci. Technol.* **31** 025011

IOP Publishing Plasma Sources Science and Technology
Plasma Sources Sci. Technol. **31** (2022) 025011 (10pp) https://doi.org/10.1088/1361-6595/ac4ddd

Comparison of laser induced breakdown spectroscopy and fast ICCD imaging for spatial and time resolved measurements of atmospheric pressure helium plasma jet

Dejan Maletić[1,2,*], Dean Popović[2], Nevena Puač[1], Zoran Lj Petrović[3,4] and Slobodan Milošević[2]

[1] Institute of Physics, University of Belgrade, Pregrevica 118, 11000 Belgrade, Serbia
[2] Institute of Physics, Bijenička 46, 10000 Zagreb, Croatia
[3] Serbian Academy of Sciences and Arts, Knez Mihajlova 35, 11001 Belgrade, Serbia
[4] School of Engineering, Ulster University, Jordanstown, Co. Antrim, BT37 0QB, United Kingdom

E-mail: dejan_maletic@ipb.ac.rs and dmaletic@ifs.hr

Received 21 October 2021, revised 13 December 2021
Accepted for publication 21 January 2022
Published 17 February 2022

Abstract

In this paper we compared the fast Intensified Charge Coupled Device (ICCD) imaging with the newly developed diagnostic method that utilizes laser induced breakdown in plasma jet. Our helium plasma jet was powered by an 80 kHz high-voltage sine wave and propagated into the ambient air. Pulsed laser beam 1064 nm (4 ns pulse duration and 5 Hz repetition rate) was focused with the lens into the plasma jet at energy below breakdown threshold in helium. Laser pulses and the jet powering signal were synchronized. Laser induced plasma is highly dependent on the concentration of seed electrons and other charged particles in the plasma jet channel. We compared the radial profiles of the plasma jet obtained with these two methods. For laser induced breakdown it was ±0.5 mm and for ICCD measurement it was ±1.75 mm, while the ionization wave velocities obtained with these two methods were 15 km s^{-1} and 20 km s^{-1} respectively. Electrical characteristics of the plasma jet were also presented and one can see a large hysteresis effect when the applied power to the plasma jet was reducing. We show that the laser induced breakdown spectroscopy can be used as a complementary diagnostics technique with ICCD measurements.

Keywords: DBD plasma jet, laser induced plasma, LIP, ICCD imaging, helium plasma jet

(Some figures may appear in colour only in the online journal)

1. Introduction

Atmospheric pressure plasma jets (APPJs) attract a lot of attention due to their great range of possible applications especially in biotechnologies and medicine [1]. The primary requirement for treatments of living cells and tissues is the non-equilibrium nature of those plasmas. Due to a variety of specific applications, it is necessary to study in detail all physical and chemical processes, both in the plasma jet itself and in its interaction with the treated samples. To solve these complex problems many diagnostics techniques are used such as optical emission spectroscopy (OES), mass spectrometry, Schlieren imaging, laser induced fluorescence (LIF), electrical probe measurements, cavity ring down spectroscopy [2–6]. From the fast ICCD imaging it was found that plasma jets are not continuous but consist of fast-moving self-propagating ionization waves (IWs). The head of the plasma jet is loaded with a high concentrations of highly reactive species. The most important reactive

---

[*] Author to whom any correspondence should be addressed.

species in plasma jets are reactive oxygen nitrogen species (RONS), ions, electrons and UV radiation. Commonly used gases as flowing buffers for plasma jets are helium and argon [7–10]. The main RONS are hydroxyl radical $^{\bullet}$OH, ozone O_3, NO_x, N_2^+, O^- and others [8, 11, 12]. A large percentage of research in plasma medicine is done by using plasma jets, because of their simple construction and flexible range of operating parameters. Plasma jets are used for bacteria sterilization, carcinoma cell treatment, blood coagulation and other [13–15]. Treatment by a single plasma jet is usually limited to 1 cm^2, so for larger surfaces, plasma jets can be connected in arrays of several identical plasma jets [16–18]. One of the new emerging fields in plasma jet applications is treatment of water and production of plasma activated water [12, 19–22] or medium [23, 24].

Medical and biotechnology applications of plasmas [25, 26] have opened a large activity in the field and it became necessary to understand those plasmas better in order to interpret and optimize those applications. Having in mind all the difficulties encountered in diagnostics of atmospheric pressure plasmas each new result is valuable especially when more than one technique has been applied and results are tested for consistency.

In this work we compared two very different plasma diagnostic techniques. The first is broadband fast ICCD imaging that is a non-perturbing technique and the second laser induced breakdown spectroscopy (LIBS) that is the opposite, a perturbing technique. Laser induced breakdown in gases has been studied in the first decades of laser applications, followed by the development of LIBS, a versatile technique for elemental analysis of solid materials [27, 28], as well as liquid [29] and gas/aerosols [30]. For the breakdown to occur in a gas, a critical electron density needs to be reached in the laser focal volume. For relatively lower laser intensities, this can occur via two processes, multiphoton ionization and laser induced avalanche ionization. In general, the individual contribution of those two processes depends on the laser wavelength and pulse duration. Using shorter wavelengths and shorter pulses leads to higher probability of multiphoton ionization to occur (especially with femtosecond lasers). In contrast to that, laser induced avalanche ionization favours longer pulses further in the infrared. Most importantly, this is a process that involves free electrons and is thus an ideal candidate for their detection. Theoretically, the process begins with a certain low electron density (at least a single electron) in the laser focal volume, which is then increased by a repeated inverse bremsstrahlung and electron impact ionization [31]. The detection threshold (lowest electron density detectable) can easily be changed by changing the laser pulse energy, so the occurrence of a laser induced plasma (LIP) corresponds to a certain electron density at the beginning of the laser pulse. This concept was first shown in a publication by Popović *et al* where a nanosecond Nd:YAG laser was used to detect free electrons in a helium APPJ via laser induced avalanche ionization [32]. More recently, Woodbury *et al* showed that low concentrations of charged species can be probed by using a picosecond mid-infrared laser for avalanche ionization breakdown of air [33]. The charged species were a result of nearby radioactive source. The authors also discussed the implementation of this technique for low-density plasma detection.

Here we will show similarities and differences of these two techniques for the plasma jet diagnostics. For example, one of the first observables to be recorded in such plasmas were the velocities of propagation of ionization fronts. Those are considerably different from the plasma flow velocities and are a projection of the space charge formation and propagation. Most of the results were obtained by using ICCD and there is wealth of data on how these velocities vary with different parameters [34–37]. Here we compared the ICCD data to those obtained by the laser induced breakdown measurements for sinewave excitation signal.

2. Experimental setup

In this paper we used two experimental setups, the first setup was for the LIBS experiment (see figure 1(a)) and the second setup for the ICCD measurements (see figure 1(b)). There are some differences in the used experimental equipment between these two experiments because they are performed in collaboration of two laboratories. The differences are such that they cannot affect the nature of the final results. The plasma jet electrode configuration and power supply for the plasma jet are the same. ICCD measurements were carried out at the Institute of Physics in Belgrade (Serbia) and the experiment on the LIBS in plasma jet was performed at the Institute of Physics in Zagreb (Croatia). Plasma jet is made of a capillary glass tube with the inner diameter (I.D.) of 1 mm and the outer diameter of 6 mm. The two external electrodes were made of copper foil wrapped around the glass tube. The width of the electrodes, the electrode gap and the distance of the first electrode from the edge of the glass tube were all 10 mm. The electrode closer to the plasma jet nozzle was connected to the high voltage power supply. The second electrode was connected to the ground through a resistor of 100 kΩ. The high voltage power supply was modular and consisted of the signal generator (PeakTech DDS Function Generator 4025 used for ICCD measurements and Keysight Arbitrary Waveform Generator 33522B used in laser measurements), custom made amplifier and a high voltage transformer. The operating frequency of the plasma jet was 80 kHz (unit time cycle 12.5 micro-seconds). High purity helium 5.0 (99.999%, Messer) was used as the working gas. The flow rate of 2 l min^{-1} of the working gas was set by a mass flow controller (Bronkhorst MASS-VIEW® MV-196-HE or Alicat MC-5SLPM-D). The electrical properties of the discharge were measured by high voltage (Tektronix P6015A, 75 MHz bandwidth) and current (Pearson 2877) probes. Waveforms were acquired by oscilloscope (Picoscope 5244B). LIP was produced by a Q-switched Nd-YAG laser at 1064 nm (Quantel Brilliant, pulse width 4 ns) operating typically at the repetition rate of 5 Hz. Polarizing beam splitter cube (CCM1-PBS25-1064-HP/M, Thorlabs) was used for attenuation of the laser power. Laser beam was focused on the helium plasma jet at 5 mm below the capillary nozzle using a fused silica lens with antireflection coating (focal length 5 cm, diameter 2.5 cm). For the laser energy measurement, we used laser

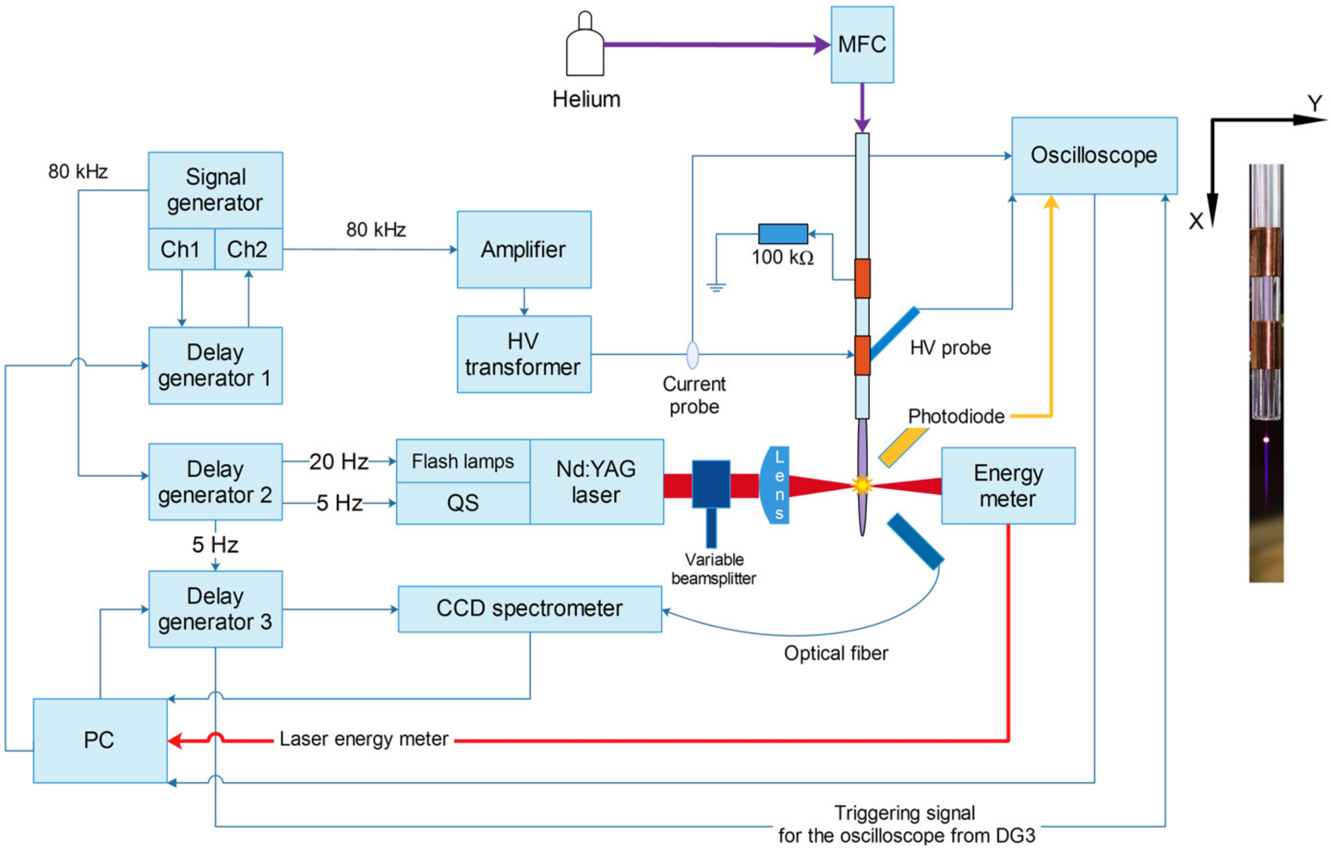
(a) LIBS - experimental setup I

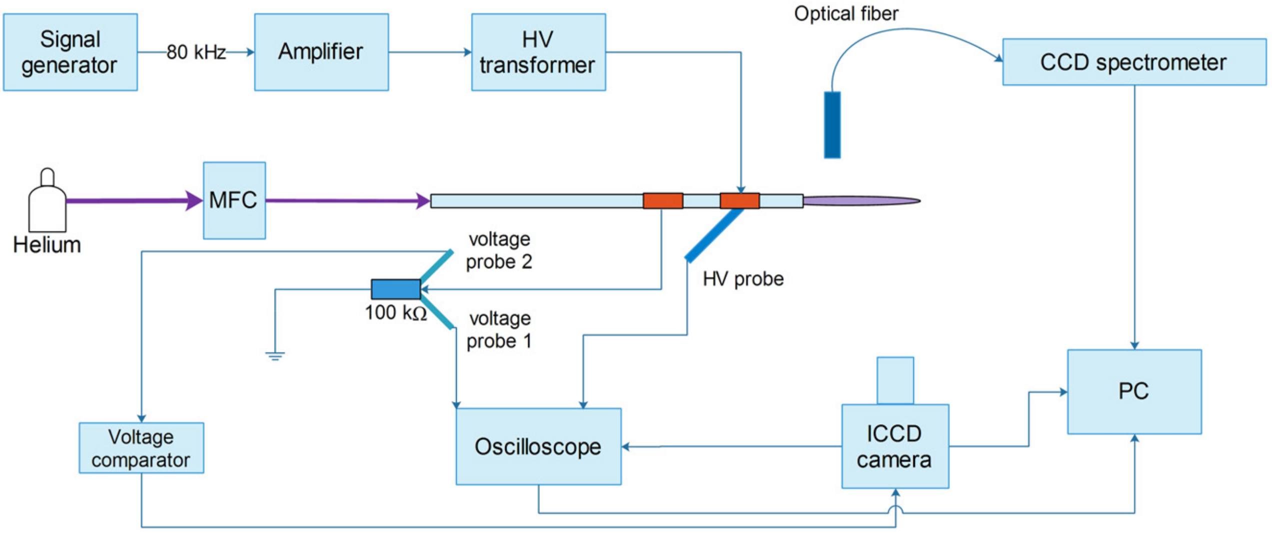
(b) ICCD - experimental setup II

Figure 1. Experimental setups: (a) LIBS and (b) ICCD.

energy meter (PE25BB-DIF-SH, Nova II, Ophir) at 15 cm after the lens focus. Laser delivered energy to the plasma jet was 20 mJ which was below breakdown threshold in helium at atmospheric pressure under present excitation conditions. The threshold for the laser plasma breakdown was experimentally determined by slowly reducing the applied laser energy, and when the laser plasma disappear that was the energy that we used in LIBS experiment.

The laser synchronization with the high voltage signal and spectrometer was achieved by using three digital delay generators (Stanford Research Systems 645). A signal generator was used as the master device. Signal generator controlled delay

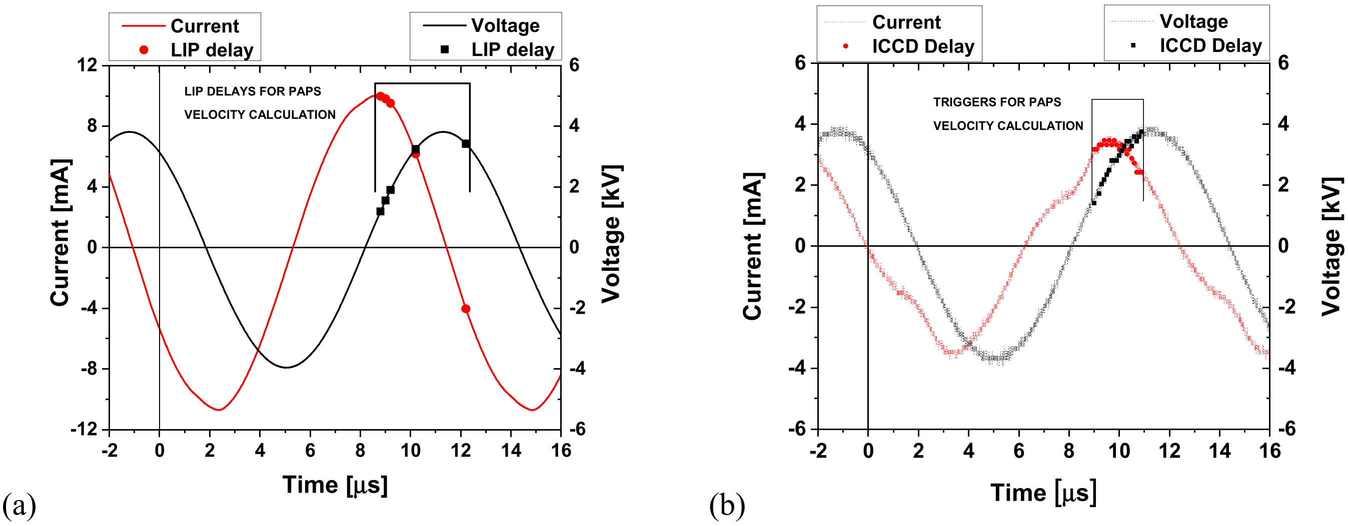

Figure 2. Typical waveforms of the plasma jet discharge (a) Current and voltage signals for the plasma jet measured at the high voltage powering cable. (b) Current and voltage signals for the plasma jet discharge, current was measured as the voltage drop at the 100 kΩ resistor. ICCD camera delay range with the step of 0.1 μs for calculating the ionization front velocity.

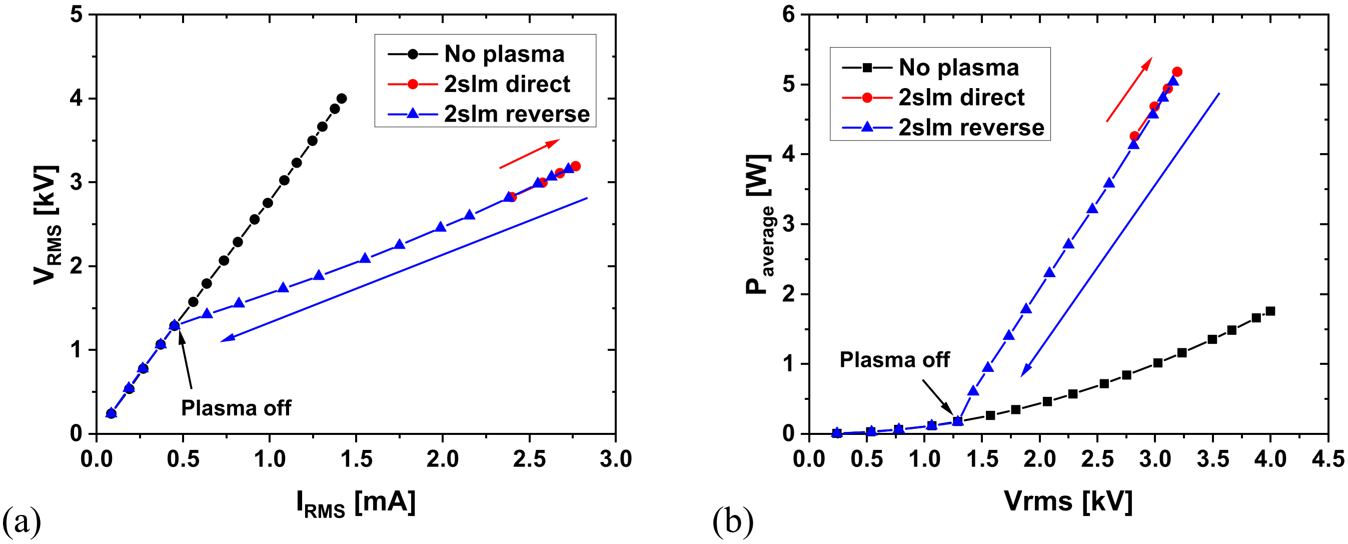

Figure 3. (a) Current voltage characteristics (b) power of the plasma jet as a function of V_{RMS}.

generators 1 and 2 with 80 kHz repetition rate. At the delay generator 2 (see figure 1) sine signal of 80 kHz was reduced to 20 Hz for the laser flash lamps and to 5 Hz for the laser Q-switch. The light from the interaction volume was collected by the lens (Avantes COL-UV/VIS) attached on the optical fiber (solarisation resistant) with a Charge Coupled Device (CCD) spectrometer (AvaSpec-3648, spectral resolution 0.6 nm). The spectrometer was in a triggering mode with integration time of 10 μs. The laser focusing lens and optical fiber were mounted on the y translator. The precision of the translators in y axis direction was 10 μm and in x axis direction 100 μm. The laser spot size was 80 μm. For more details, see [32].

The second experimental setup (figure 1(b)) for the ICCD measurements was previously described in paper [35], with some minor differences. The oscilloscope used here was Agilent DSO 6052a and high voltage probe was Tektronix P6015A, with 75 MHz bandwidth. For the current measurement we used 100× voltage probe (Agilent 10076B) for measurement of the voltage drop at the 100 kΩ resistor. For ICCD time resolved imaging we used Andor iStar DH734I ICCD camera and the plasma jet was in the horizontal position. Optical emission spectrum of the capillary plasma jet was measured using USB spectrometer Ocean Optics Maya2000 Pro (spectral resolution 0.5 nm).

3. Results and discussion

3.1. Electrical properties of the capillary plasma jet

Plasma jet properties are highly dependent on the electrode configuration [36]. With that in mind, we first performed a detailed electrical analysis. The current and voltage signals for

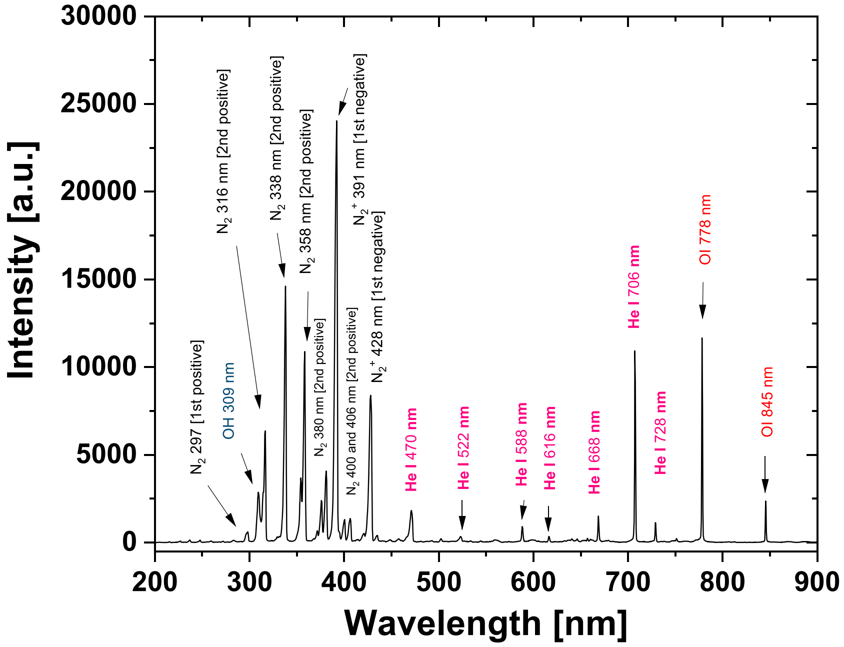

Figure 4. Typical OES spectrum for the helium plasma jet, for 2 slm helium, measured 5 mm below the plasma jet nozzle with 4 W of RF power delivered to the plasma.

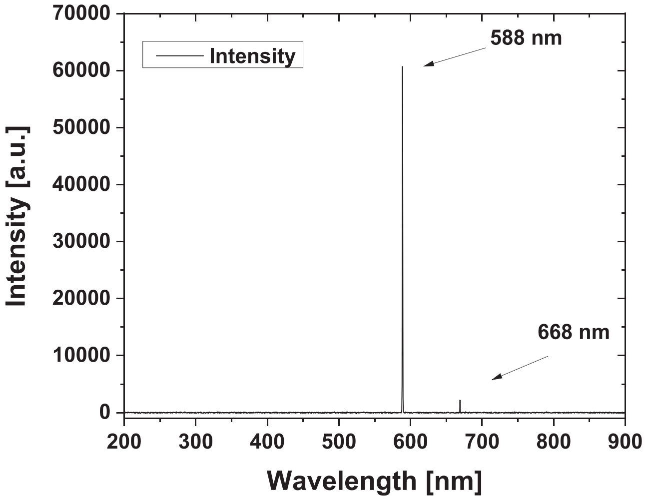

Figure 5. LIP spectrum in helium flow: 588 nm (2p ^{3}P°–3d ^{3}D) and 668 nm (2p ^{1}P°–3d ^{1}D) lines are observed. Helium flow was 2 slm, plasma was induced by the laser 5 mm from the jet nozzle, and 4 W of RF power was delivered to the plasma, the same as in figure 4. Since spectrum in figure 4 was recorded with a different spectrometer (Maya2000Pro) units of the intensity in figures 4 and 5 are completely different.

the plasma jet are shown in figure 2. In figure 2(a) current and voltage waveforms are presented, with the current and voltage waveforms captured at the main high voltage powering cable at the closest point to the powered electrode of the plasma jet. Peak to peak (p–p) values for current (I) were 20 mA and for the voltage (V) were 8.0 kV. The phase difference was close to $\pi/2$ (84°).

In figure 2(b) current and voltage waveforms for the plasma jet are presented. The voltage waveform was recorded near the powered electrode and the current waveform was recorded as the voltage drop on the resistor near the grounded electrode as presented in Maletić *et al* [35]. The measured p–p value of the current was 6.92 mA and of the voltage was 8.0 kV. If we compare the current waveforms at these two different points of the plasma jet (on the High Voltage (HV) power cable and at the resistor), we can see almost three-time (3×) difference in its magnitude. The phase difference between voltage and the current was significantly lower than the current signal measured at the HV cable, it was 55°. The delay positions for the pulsed atmospheric pressure streamers (PAPS [16]) velocity calculation are shown in the figure 2 with circle symbol for the current and square symbol for the voltage. For this capillary plasma jet we can see two peaks superimposed on the current waveform. These peaks can be attributed to the collection of wall charges (Q) on the inner surface of the glass tube in the zone of powered and grounded electrode. In our previous experiments we could not observe the peak in the negative half cycle [35].

The V–I characteristics are given in figure 3(a) as well as the power (in figure 3(b)) as a function of V_{RMS}. The voltage was measured at the HV cable while the current was calculated from measured voltage drop at the 100 kΩ resistor. The calculated impedance for the plasma jet when the 'plasma is off' (without the working gas) was $Z = 2.80$ MΩ, while after plasma formation in the gas flow the impedance decreased to $Z = 0.81$ MΩ. We measured V–I characteristics from the plasma ignition to the maximum power that our power supply can deliver and in the reverse direction until the plasma was extinguished. The power for the plasma jet is presented in figure 3(b). The power range for the capillary jet was narrow in direct direction (increasing power) just 1 W (from 4.2 to 5.2 W), while in reverse direction (decreasing power) the range was around 4.7 W (from 5.2 to 0.5 W).

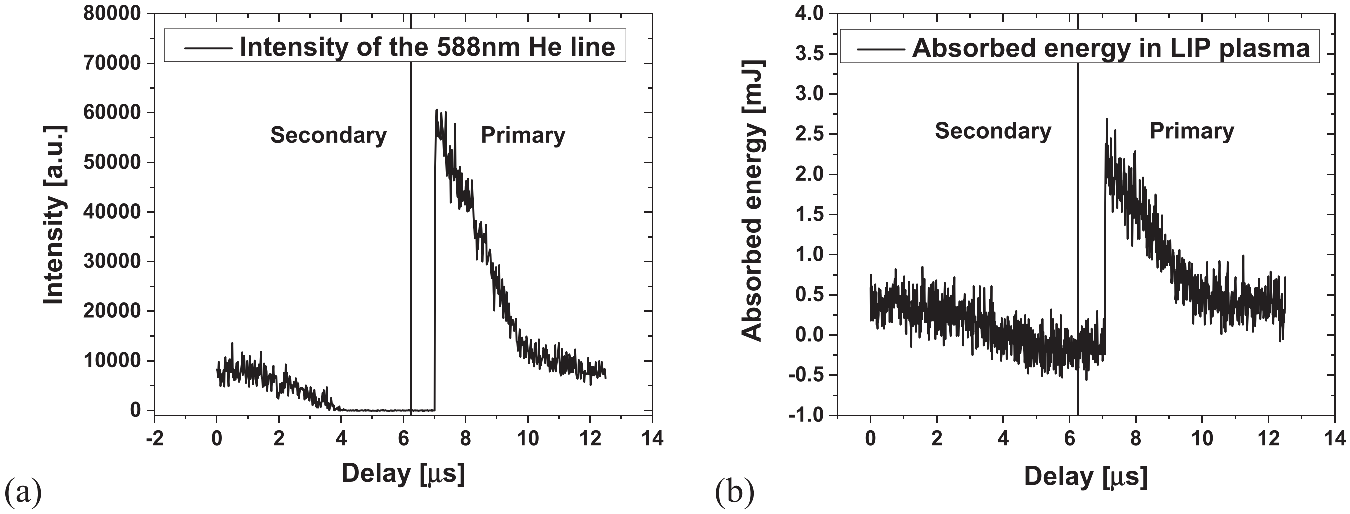

Figure 6. (a) Intensity of helium 588 nm line emission as a function of delay (intensity of emission was integrated over 10 μs and the entire volume of the induced plasma; (b) absorbed laser energy by the plasma jet as a function of the delay of laser trigger. Helium flow was 2 slm, Laser was focused at 5 mm from the jet nozzle, and 4 W of RF power was delivered to the plasma.

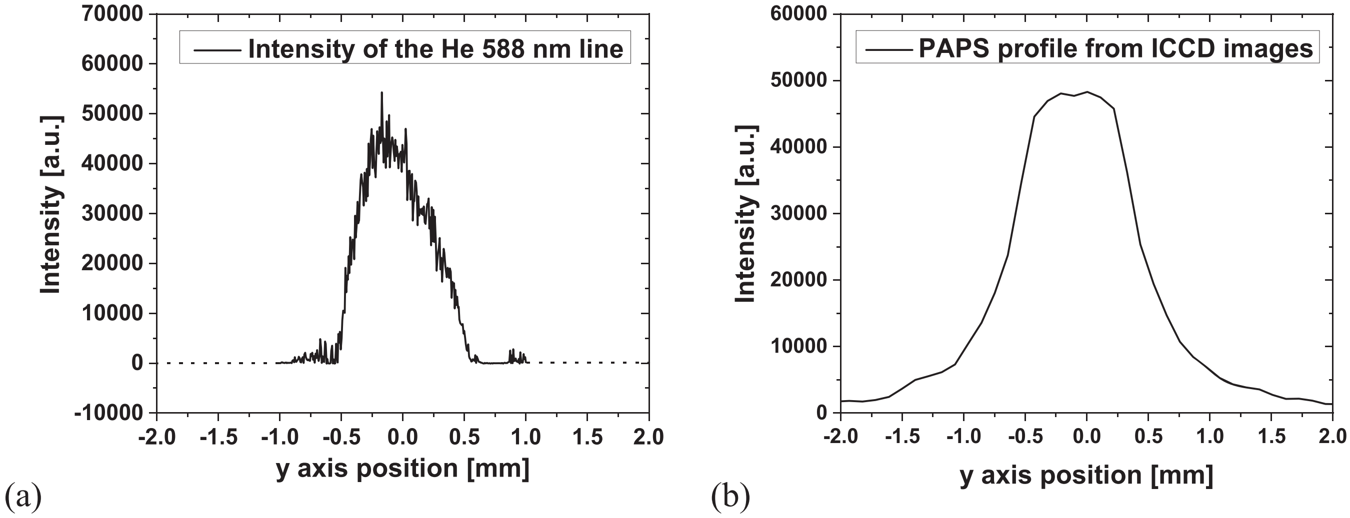

Figure 7. (a) Intensity of the He 588 nm line in the y axis, (b) total emission profile from the ICCD image. Helium flow 2 slm, 5 mm from the jet nozzle, 4 W of RF power delivered to the plasma. [y axis is perpendicular to the axis of the gas flow and it is along the axis defined by the laser beam (radial position in reference Popović *et al* 2019 [32]). Measurements are performed by moving the focal point of the laser along the y axis.].

3.2. Time resolved emission intensity and absorbed laser energy by the plasma jet

In air the laser induced breakdown occurred at about 10 mJ at room temperature (22 °C and with 25% relative humidity). The laser breakdown in air was accompanied with strong visible light from the spark and loud sound from the associated shock wave. When we focused the laser beam in the flow of helium coming from the plasma jet nozzle the breakdown occurred at a much higher laser pulse energy around 30 mJ with much less light emission and weaker sound [32]. When the laser energy was set to 20 mJ, the laser plasma was not induced since there were no seed electrons from the plasma jet present. Light emission from the plasma jet was around 1000 times weaker than the light from the LIP. Typical optical emission spectrum with 400 ms integration time for the helium plasma jet is shown in figure 4. The spectrum was recorded for the 4 W of RF power delivered to the plasma, 2 slm of helium and at the 5 mm in front of the plasma jet nozzle. He I, N_2, N_2^+, OH and OI lines may be observed in the spectrum of the free plasma jet. The He 588 nm line has a very weak intensity that was drastically increased in the LIP.

In figure 5 typical LIP spectrum is presented for the primary discharge (delay 7.08 μs), where one can observe two helium lines, 588 nm (2p ^{3}P°–3d ^{3}D) and 668 nm (2p ^{1}P°–3d ^{1}D). Integration time for the spectrometer was 10 μs. For the further plasma jet diagnostics, we chose the 588 nm line because of its strongest intensity. Molecular lines originating from the plasma jet could hardly be noticed since the LIP was

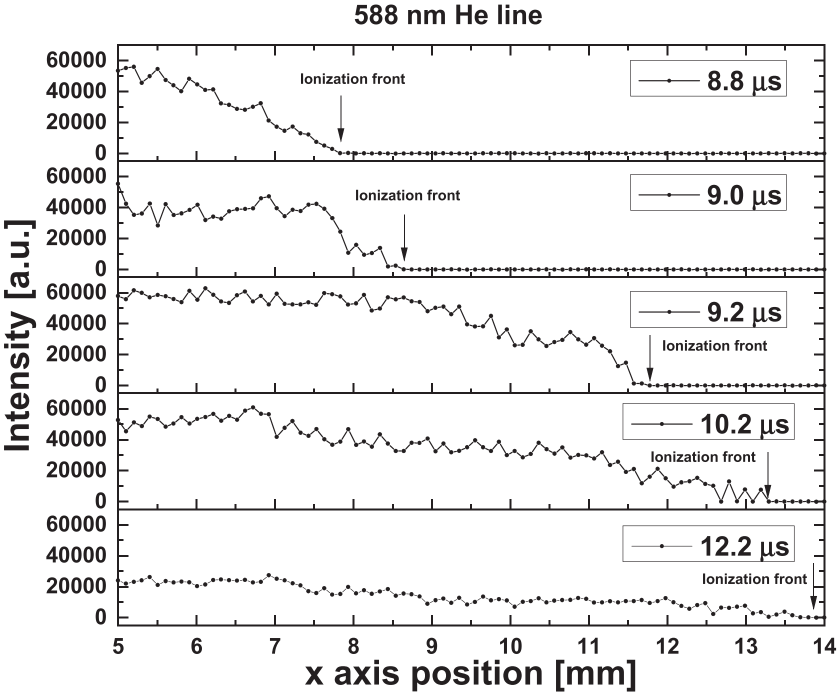

Figure 8. Emission profiles along the *x* axis (distance from the capillary orifice) for different delays, the LIP is formed outside the glass tube. Helium flow was 2 slm, 4 W of power was delivered to the plasma.

producing emission that was several order of magnitude more intense in helium atmosphere.

In figure 6(a) we presented the intensities of the 588 nm He line for different delays of the laser–plasma jet synchronization. The position of the LIP was at 5 mm from the jet nozzle. As one can see the line intensities are dependent on the plasma jet voltages. The 0 μs correspond to 0 mA current, the voltage was around 3.0 kV in the falling slope (see figure 2(b)). This emission corresponds to the current peak in the negative half-cycle (secondary PAPS). When current starts to rise we can observe a sharp emission increase that corresponds to the current peak in the positive half-cycle (primary PAPS). The primary and secondary PAPS are typical for pulsed DC plasma jets [32]. The secondary PAPS was not observed with ICCD measurements (see figure 9) due to insufficient concentrations of seed electrons for the helium excitation in negative half-cycle of the excitation signal. In contrast to this LIP amplifies the emission signal of helium line, so the secondary PAPS were visible in emission spectrum of plasma jet. The difference in intensities between the positive and negative half cycles is around a factor of six (6×). Absorbed laser energy as the function of delay is shown in figure 6(b). We have the same shape of the absorbed light as for the light emission. One could argue that one can observe a smaller peak for the negative and a larger peak for the positive half-cycle. However, it is hard to make such a conclusion due to a different nature of the measurement of absorption and emission. The maximum absorbed laser energy in LIP plasma was 2.5 mJ.

3.3. Comparison of the plasma jet profiles obtained by LIP and ICCD measurement

In figure 7 we show emission profile of the plasma jet at 5 mm from the jet nozzle. As one can see, the profile obtained with the LIP was considerably narrower than the profile from the ICCD images. The broad ICCD profile (figure 7(b)) is due to the light emission from plasma (helium in the center and nitrogen on the outer region of the jet) while the narrower (figure 7(a)) profile is due to the LIP intensity dependence on electron densities in helium flow. One should note that the LIP emission profile is not deconvoluted. Laser focal depth in direction of y-axis was estimated to be about 200 μm. From these two profiles one can estimate the size of the transitional region between the pure helium plasma and the surrounding air. The transitional region has a considerably weaker intensity of He lines than the emission in pure helium plasma. The size of the region with a high concentration of helium was ±0.5 mm (in figure 7(a)) from the jet axis, and the transition region where most chemical reactions are occurring was around 1 mm on both sides beyond the He region. We did not observe any light emission further than ±1.75 mm (in figure 7(b)) from the jet axis.

3.4. Comparison of the velocities for the plasma jet obtained with LIP and ICCD measurements

In this paragraph we calculate the PAPS velocities using the edge of the emission in the axis of plasma jet propagation. The intensities of the 588 nm He line for different delays are shown in figure 8. The procedure for the PAPS velocity cal-

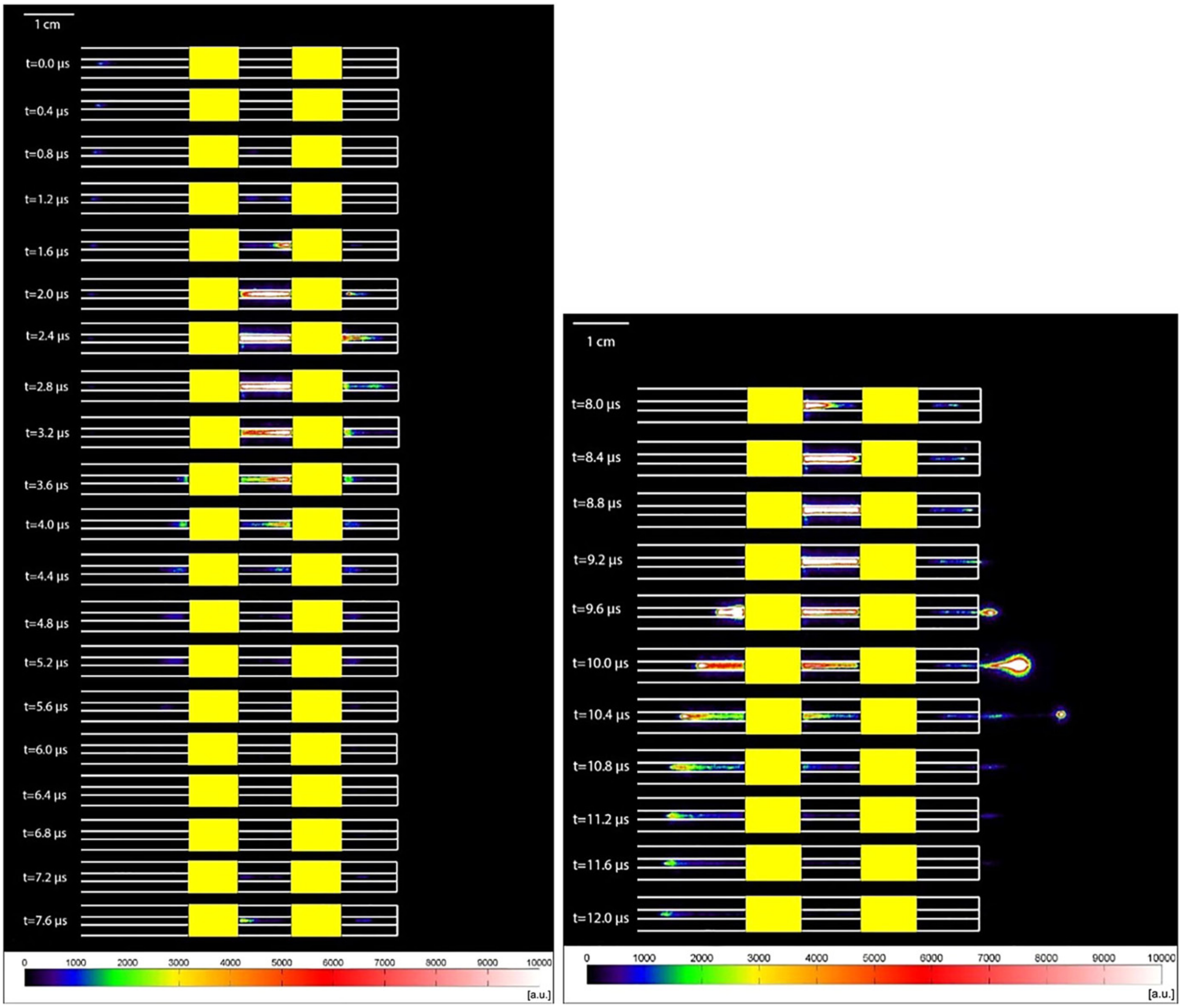

Figure 9. Time resolved broadband ICCD images of the capillary plasma jet for the whole period of the excitation signal, helium flow was 2 slm, 4 W of RF power were delivered to the plasma, gate width was 25 ns, exposure time 2 ms and gain was 200. Recording was made by integration on the chip of the ICCD.

culation is the following: (1) laser beam was focused in the center of the plasma jet; (2) the starting position of the LIP was 5 mm from the jet nozzle (0 on the *x* axis); (3) plasma jet was translated along the *x* axis; (4) for the fixed delay we recorded profiles; (5) for the velocity calculation we used position when the emission intensity drops to zero and that is the edge of the ionization front (marked with arrows in figure 8). As delay was varied we scanned different parts of the propagating front and thus we observed propagation of the emission front along the *x* axis.

In figure 9 we have shown the ICCD images of the capillary plasma jet for the whole period of the excitation time. Left electrode was grounded and the right electrode was powered. We used integration on chip because of the very low light signal from the single period. The exposure time was 2 ms (160 periods), the gate width was 25 ns and the gain was 200. The starting delay position was when the current was zero. As one can see, the formation of the plasma in the negative half cycle occurred at 1.6 μs at the right edge of the powered electrode. Moving further in time the plasma filled the inter-electrode gap with high emission intensity. We have observed low intensity plasma in front of the powered electrode. Positive half-cycle starts at 8.0 μs (voltage waveform) and plasma was first formed at the left edge of the grounded electrode. The PAPS was formed at 9.6 μs, and propagated into the ambient air. At the same time another PAPS was formed at the right edge of the grounded electrode. This 'negative' PAPS was propagating in the opposite direction from the working gas flow. This kind of propagation was not observed in our previous experiments when we used glass tubes with larger I.D. (4 mm) [35].

In figure 10 we show velocities of the ionization fronts of the plasma jet outside the glass tube. The PAPS velocities (squares in figure 10) were calculated from the helium 588 nm

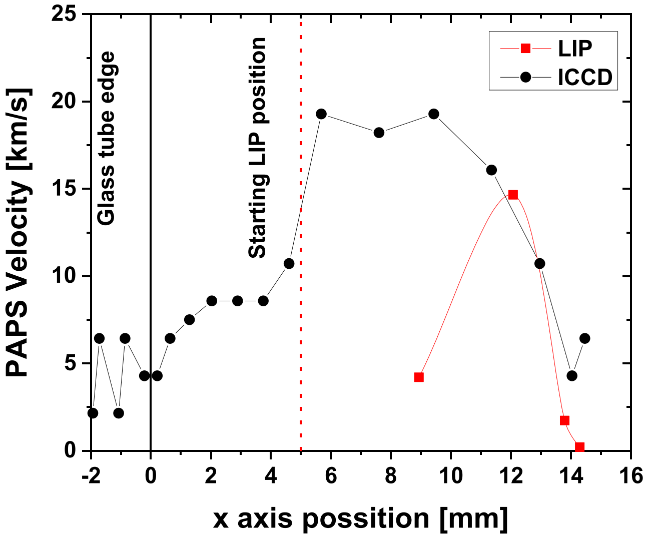

Figure 10. LIP PAPS velocities calculated from He line intensity and PAPS velocities calculated from ICCD images (100 ns step), helium flow was 2 slm, breakdown was induced at 5 mm from the jet nozzle and 4 W of RF power were delivered to the plasma.

line intensity propagation in space (see figure 8), the positions from the jet nozzle were calculated as x position plus 5 mm (starting LIP position). We calculated that the maximal speed of the ionization front to be around 15 km s^{-1}. On the other hand, we show velocities of the IW (circles in figure 10) obtained from the fast ICCD images with the step of 0.1 μs (ICCD images are not presented). The maximal velocity obtained with this method is more precise and it is around the 20 km s^{-1}. One can see that the ionization front starts slowly to accelerate after the moment when PAPS leaves the glass tube up to 4 mm. After that point there is a rapid mixing of helium with the surrounding air and that leads to fast acceleration to the maximal front velocity 10 mm away from the nozzle. After reaching maximal velocity, ionization front velocity slowly decreases until plasma is extinguished at 15 mm from the nozzle. The estimated experimental errors for LIP and ICCD velocities calculation are under 10%.

Having in mind the accuracy of the LIP technique the two sets of results are in agreement. LIP diagnostics provides additional freedom to determine radial profile and observe a finer view of the inner structure of the propagating jet, especially the radial profile of mixing with air.

4. Conclusion

In this research paper we presented electrical properties, LIP and time resolved ICCD images for the capillary helium plasma jet driven by kHz sine waveform.

For this plasma jet we observed a large hysteresis effect when we decreased the power. We also observed the appearance of a peak (2 μs) in the current signal in the negative (falling) half-cycle and with LIP formation detect the presence of charge carrier near the jet nozzle. In the positive (rising) half cycle plasma jet front propagated inside the narrow glass tube against the flow.

We show that the LIBS (running at laser energy below threshold in helium) can be used for time resolved and spatial diagnostic of the APPJ. This method can be used as a complementary method for the diagnostics of plasma jets together with ICCD measurements, or independently. Using the LIP, we detected the secondary PAPS in negative half cycle of the excitation signal, we determined the dimensions of plasma channel with sufficient charge carriers necessary for initiation of the laser induced breakdown. Thus one may provide a profile of helium plasma mixing with air. Reasonable agreement of the two sets of results gives us confidence to claim that one may be able to use LIP to establish anatomy of more complex plasma systems. The LIP technique can be used together with LIF (or intra cavity spectroscopy) required to detect atoms and radicals produced in the plasma.

Acknowledgments

This research has been supported by the Ministry of Education, Science and Technological Development, Republic of Serbia, under Grant No. 451-03-68/2020-14/200024 and Center of Excellence Non Equilibrium Processes, IPB. DM is also grateful for the funding of STSM in COST action TD1208 and to the Croatian Science Foundation HrZZ—IP-2019-04-6418. One of the authors (ZLP) is grateful to SASA project F155 and to Ulster University, U.K. SM and DP are grateful to the Croatian Science Foundation, through project IP-2013-11-2753.

Data availability statement

The data that support the findings of this study are available upon reasonable request from the authors.

ORCID iDs

Dejan Maletić https://orcid.org/0000-0002-0368-6568
Dean Popović https://orcid.org/0000-0003-3906-3482
Nevena Puač https://orcid.org/0000-0003-1142-8494
Zoran Lj Petrović https://orcid.org/0000-0001-6569-9447
Slobodan Milošević https://orcid.org/0000-0002-4455-7869

References

[1] Petrović Z L, Puač N, Lazović S, Maletić D, Spasić K and Malović G 2012 *J. Phys.: Conf. Ser.* **356** 012001
[2] Bradley J W, Oh J-S, Olabanji O T, Hale C, Mariani R and Kontis K 2011 *IEEE Trans. Plasma Sci.* **39** 2312–3
[3] Maletić D, Puač N, Lazović S, Malović G, Gans T, Schulz-von der Gathen V and Petrović Z L 2012 *Plasma Phys. Control. Fusion* **54** 124046
[4] Oh J-S, Walsh J L and Bradley J W 2012 *Plasma Sources Sci. Technol.* **21** 034020
[5] Oh J-S, Furuta H, Hatta A and Bradley J W 2015 *Japan. J. Appl. Phys.* **54** 01AA03
[6] Zaplotnik R, Biščan M, Krstulović N, Popović D and Milošević S 2015 *Plasma Sources Sci. Technol.* **24** 054004

[7] Boeuf J-P, Yang L L and Pitchford L C 2013 *J. Phys. D: Appl. Phys.* **46** 015201

[8] Li J, Lei B, Wang J, Zhang T, Tang J, Wang Y, Zhao W and Duan Y 2019 *IEEE Trans. Plasma Sci.* **47** 3134–40

[9] Emmert S *et al* 2013 *Clin. Plasma Med.* **1** 24–9

[10] Wu S, Wang Z, Huang Q, Tan X, Lu X and Ostrikov K 2013 *Phys. Plasmas* **20** 023503

[11] Ghimire B *et al* 2019 *Appl. Phys. Lett.* **114** 093701

[12] Oh J S, Szili E J, Hatta M, Ito M and Shirafuji T 2019 *Plasma* **2** 127–37

[13] Cheng X, Sherman J, Murphy W, Ratovitski E, Canady J and Keidar M 2014 *PLoS One* **9** 1–9

[14] Fröhling A, Baier M, Ehlbeck J, Knorr D and Schlter O 2012 *Innov. Food Sci. Emerg. Technol.* **13** 142–50

[15] Nastuta A V, Topala I, Grigoras C, Pohoata V and Popa G 2011 *J. Phys. D: Appl. Phys.* **44** 105204

[16] Ghasemi M, Olszewski P, Bradley J W and Walsh J L 2013 *J. Phys. D: Appl. Phys.* **46** 052001

[17] Kim J Y and Kim S-O 2011 *IEEE Trans. Plasma Sci.* **39** 2278–9

[18] Wang R, Xu H, Zhao Y, Zhu W, Zhang C and Shao T 2019 *Plasma Chem. Plasma Process.* **39** 187–203

[19] Lamichhane P, Paneru R, Nguyen L N, Lim J S, Bhartiya P, Adhikari B C, Mumtaz S and Choi E H 2020 *React. Chem. Eng.* **5** 2053–7

[20] Royintarat T, Seesuriyachan P, Boonyawan D, Choi E H and Wattanutchariya W 2019 *Curr. Appl. Phys.* **19** 1006–14

[21] Gierczik K, Vukušić T, Kovcs L, Szkely A, Szalai G, Milošević S, Kocsy G, Kutasi K and Galiba G 2020 *Plasma Process. Polym* **17** 1900123

[22] Kutasi K, Popović D, Krstulović N and Milošević S 2019 *Plasma Sources Sci. Technol.* **28** 095010

[23] Tanaka H, Mizuno M, Ishikawa K, Nakamura K, Kajiyama H, Kano H, Kikkawa F and Hori M 2011 *Plasma Med.* **1** 265–77

[24] Tomić S, Petrović A, Puač N, Škoro N, Bekić M, Petrović Z L and Čolić M 2021 *Cancers* **13** 1626

[25] Adamovich I *et al* 2017 *J. Phys. D: Appl. Phys.* **50** 323001

[26] Puač N, Gherardi M and Shiratani M 2018 *Plasma Process. Polym.* **15** 1700174

[27] Hahn D W and Omenetto N 2012 *Appl. Spectrosc.* **66** 347–419

[28] Burger M, Skočić M and Bukvić S 2014 *Spectrochim. Acta* B **101** 51–6

[29] Barreda F-A, Trichard F, Barbier S, Gilon N and Saint-Jalmes L 2012 *Anal. Bioanal. Chem.* **403** 2601–10

[30] Ji H, Ding Y, Zhang L, Hu Y and Zhong X 2021 *Appl. Spectrosc. Rev.* **56** 193–220

[31] Morgan C G 1975 *Rep. Prog. Phys.* **38** 621–65

[32] Popović D, Bišćan M and Milošević S 2019 *Plasma Sources Sci. Technol.* **28** 055009

[33] Woodbury D, Schwartz R M and Milchberg H M 2019 *Optica* **6** 811

[34] Gott R P and Xu K G 2020 *J. Phys. D: Appl. Phys.* **53** 315201

[35] Maletić D, Puač N, Selaković N, Lazović S, Malović G, Dorđević A and Petrović Z L 2015 *Plasma Sources Sci. Technol.* **24** 025006

[36] Maletić D, Puač N, Malović G, Dorđević A and Petrović Z L 2017 *J. Phys. D: Appl. Phys.* **50** 145202

[37] Karakas E, Akman M A and Laroussi M 2012 *Plasma Sources Sci. Technol.* **21** 034016

nanomaterials

Article

Enhancement of Methylene Blue Photodegradation Rate Using Laser Synthesized Ag-Doped ZnO Nanoparticles

Damjan Blažeka [1], Rafaela Radičić [1], Dejan Maletić [1], Sanja Živković [2], Miloš Momčilović [2] and Nikša Krstulović [1,*]

[1] Institute of Physics, Bijenička Cesta 46, 10000 Zagreb, Croatia
[2] VINČA Institute of Nuclear Sciences—National Institute of the Republic of Serbia, University of Belgrade, P.O. Box 522, 11351 Belgrade, Serbia
* Correspondence: niksak@ifs.hr

Abstract: In this work, Ag-doped ZnO nanoparticles are obtained via pulsed laser ablation of the Ag-coated ZnO target in water. The ratio of Ag dopant in ZnO nanoparticles strongly depends on the thickness of the Ag layer at the ZnO target. Synthesized nanoparticles were characterized by XRD, XPS, SEM, EDS, ICP-OES, and UV–VIS spectrophotometry to obtain their crystal structure, elemental composition, morphology and size distribution, mass concentration, and optical properties, respectively. The photocatalytic studies showed photodegradation of methylene blue (MB) under UV irradiation. Different ratios of Ag dopant in ZnO nanoparticles influence the photodegradation rate. The ZnO nanoparticles doped with 0.32% silver show the most efficient photodegradation rate, with the chemical reaction constant of 0.0233 min^{-1}. It exhibits an almost twice as large photodegradation rate compared to pure ZnO nanoparticles, showing the doping effect on the photocatalytic activity.

Keywords: photocatalysis; ZnO nanoparticles; Ag-doped ZnO; zinc oxide; bicomponent nanoparticles; photodegradation; silver dopant; methylene blue; laser ablation in water; pulsed laser deposition

Citation: Blažeka, D.; Radičić, R.; Maletić, D.; Živković, S.; Momčilović, M.; Krstulović, N. Enhancement of Methylene Blue Photodegradation Rate Using Laser Synthesized Ag-Doped ZnO Nanoparticles. *Nanomaterials* **2022**, *12*, 2677. https://doi.org/10.3390/nano12152677

Academic Editor: Vincenzo Vaiano

Received: 13 June 2022
Accepted: 1 August 2022
Published: 4 August 2022

1. Introduction

Zinc oxide (ZnO) is a wide-bandgap semiconductor material with unique electrical, mechanical and optical properties, making it appropriate for a wide range of applications. Some of these properties are high optical transparency, high electron mobility (200–300 cm^2 V^{-1} s^{-1}), large direct bandgap (3.37 eV at room temperature), large exciton binding energy (60 meV), and high mechanical stability. ZnO is a low-cost, low-toxic, and easily available material, with many possible economical methods of synthesis that makes it appropriate for a broad range of scientific research and industrial applications [1]. ZnO is widely used in industry for the production of solar cells, light-emitting diodes and transistors, sensors, UV-protecting coatings, baby powders, vulcanization products, and for improving concrete and ceramic quality [2–5]. Photocatalytic, antibacterial, food-packaging, and medical (cancer-treatment) applications of ZnO are considered fast-developing technology [6–8]. The interest of this work is based on the photocatalytic properties of ZnO, especially those related to the photodegradation of surrounding chemicals in water, the process that can be used in water purification [9]. On the other hand, the widespread production and use of ZnO can lead to high concentrations of ZnO waste material in the aquatic environment that cause some degree of ecotoxicity, due to the large photocatalytic and antibacterial activity of ZnO [10]. In the photocatalytic process, electrons and holes, excited after light irradiation of semiconductor materials, interact with the surrounding medium, causing and accelerating many chemical and redox reactions. ZnO is the second most popular photocatalytic material after titanium oxide (TiO_2), and in both materials, the processes that lead to photodegradation of the surrounding chemicals are similar [11]. Electrons in the conduction band transfer to O_2, producing very reactive O^{2-} ions, while holes from the valence band transfer to hydroxide ion OH^-, producing hydroxyl radical ·OH, which is very reactive [12]. The photocatalytic degradation of pollutants in water occurs due to interaction with reactive radicals. Light irradiation may also excite electrons in pollutants, leading to their transfer to the catalyst conductive band and the formation of additional reactive radicals [13]. The use of nanomaterials as photocatalysts is very efficient, due to the large area/volume ratio and better light irradiation harvesting. In nanoparticles, the same amount of material has a larger active site area and is irradiated with larger light intensity when compared to the bulk material. Both effects strongly increase the number of electrons and holes available for reactions at the catalyst surface.

The wide bandgap of ZnO is the reason why UV light is needed for electron/hole excitation and this is a great limitation in photocatalytic applications because sunlight contains only 5% intensity of UV light in the whole EM spectrum [14]. However, the physical and chemical properties are easily adapted and modified by doping with various materials and surface engineering [12]. Many materials are used as dopants in ZnO to improve its photocatalytic activity and expand it to the visible part of the spectrum. Silver (Ag) seems to be the most promising doping material for this purpose [3]. Ag acts as a p-dopant in the ZnO crystal lattice, which in its pure form has a hexagonal wurtzite crystal structure that often has n-type conductivity, due to the presence of oxygen vacancies [13,15]. Doping with Ag is also used to improve the antibacterial activity of ZnO [16,17]. Furthermore, Ag, as a noble metal, can impose the photostability of ZnO, which is very important because of the fast photocorrosion, one of the main disadvantages of pure ZnO [12]. Doping can increase photocatalytic activity by creating band levels that act as traps for charge carriers. Therefore, the recombination rate of electrons and holes decreases, and their lifetime increases [14]. Several methods are usually applied for the synthesis of Ag-doped ZnO nanoparticles (ZnO NP). Some of them are photodeposition via photoreduction of Ag^{2+} [18,19], precipitation [20,21], the solvothermal route [14,22], using Ag nitrate in the sol-gel method [23], the hydrothermal route [24], laser induction [25], ultrasonic spray pyrolysis [26] and flame spray pyrolysis [27]. Pulsed laser ablation in liquid (PLAL) is a green method for the synthesis of colloidal solutions, which contains very pure nanoparticles without the unwanted residual byproducts [28]. Nanoparticles' purity and the possibility of using a large variety of materials as a target in ablation are the main advantages of PLAL compared to chemical routes of NP synthesis.

From the literature, it is evident that laser ablation in liquids has been applied for doping ZnO. In [29], Ag-doped ZnO nanoparticles were successfully synthesized by nanosecond laser ablation of Zn for 30 min and then Ag for 1, 3 or 5 min. Furthermore, some works were found where targets for laser ablation were prepared. The targets are produced through sintering at high temperatures and compressing, which can last up to two days and has many steps in the production process [30–32].

In our work, we propose a new method, which is thoroughly described in the experimental section, for the production of Ag-doped ZnO NPs. An Ag thin layer is deposited at the ZnO target surface with the pulsed laser deposition (PLD) technique, and the obtained target is ablated by a pulsed laser in water. As a result, a colloidal solution of Ag-doped ZnO nanoparticles is formed. Furthermore, a ratio of Ag dopant in the ZnO NP is varied by using different thicknesses of Ag layer at the ZnO target irradiated in PLAL. ZnO NPs, with different ratios of Ag dopant, are then tested as a catalyst in photocatalytic degradation of methylene blue. The method is simple, fast and versatile, allowing a combination of a wide variety of dopants and semiconductors. Moreover, the overall process (including PLD and PLAL) for the synthesis of Ag-doped ZnO NP colloidal solution takes approximately 10 min.

2. Materials and Methods

2.1. Preparation of the Ag Thin Films at the ZnO Substrates by PLD

The thin films of Ag were deposited at the ZnO substrates (purity > 99.99%, GoodFellow, Huntingdon, UK) by PLD in a vacuum. The 1 mm silver plate (purity > 99.99%, GoodFellow) was used as the laser target in PLD. The ZnO substrate and the Ag target were placed at the two stages separated 1 cm inside the vacuum chamber, which both rotated to ensure the homogenous laser irradiation of the Ag target and homogeneity of the deposited Ag film. An Nd:YAG laser (300 mJ, 5 Hz, 5 ns pulse duration, wavelength 1064 nm, Quantel, Brilliant, Les Ulis, France) was used for Ag target irradiation in the PLD process. Laser pulses were focused onto the target surface using a 30 cm lens yielding laser fluence of 12 J/cm^2. In order to make samples with different thicknesses of the silver film at the ZnO substrate, the following six different numbers of pulses were used in PLD: 50, 200, 500, 1000, 2000, and 3000. The detailed schematics procedure of the two-step synthesis of Ag-doped ZnO nanoparticles is shown in Figure 1 [33]. As a first step, in Figure 1a, pulsed laser deposition of Ag onto ZnO substrate is shown. As a result of the deposition, a two-layer structure was obtained, consisting of several nanometers thick Ag thin film deposited over the ZnO substrate, as shown in Figure 1b.

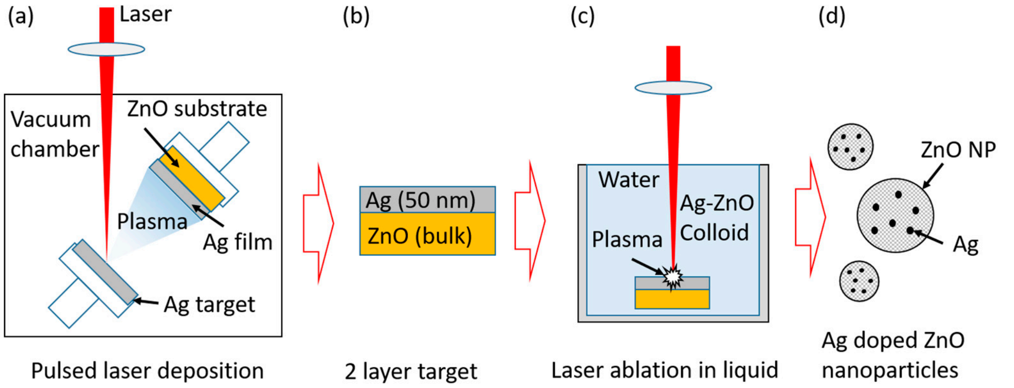

Figure 1. Experimental scheme for the synthesis of Ag-doped ZnO nanoparticles. (**a**) Pulsed laser deposition of Ag onto ZnO substrate (bulk), (**b**) two-layer target formed in PLD comprised of thin Ag film and ZnO bulk, (**c**) laser ablation of two-layer target in water and (**d**) Ag-doped ZnO nanoparticles synthesized in (**c**).

2.2. Syntheses of the Ag-Doped ZnO NP Using PLAL

In the second step, an Ag-coated target was used for the pulsed laser ablation in the water process, producing an Ag-doped ZnO colloidal solution as a final product (Figure 1d). The colloidal solutions of nanoparticles were prepared for six targets, synthesized by PLD in (Figure 1a) to obtain the ZnO NPs with different Ag dopant ratios. The pure ZnO target was ablated to synthesize the colloidal solution of pure ZnO NP as a reference solution. The target, as shown in Figure 1b, was immersed in the 25 mL of MilliQ water and placed about 2.5 cm under the water surface. The surface of approximately 1 cm^2 in size was continually scanned by the pulsed laser beam to achieve homogenous ablation of the sample. The total number of pulses for irradiation of each sample was 2000, using the same laser as for PLD. The laser beam was focused by a 10 cm lens to enhance ablation. The energy delivered to the sample was about 120 mJ per pulse, and the calculated fluence was 79 J/cm^2. The experimental setup is shown in Figure S1 in the Supplementary Material.

2.3. Characterization of the Ag-Doped ZnO NP

2.3.1. UV–Vis

Photoabsorbance of every colloidal solution of Ag-doped or pure ZnO NP was measured in order to analyze the influence of Ag doping on ZnO NP optical properties. Photoabsorbance data were used to determine the ZnO NP bandgap from the Tauc plot. Photoabsorbance was measured immediately after the synthesis of every colloidal solution of nanoparticles, using a UV–Vis spectrophotometer (Lambda 25, Perkin Elmer, Waltham, MA, USA).

2.3.2. Structural Analysis (XPS, XRD, SEM, TEM)

In order to perform structural characterization of ZnO NPs, the produced colloid was dropped onto a silicon substrate and left to air dry to obtain the ZnO NP film.

The X-ray photoelectron spectroscopy (XPS) analysis was carried out with the PHI-TFA XPS spectrometer produced by Physical Electronics Inc. The analyzed area was 0.4 mm in diameter and the analyzed depth was about 3–5 nm. The sample surface was excited by X-ray radiation from a monochromatic Al source at photon energy of 1486.6 eV. The high-energy resolution spectrum was acquired with an energy analyzer, operating at a resolution of about 0.6 eV and pass energy of 29 eV. During data processing, the spectrum was aligned by setting the C 1s peak at 284.8 eV, characteristic for the C-C/C-H bonds. The accuracy of binding energies was about ± 0.3 eV. Quantification of surface composition was performed from XPS peak intensities, considering the relative sensitivity factors provided by the instrument manufacturer [34]. Two different XPS measurements were performed on each sample, and the average composition was calculated.

The crystallinity and crystalline phases were studied by grazing incidence X-ray diffraction (GIXRD). The crystalline structure of ZnO NP was investigated using a D5000 diffractometer (Siemens, Karlsruhe, Germany) in parallel beam geometry with Cu Kα radiation, a point detector, and a collimator in front of the detector. Grazing incidence X-ray diffraction (GIXRD) scans were acquired with the constant incidence angle α_i of 1°, ensuring that the information contained in the collected signal covered the entire film thickness. The following JCPDS cards were used for crystallographic analysis: JCPDS 36-1451 (ZnO), JCPDS 04-0783 (Ag), JCPDS 43-1038 (AgO), and JCPDS 76-1393 (Ag_2O).

The morphology and size-distribution of the obtained nanoparticles were studied by a field emission scanning electron microscope (SEM, Joel 7600F, Tokyo, Japan). Samples for SEM imaging were prepared by dropping a colloidal solution on a 5×5 mm^2 Si wafer. The colloidal solutions were sonicated for 5 min before the deposition.

The detailed morphology of the nanoparticles was obtained by a transmission electron microscope (TEM, JEOL JEM-1400 Flash, Tokyo, Japan). Samples for imaging were prepared by dropping one drop of colloidal solution onto the TEM grid. The colloidal solutions were sonicated for 5 min before the deposition.

2.3.3. ICP-OES

Quantitative elemental analysis of the nanoparticles, prepared in the form of aqueous solutions, was performed using a Thermo Scientific iCAP 7400 duo analyzer, an instrument used for inductively coupled plasma optical emission spectrometry (ICP-OES). ICP-OES measurements were taken to calculate the mass concentration of the ablated material and to estimate the Ag weight ratio in the colloidal particles. Before analysis, 2mL of each NP solution was treated with the same volume of analytical grade 65% (w/v) HNO_3 or aqua regia (Au, Pt), and diluted to 10 mL with distilled high-purity deionized water in a volumetric flask. The calibration standard solutions of Zn, Au, Pt, and Ag were prepared from a single element commercial standard (J.T. Baker 1000 µg/mL and Accu Trace (1000 µg/mL)) by diluting it to different volumes of distilled high-purity deionized water with 1% (w/v) analytical grade HNO_3. The data acquisition and processing stages were performed by using the Thermo Scientific Qtegra Intelligent Scientific Data Solution (ISDS, Waltham, MA USA) software. The obtained results are presented in the form of the average values of the three measurements.

2.4. Photocatalytic Measurements

An Hg lamp (Jelight Co., Zagreb, Croatia) was used for irradiation of the solutions that contained the pure and Ag-doped ZnO NPs and the organic dye methylene blue was used to achieve MB photocatalytic degradation. The irradiation intensities of the lamp were measured using a radiometer (Opsytec Radiometer RMD, Ettlingen, Germany) and the intensities were as follows: VIS 2.11 klx, UVA 0.2 mW/cm^2, UVB 0.02 mW/cm^2 and UVC 0.08 mW/cm^2. The optical emission spectrum of the lamp is shown in Figure S2 in the

Supplementary Material. For purposes of MB photodegradation rate calculation, solution absorbance was measured every 10 min of irradiation using a UV–Vis spectrophotometer. Initial MB concentration for all the samples corresponds to the absorbance maxima $A_0 = 2$ of the pure MB solutions in water and was calculated to be 2.7×10^{-5} mol/L from the Beer–Lambert law, using the extinction coefficient 75,000 cm^{-1}/M and $A_0 = 2$ at peak maximum at $\lambda = 664$ nm.

3. Results and Discussion

3.1. SEM and TEM Images

The SEM scans of all the samples show that ablation of the ZnO target resulted in the formation of colloidal particles, which were distributed in a large variety of sizes and shapes. It is worth mentioning that morphology and size-distribution of the nanoparticles is independent from the amount of silver that differs by a few nanometers (including pure ZnO NP). In Figure 2, examples of the SEM micrographs are shown for the pure and Ag-doped ZnO NP. In Figure 2a,c, it can be observed that the spherical nanoparticles prevail, and some small amounts of microparticles in the form of large debris structures with irregular shapes are present. The size-distributions of pure and Ag-doped ZnO NP are shown in Figure 2b,d, respectively. Size-distributions can be fitted with LogNormal functions that achieve a maximum value at a diameter of 53 nm for pure and 47 for Ag-doped ZnO NPs.

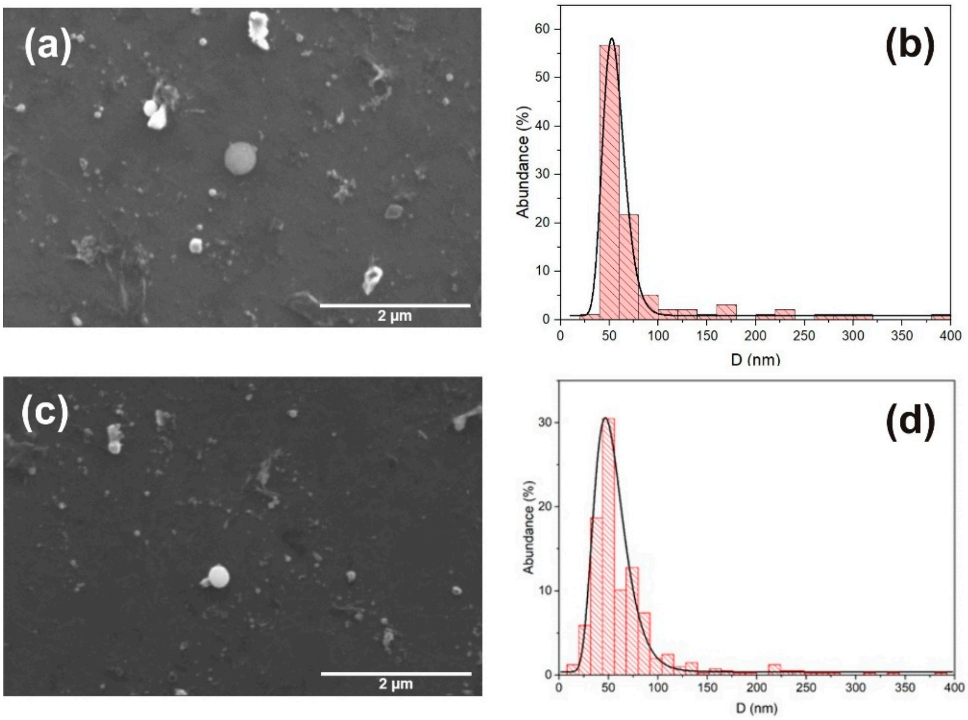

Figure 2. SEM micrograph of (**a**) pure ZnO NP with (**b**) corresponding size-distribution with maximum at 53 nm. SEM micrograph of (**c**) Ag-doped ZnO NP with (**d**) corresponding size-distribution with maximum at 47 nm.

In Figure 3, TEM images for pure (a, b) and Ag-doped (c, d) ZnO NP are presented. Figure 3a,c show the presence of spherical nanoparticles with different sizes and irregular material formed during the LAL process. Figure 3b,d show the surface morphology of the nanoparticles. It can be observed that in both cases, the NP surface is relatively smooth. Nevertheless, the edges are not perfectly sharp, indicating that the NP surface has some roughness. The differences in photocatalytic activities between the pure and Ag-doped ZnO NPs are obviously not dependent on surface morphology.

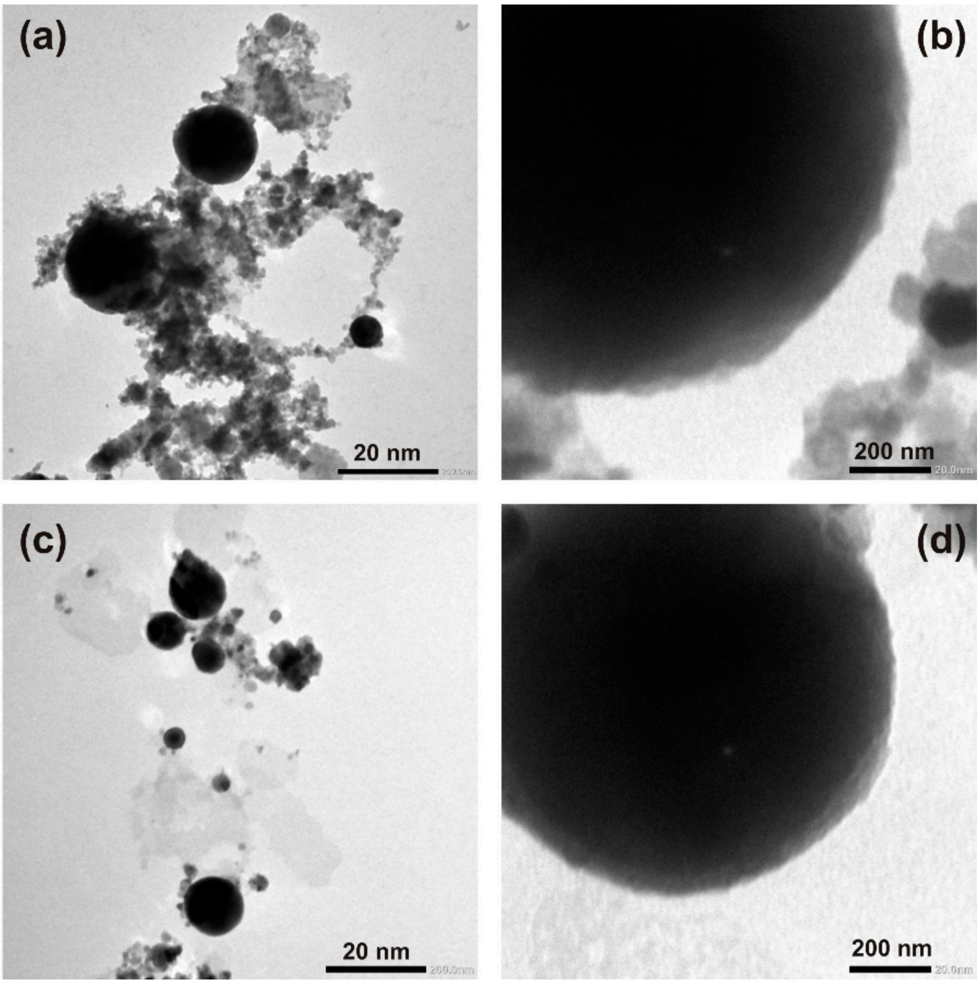

Figure 3. TEM images of pure ZnO NP (**a**,**b**) and Ag-doped ZnO NP (**c**,**d**).

3.2. XRD Patterns

The XRD spectrum of colloidal Ag-doped ZnO nanoparticles (3000p used for Ag deposition in PLD) and reference XRD spectral peaks for ZnO, Ag, AgO, and Ag_2O are shown in Figure 4. The majority of the detectable Bragg peaks (31.75°-(100), 34.45°-(002), 36.2°-(101), 47.6°-(102), 56.55°-(110), 62.85°-(103), 68°-(112) and 69.1°-(201)) correspond to ZnO. The majority of the ablated material crystallized in the hexagonal wurtzite ZnO phase. The presence of all main ZnO diffraction peaks indicates that ZnO crystallites are randomly oriented. The low-intensity peak at 32.75° can probably be attributed to the corresponding peak in the AgO reference spectrum. The absence of Ag peaks indicates that Ag in the colloidal solution is not in the form of pure Ag nanoparticles or Ag crystalline clusters in ZnO nanoparticles, indicating that Ag atoms are incorporated in the ZnO crystal lattice. Since the sample selected for XRD analysis is synthesized by using the largest number of laser pulses in PLD (3000p), it is expected that in all other samples, the ZnO wurtzite crystal structure and some amount of Ag also prevail, which is well-incorporated in the ZnO crystal lattice.

However, to study the effect of Ag doping on the ZnO lattice diffraction peaks for (100), (002), and (101) planes were compared for the doped and pure ZnO nanoparticles, as is shown in Figure 5.

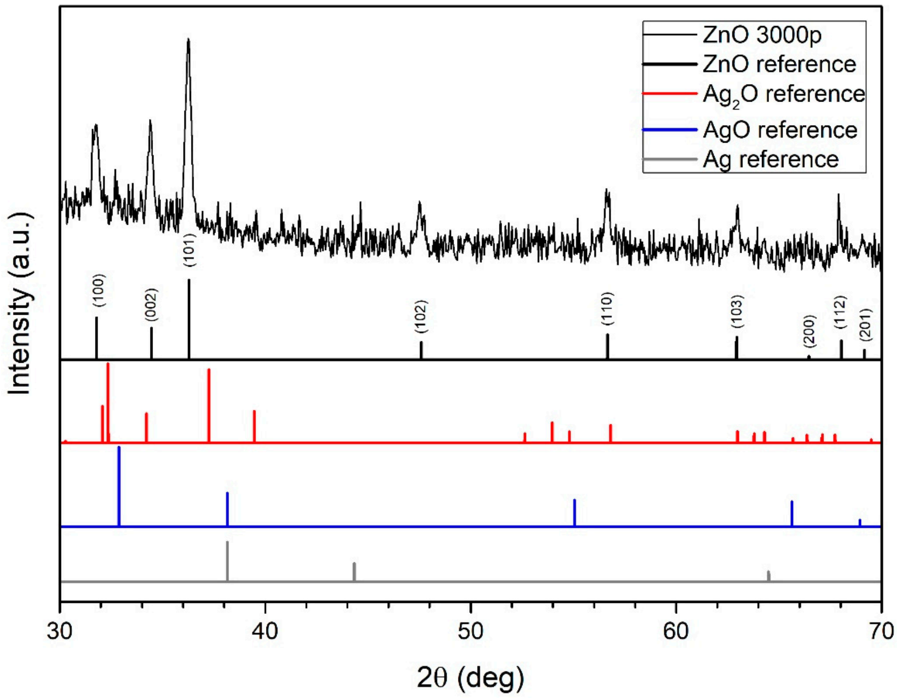

Figure 4. XRD spectrum of ZnO NP (3000 pulses used for Ag deposition in PLD) and reference XRD spectral peaks of ZnO, Ag, AgO and Ag_2O.

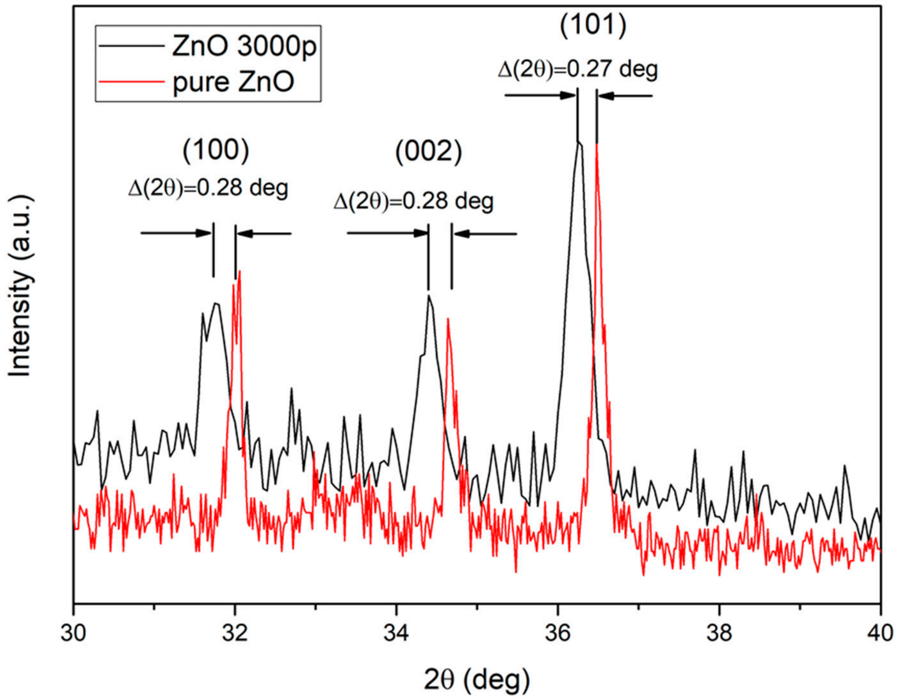

Figure 5. The shift of Ag-doped ZnO XRD peaks, with respect to the pure ZnO peaks.

The XRD peaks of the Ag-doped ZnO NPs shifted to a lower 2θ angle value, as compared with those of pure ZnO nanoparticles. This shift appears due to the fact that the radius of the incorporated Ag^+ ions is greater than that of Zn^{2+}, which consequently causes lattice expansion [35]. The FWHM of the pure ZnO diffraction peaks is narrower than the Ag-doped ZnO peaks, implying that the doping causes the formation of smaller crystallites [36]. The average crystallite size (D) was calculated using Debye–Scherrer's formula [37], using data from the pure and Ag-doped ZnO main XRD peaks.

$$D = \frac{0.9 \cdot \lambda}{\beta \cdot \cos\theta} \quad (1)$$

where λ is the wavelength of the X-ray beam (1.5406 Å), β is the full width at half maximum (in radians), and θ is the diffraction or Bragg's angle. The calculated average crystallite sizes are 49 ± 6 nm for the pure ZnO and 23 ± 1 nm for the Ag-doped ZnO. Furthermore, one must note that the relative intensities of all the diffraction peaks do not change significantly for the Ag-doped and pure ZnO structures. It means that in both cases, there is no preferential growth rate in any direction and that the presence of Ag atoms/ions does not change the growth mechanism of the ZnO nanoparticles in LAL, as described in [38]. The Ag doping causes lattice structural changes, which are also evident if one compares a and c lattice constants for doped and pure samples of the wurtzite ZnO structure. The lattice constants are calculated using Bragg's law of diffraction, which is as follows:

$$n \cdot \lambda = 2 \cdot d \cdot \sin(\theta) \quad (2)$$

where $n = 1$ (order of diffraction), λ is the X-ray wavelength (λ = 1.5406 Å), d is the spacing between the planes defined by Miller indices (h,k,l), and θ is the position of the diffraction peak. The relation of plane spacing in a hexagonal structure and Miller indices are defined in [39], while ((100) orientation) and c ((002) orientation) spacing can be calculated using the following formulae:

$$a = \frac{\lambda}{\sqrt{3} \cdot \sin\theta} \quad (3)$$

$$c = \frac{\lambda}{\sin\theta} \quad (4)$$

The lattice constants for Ag-doped and pure ZnO nanoparticles are listed in Table 1.

Table 1. Lattice constants a and c for pure and Ag-doped ZnO NPs.

Lattice Constant (Orientation)	Pure ZnO	Ag-Doped ZnO
a (100)/Å	3.23	3.25
c (002)/Å	5.17	5.21

From Table 1, it is evident that the lattice constants a and c are larger for Ag-doped than that of pure ZnO nanoparticles, implying lattice expansion. An increase in lattice parameters can be ascribed to the replacement of Zn^{2+} with Ag^{+} ions, as they possess a larger ionic radius (radius is 0.074 nm for Zn^{2+} ions and 0.126 for Ag^{+} ions). As discussed in [39], an increase in lattice constants can be achieved either by the incorporation of Ag^{+} ions into the ZnO lattice or by the substitution of Ag^{+} ions with Zn^{2+} ions.

3.3. XPS Analysis

The XPS technique was applied to obtain an insight into the surface composition of Ag-doped ZnO nanoparticles. In Figure 6, the full XPS spectrum of Ag-doped ZnO NP is presented for a sample where 3000 pulses were used for Ag deposition in PLD. The presence of characteristic peaks can be identified for zinc (Zn 2p, Zn 3s, Zn 3p, Zn 3d, and Auger peaks Zn LMM), oxygen (O 1s and Auger peak O KLL), silver (Ag 3d, shown in inset) and carbon (C 1s). The spectrum indicates that Ag-doped ZnO nanoparticles are successfully synthesized.

The XPS high-resolution spectra are shown in Figure 7 for the following peaks: (a) Zn $2p_{3/2}$, (b) Ag 3d, (c) O 1s, and (d) C 1s. Deconvolution of the Zn $2p_{3/2}$ peak (Figure 7a) reveals that a gaussian distribution with a maximum at 1021.5 eV, which corresponds to Zn^{2+} states in the ZnO crystal lattice [40], is dominant. The origin of the gaussian distribution with a maximum at 1019.7 eV is unclear, but its influence is small. Among the Ag 3d states (Figure 7b), the Ag $3d_{5/2}$ peak at 367.3 eV and Ag $3d_{3/2}$ peak at 373.3 eV are present, which are probably related to Ag-O bonds, because the same binding energies are characteristic for Ag_2O [41]. The expected binding energies of the Ag 3d state for pure metallic silver are 368.3 eV for Ag $3d_{5/2}$ and 374.3 eV za Ag $3d_{5/2}$, while their absence, as is the case here, points to the conclusion that silver appears not in the form of metallic Ag nanoparticles but is incorporated in ZnO. Deconvolution of the O 1s (Figure 7c) peak results in two gaussian fits, first with a maximum at 529.9 eV, related to oxygen that builds up in the ZnO crystal lattice, and second with a maximum at 531.6 eV that is related to hydroxyl (O-H) oxygen [39]. Deconvolution of C 1s states (Figure 7d) results also in two gaussian fits, first with a maximum at 288.6 eV, related to C=O bonds, and second with a maximum of 284.7 eV, related to C-C bonds [42]. Carbon occurs as a sample impurity.

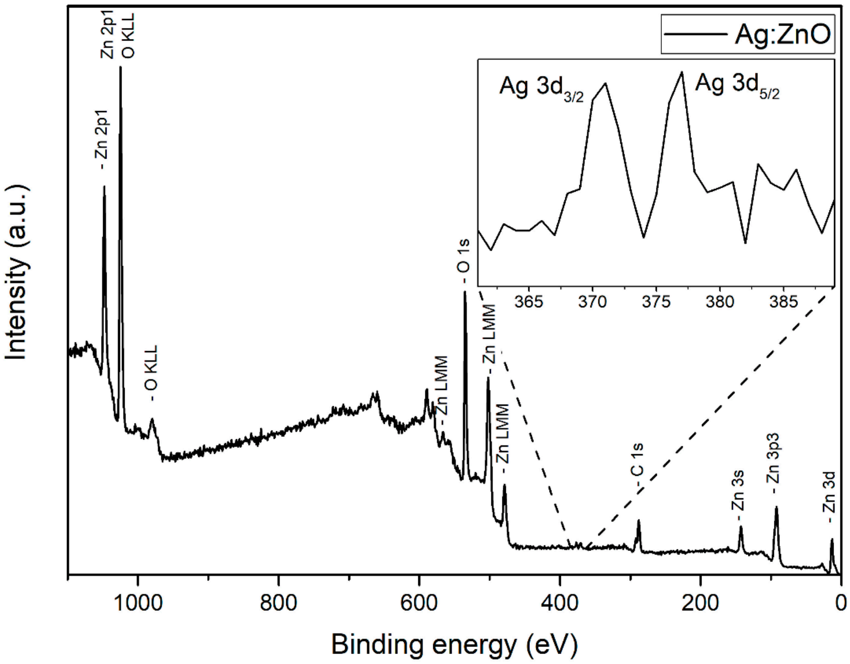

Figure 6. XPS spectrum of Ag-doped ZnO NP (3000 pulses used for Ag deposition in PLD).

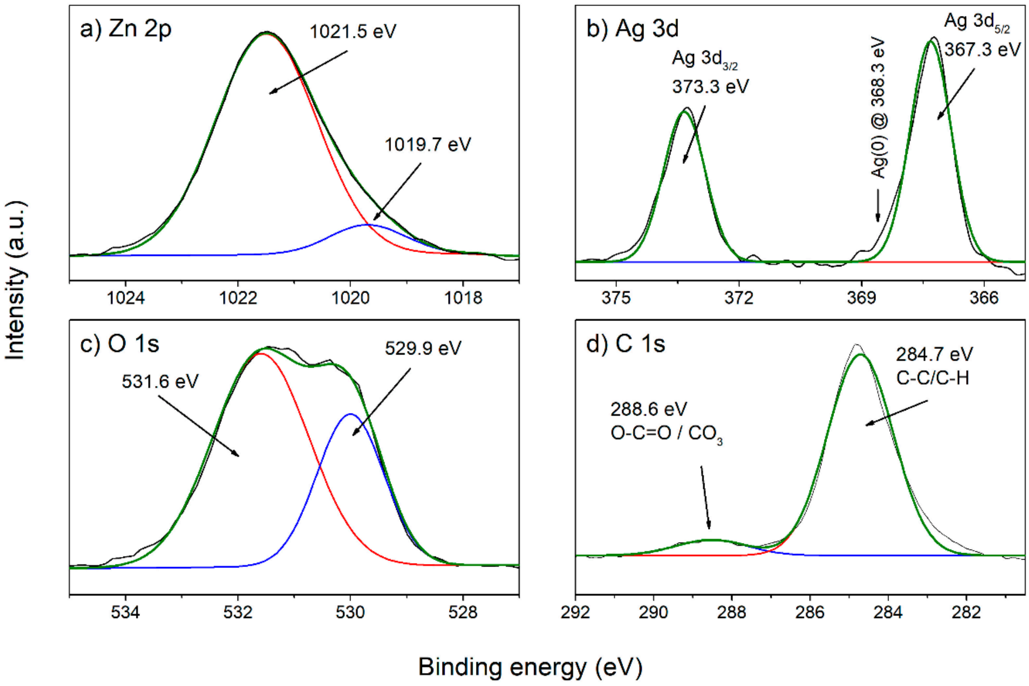

Figure 7. High-resolution spectra of Ag-doped ZnO NP (3000p used for Ag deposition in PLD) with fit spectra for (**a**) Zn $2p_{3/2}$, (**b**) Ag 3d, (**c**) O 1s and (**d**) C 1s.

XPS spectral data are used for the atomic ratio calculation for each element present in the XPS spectrum (Zn, O, Ag, and C). From atomic ratios, after subtraction of impurities, the Ag weight ratio in ZnO NP can be calculated, but such calculated value pertains only to the depth range 3–5 nm monitored by XPS. In Figure 8, the Ag weight ratio (calculated using XPS data), which is dependent on the number of pulses used for Ag deposition in PLD, is shown. It can be observed that the Ag silver ratio grows while the PLD number of pulses increases, up to a maximal value of 4.5 wt.% at 3000 pulses.

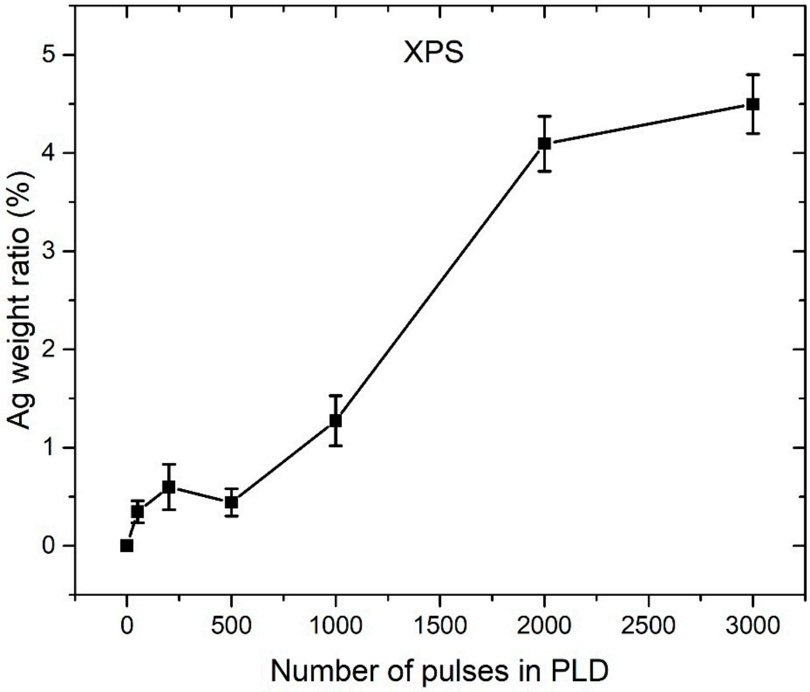

Figure 8. XPS calculated Ag weight ratio in PLAL-synthesized Ag-doped ZnO NP, which is dependent on number of pulses used for Ag deposition in PLD synthesis of PLAL target.

3.4. ICP-OES Measurements

ICP-OES measurements revealed that Zn mass concentration in each colloidal solution is approximately the same and has the value of 80 ± 3 mg/L. Under the assumption that the majority of synthesized colloidal material is Ag-doped ZnO, the mass concentration of ZnO is calculated to be 101 ± 3 mg/L. The Ag weight ratio in colloidal particles is estimated from the ICP-OES results, under the assumption (justified from XRD and XPS analysis) that the majority of Ag atoms are incorporated in ZnO. Figure 9 shows the ICP-OES calculated Ag weight ratio in Ag-doped ZnO NPs for a different number of pulses used for Ag deposition during PLD. It can be observed that the Ag weight ratios calculated from ICP-OES (Figure 9) are much smaller than those obtained from XPS (Figure 8). For instance, in the sample where 3000 pulses were used for Ag deposition in PLD, the Ag weight ratio calculated from XPS is 4.5%, while ICP-OES gives 0.55%, which is 8 times smaller. In the ICP-OES measurements, all colloidal material from the solution is included, while XPS monitors only in the 3–5 nm depth range and only at specific points on the samples. The Ag weight ratios obtained from ICP-OES have much higher accuracy, but large XPS values point to the conclusion that Ag atoms are mostly concentrated close to the ZnO surface.

In Figure 9, it can be observed that the Ag weight ratio growth slows down with the increasing number of pulses. Such a relation is probably related to the similar dependence of a number of deposited Ag atoms at the ZnO substrate on a number of laser pulses during PLD. There are a few possible explanations for such a relation. First, incident Ag atoms from the plasma plume formed during ablation in the PLD process could have enough energy to induce sputtering of other Ag atoms that are already deposited on the ZnO substrate. Secondly, Ag ions are positively charged, so the deposited Ag film could also be positively charged because the ZnO substrate lays on an ungrounded base. Therefore, incident Ag ions could be electrically repulsed from the Ag film, and this repulsion is expected to be larger when more Ag atoms are already present in the Ag film. The deposition rate is expected to decrease while increasing the number of pulses in PLD. Thirdly, by increasing the number of pulses in PLD, the average number of pulses that hits the same position of the Ag target also grows. It means that the focusing conditions deteriorate with irradiation time, so the same energy of the laser beam is distributed over a larger area of the Ag target. Therefore, single plasma species created during ablation have lower average energy, which means that a smaller number of Ag atoms have sufficient energy for reaching the ZnO substrate.

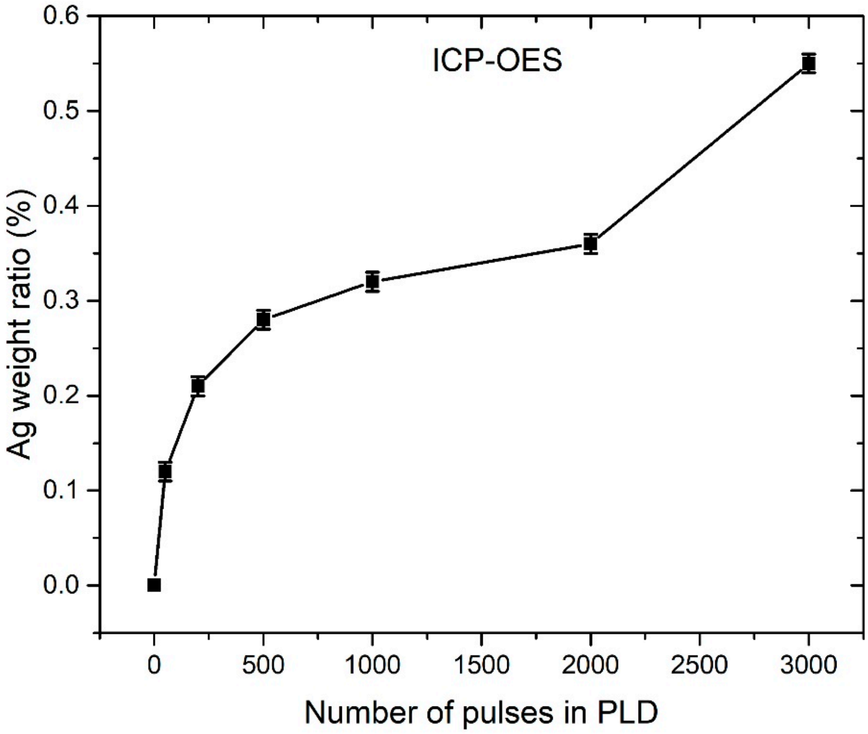

Figure 9. ICP-OES calculated Ag weight ratio in PLAL-synthesized Ag-doped ZnO NP that is dependent on number of pulses used for Ag deposition in PLD synthesis of PLAL target.

3.5. Photoabsorption Measurements

In Figure 10, photoabsorbance measurements are shown for the colloidal solutions of pure ZnO NP and Ag-doped ZnO NP synthesized by ablation of the ZnO target, covered with an Ag layer deposited with 1000 pulses in PLD. The UV–Vis spectra differ in intensity, where the Ag-doped ZnO colloidal solution has higher absorbance in the visible part of the spectrum and lower absorbance in the UV part concerning absorbances for pure ZnO NP. The total mass of Zn measured by ICP-OES is 79 mg/L and 85 mg/L for Ag-doped and pure ZnO, respectively. From the similarity of those masses, it can be concluded that a similar amount of material is involved in photocatalysis. The UV–Vis spectra differ either since Ag-doped ZnO NPs are larger than pure ZnO NPs, which was not found in the SEM observations (it applies to all samples), or that in the Ag-doped ZnO NP solution, more material crystallizes in irregular shaped structures, which is hard to quantify from SEM images. One must note that the metallic Ag peak with a maximum at about 400 nm [43] is not visible, and this further confirms that Ag is incorporated in the ZnO crystal lattice, rather than appearing in the form of pure Ag NPs.

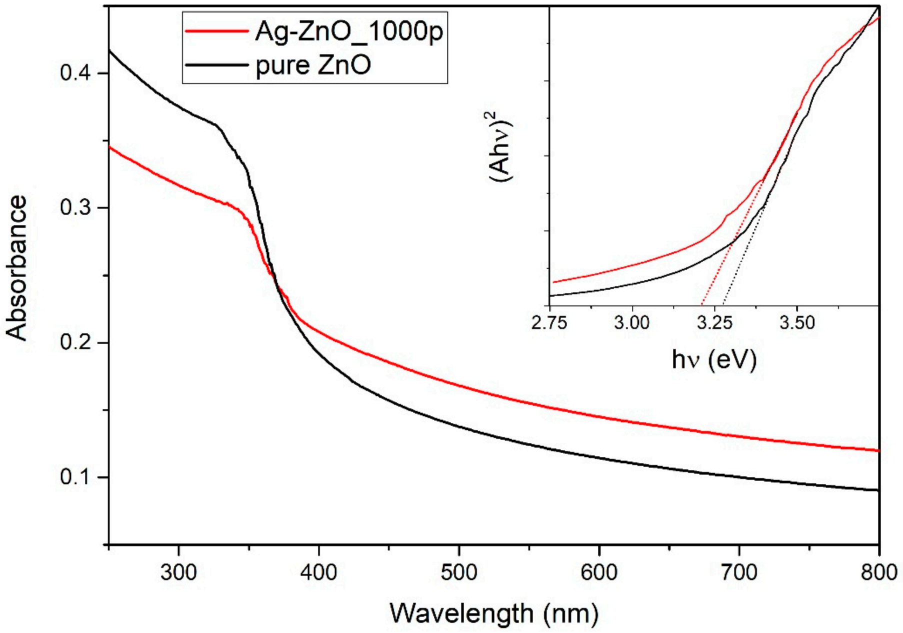

Figure 10. Photoabsorbance spectrum of colloidal solutions of pure ZnO NPs and Ag-doped ZnO NPs synthesized with 1000 pulses in PLD.

Photoabsorbance measurements of the as-synthesized Ag-doped ZnO NP colloidal solutions (as shown in Figure 10) were used for bandgap calculations. Tauc plot for direct bandgap calculation ($(Ah\nu)^2$ vs. $h\nu$) was used to determine the bandgap of pure and Ag-doped ZnO NPs. Tauc plots for pure ZnO NP and Ag-doped ZnO NPs (produced with 1000 pulses in PLD) are shown in the inset of Figure 10. The direct bandgap is calculated as the intercept on the x-axis of the linear part of the Tauc curve and has a value of 3.27 eV for pure and 3.21 eV for Ag-doped ZnO. It was found that the bandgap energies gradually drop from 3.27 eV for pure to 3.14 eV for Ag-doped ZnO produced with 3000 pulses in PLD. It is evident that the bandgap energy decreases when the Ag weight ratio increases. It implies that the incorporated Ag ions influence the narrowing of the bandgap of ZnO, extending the absorption to the visible part of the spectrum, and thus leading to more efficient absorption of light.

3.6. Photocatalytic Efficiency Determination

In order to measure the photocatalytic efficiency of Ag-doped ZnO NPs, the MB photodegradation process during UV irradiation was monitored for 1 hour in 10 min steps for each sample. In Figure 11, the example of a gradual decrease in the photoabsorbance curve during irradiation time is shown. In this example, ZnO NPs are synthesized by using 1000 Ag pulses in PLD. The photoabsorbance maximum decreased from 2.15 to 0.60 (or by 73%) during 60 min of irradiation, which points to the relatively strong photocatalytic activity of Ag-doped ZnO NPs.

The photocatalytic activity of Ag-doped ZnO NPs is based on the excitation of the electrons from the valence band (VB) to the conduction band (CB) under light irradiation that is equal or higher than the band-gap energy. When electrons are excited, holes are formed in the VB that act as positive charge carriers. The unique Ag/ZnO Fermi level is below the bottom of the ZnO CB, so photo-excited electrons flow from ZnO to the Ag surface (Ag is an “electron sink”), while the holes remain on the ZnO surface. Moreover, silver doping can increase photocatalytic activity by creating band levels that act as traps for charge carriers. Therefore, the recombination rate of electrons and holes decreases, and their lifetime increases [14]. New band levels can also lead to effective band-gap narrowing that expands the range of photon energies, which can lead to photocatalytic efficiency in the visible part of the spectrum [12]. Silver, as a plasmonic metal, strongly enhances the light absorption via surface plasmon resonance (SPR), increasing the number of excited electrons and holes in the catalyst, consequently leading to higher photocatalytic performance [12]. Ag usually has a higher value of work function (4.3 eV [44]) than the absolute value of ZnO electron affinity (about 4.1 eV [45]). When the balance between the Fermi levels is established, the Schottky barrier is formed at ZnO/Ag [18]. The Schottky junction is the depleted area where a strong electric field separates the electrons and holes. This process decreases the e−/h+ recombination rate and, therefore, improves photocatalysis. In photocatalytic reactions, electrons in the CB react with O_2, generating superoxide anions ($\cdot O_2^-$), while holes in the VB react with H_2O, generating hydroxyl radicals (·OH). Therefore, these free radicals participate in the photodegradation of organic dyes, such as MB [46–48]. In [48], Ag-doped ZnO nanocatalysts were synthesized using the co-precipitation method. Intriguingly, a scavenger test was carried out to determine the radicals that affect MB photodegradation. The results showed that photo-generated holes and ·OH radicals are the main species, while $\cdot O_2^-$ radicals are the supportive species in the photodegradation process of MB. We assume that the same radicals dominate in our case, as the crystallinity of the nanoparticles and Ag weight ratios are similar.

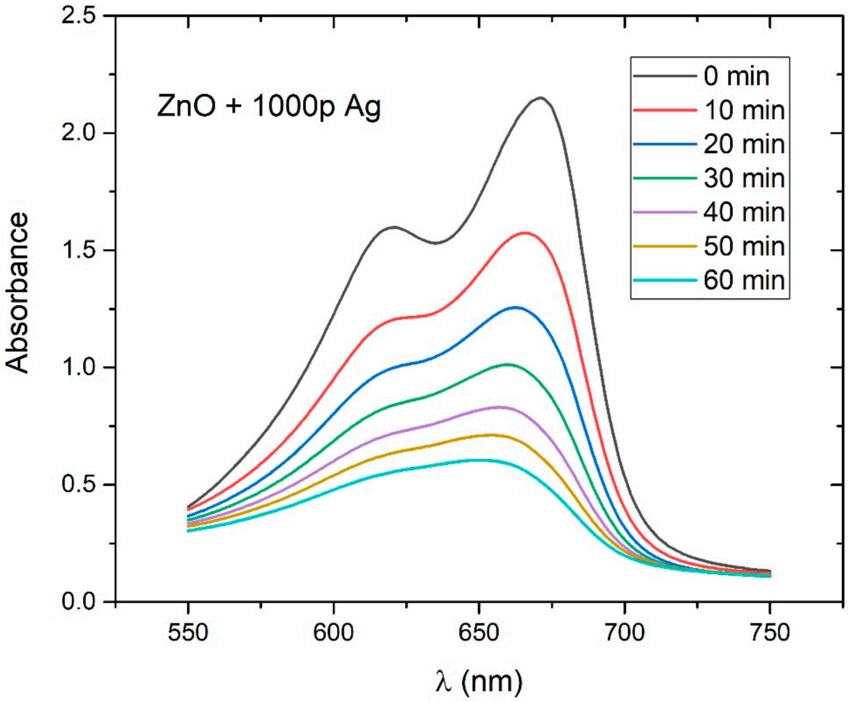

Figure 11. Photocatalytic degradation of MB in PLAL-synthesized colloidal solution of Ag-doped ZnO NPs (1000p used for Ag deposition in PLD) under UV irradiation.

The photodegradation rates (k_{DR}) were calculated by the following equation, assuming that the reaction follows pseudo-first-order kinetics:

$$C = C_0 \cdot e^{-k_{DR} \cdot t} \tag{5}$$

where C is a concentration of MB at time t, C_0 is an initial MB concentration, k_{DR} is the degradation rate, and t is the irradiation time. In Figure 12, the $\ln(C/C_0)$ vs. t plot is shown for each sample, where C/C_0 is the ratio between the time-dependent concentration C of MB and initial concentration C_0 of MB. C and C_0 are, according to the Beer–Lambert law, proportional to the corresponding values of photoabsorbance maxima, from which the photoabsorbance of the solution without MB (zero-curve) is distracted, so C/C_0 is simply calculated as the ratio between these photoabsorbance values. Photodegradation rate k_{DR} is calculated as the slope of the linear fit in $\ln(C/C_0)$ vs. t plot for each case.

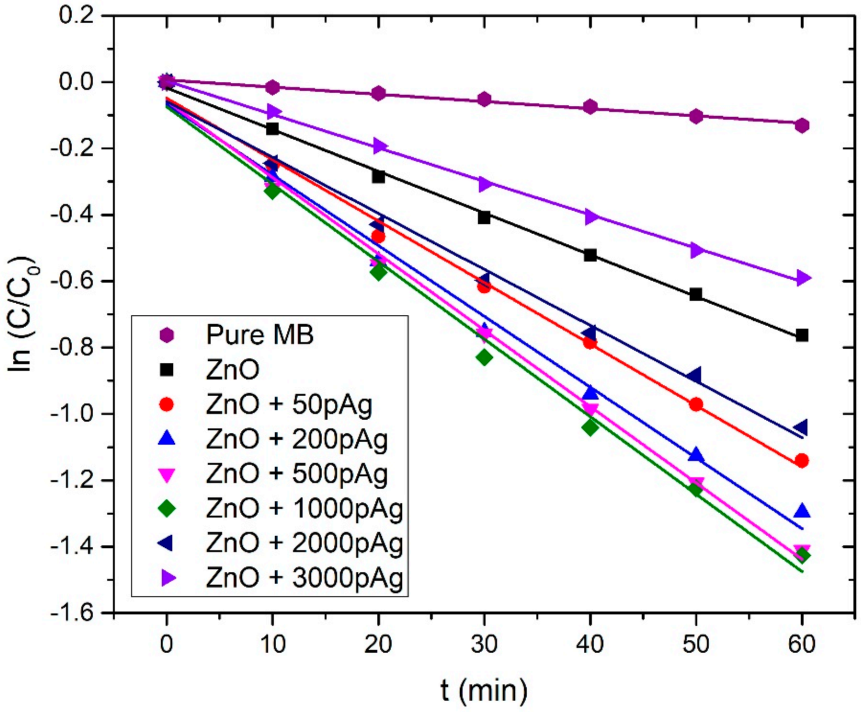

Figure 12. $\ln(C/C_0)$ as a function of time for photocatalytic degradation of MB in different ZnO NP colloidal solutions under UV irradiation.

Table 2 summarizes the Ag weight ratios in Ag-doped ZnO NPs calculated from ICP-OES, the photodegradation rates, and corresponding photodegradation half-times for each irradiated colloidal solution.

Table 2. MB photodegradation rates and photodegradation half-times under UV irradiation, derived from pseudo-first order reaction model for different Ag weight ratios in colloidal ZnO catalyst.

Solution	Ag Weight Ratio (ICP-OES)/%	k_{DR}/min^{-1}	$t_{1/2}$/min
Pure MB	/	0.00217	319.4
ZnO	0	0.0126	55.0
ZnO_50Ag	0.12	0.0185	37.5
ZnO_200Ag	0.21	0.0213	32.5
ZnO_500Ag	0.28	0.0230	30.1
ZnO_1000Ag	0.32	0.0233	29.7
ZnO_2000Ag	0.36	0.0169	41.0
ZnO_3000Ag	0.55	0.0101	68.6

In Figure 13, the dependence of the photodegradation rate on Ag weight ratio in ZnO NPs is shown. The photodegradation rate for the pure ZnO NP colloidal solution is 0.0126 min^{-1}. As we introduce Ag dopant and increase its mass concentration in the nanoparticles, the photodegradation rate increases. It reaches a maximum value of 0.0233 min^{-1} for 0.32 Ag wt.% (1000p in PLD), which is almost the same as 0.230 min^{-1}, the value achieved for 0.28 Ag wt.% (500p in PLD). For the higher concentrations of Ag (2000 and 3000 pulses in PLD), the photodegradation rate decreases and drops to the value of 0.0101 min^{-1} for 0.55 Ag wt.% (3000p in PLD), which is lower than the photodegradation rate of pure ZnO NP. The existence of an optimal Ag dopant ratio for maximization of photocatalytic activity is observed in numerous papers [13,49–54] and mostly has a value between 0.5 wt.% and 2.5 wt.%. The growth of $k_{DR,}$ while increasing the Ag ratio in ZnO

NP, can be explained as an interplay of the Ag doping effects, which are favorable for photocatalysis, such as decreased recombination rate due to induced Ag intraband levels, improved charge separation, bandgap narrowing, and the SPR effect. The decrease in k_{DR} in the Ag dopant ratios that are larger than the optimal ratio can be caused by several effects. For example, defects induced in the ZnO crystal lattice, due to the presence of the Ag material, can act as recombination centers for electron–hole pairs and decrease their lifetime [20]. This is attributed to the electrostatic attraction of positively charged holes and negatively charged Ag. Other reasons include the decreased available area for UV light absorption and decreased reactant adsorption due to the presence of Ag at the ZnO surface [27]. This leads to the decrease in the photons absorbed by ZnO NP, lowering the photocatalytic reaction efficiency. Furthermore, decrease in the holes reacting with organic pollutants at the ZnO surface can occur. As was concluded from the comparison of the Ag ratios calculated by ICP-OES and XPS, the Ag atoms are probably found mostly close to the surface of the ZnO catalyst. Their contribution to all the mentioned effects, either beneficial or detrimental for photocatalysis, is larger than in the case of homogenous doping. The reason is that both light irradiation and photocatalytic interactions occur at the catalyst surface. In addition, this is probably the reason why the optimal Ag weight ratio for maximization of photocatalytic activity, calculated from ICP-OES, which considers the whole volume of the catalyst material, is relatively low (0.32 wt.%). The large decrease in k_{DR} from 0.0233 min^{-1} to 0.0169 min^{-1}, which occurs while increasing the silver weight ratio by a very small amount (from 0.32% to 0.36%, ICP-OES), can be explained by the fact that at the same time, the silver weight ratio close to the ZnO surface drastically increased (from 1.3% to 4.1%, XPS).

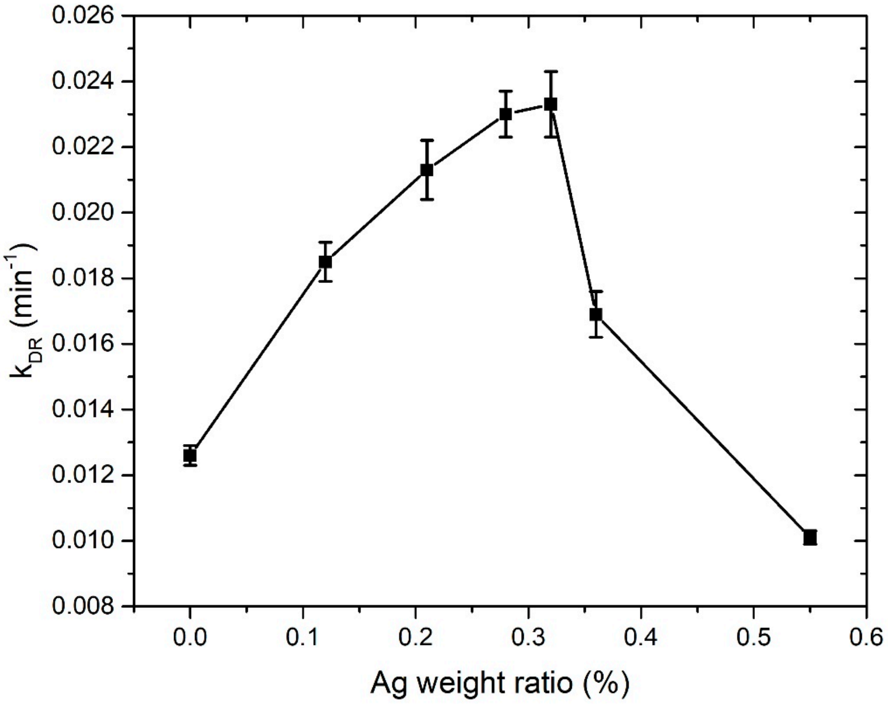

Figure 13. Photodegradation rate dependence on ICP-OES calculated Ag weight ratio in Ag-doped ZnO NPs.

It is interesting to compare the obtained results with results in similar works [21,50,51,54]. In [50], 95.6% photodegradation efficiency of amaranth dye was achieved after 4 h with the addition of 1% of Ag to ZnO, but with a total amount of catalyst of 160 mg/L. In our case, 73% of MB photodegradation after one hour was achieved with a catalyst amount of around 100 mg/L. These two cases cannot be directly compared but can serve as a point to assess the efficiency of photocatalysis presented in this work. In other papers, the amount of catalyst is not reported, so a direct comparison with our work cannot be made. In [51], the photocatalytic behavior of nanostructured sol-gel synthesized Ag-doped ZnO films for degradation of MB under UV irradiation was studied. The optimal weight ratio of the Ag dopant was 0.5%, with an MB photodegradation rate that was 1.6 times larger (0.039 min^{-1}) when compared with pure ZnO (0.024 min^{-1}). This is a slightly lower improvement than that achieved in our work (2 times larger k_{DR}), while comparing the cases with optimal Ag doping and pure ZnO. In [54], Ag-doped ZnO NPs were synthesized by combining the co-precipitation method and HILF (hybrid induction and laser heating) technique and their photocatalytic efficiency was analyzed for MB degradation under UV irradiation. The largest MB photodegradation rate (0.126 min^{-1}–85% in 15 min) was achieved for the Ag/Zn ratio of 2%, which corresponds to the Ag weight ratio of 2.5 wt.%. It is about 5 times larger than the one obtained for pure ZnO NPs (0.024 min^{-1}–30% in 15 min). In [21], Ag-doped ZnO NPs were synthesized by the co-precipitation method and photodegradation of brilliant green dye under UV irradiation was examined in their presence. Optimal photocatalytic efficiency (0.031 min^{-1}) was obtained at the Ag weight ratio of 2%, and it is 2.6 times better than the one obtained for pure ZnO (0.012 min^{-1}). Here, the strong bandgap narrowing is also noticed, from 3.09 eV for pure ZnO to 2.79 eV for 2% Ag-doped ZnO. Although optimal Ag doping in papers [21,54] increased the photodegradation rate of ZnO more than in the case of the present paper (5 and 2.6 compared to 2), it should be noted that in these papers, it is achieved at much larger Ag weight ratios (2.5 wt.% and 2 wt.% compared to 0.32%). A low optimal Ag ratio, such as that achieved in this paper, can be an advantage from the cost-effectivity point of view.

4. Conclusions

Ag-doped ZnO NPs are successfully synthesized using the combination of PLD and PLAL laser methods. The difference in silver weight ratio calculated by XPS and ICP-OES points to the conclusion that the silver atoms prevail close to the ZnO NP surface, and therefore have a greater impact on ZnO photocatalytic efficiency than in the case of homogenous doping. The largest photocatalytic efficiency is obtained by using ZnO NPs doped with 0.32 wt.% silver, with an MB photodegradation rate that is twice as large as that obtained in the presence of pure ZnO NP. The photocatalytic efficiency is improved by silver doping, due to its favorable impacts on photocatalysis, such as decreasing the recombination rate caused by inducing energy levels in the ZnO band gap, which acts as charge carrier traps and the activity of ZnO is evident, implying good effectivity of silver as a doping material.

5. Patents

Croatian patent application involves the method of production of two-component nanoparticles using a laser (patent application number P20211098A).

Supplementary Materials: The following supporting information can be downloaded at: https://www.mdpi.com/article/10.3390/nano12152677/s1, Figure S1: Photographs of experimental setups PLD (on the left) and PLAL (on the right). Figure S2: UV lamp emission spectrum with VIS, UVA, UVB and UVC irradiation intensities.

Author Contributions: D.B.: synthesis of nanoparticles, photocatalysis test, analysis and discussion of results and writing of manuscript; D.M.: synthesis of nanoparticles; R.R.: synthesis of nanoparticles, photocatalysis test and text revision; S.Ž.: ICP-OES measurements; M.M.: ICP-OES measurements and discussion of results; N.K.: analysis and discussion of results, writing of manuscript, conceptual design of experiment and project management. All authors have read and agreed to the published version of the manuscript.

Funding: This work was mainly supported by the Croatian Science Foundation under project HrZZ-PZS-2019-02-5276.

Data Availability Statement: Not applicable.

Acknowledgments: This work was mainly supported by the Croatian Science Foundation under project HrZZ-PZS-2019-02-5276 and to a lesser extent by the Croatian-Serbian bilateral project. D.M. is also grateful to the Institute of Physics Belgrade, the Ministry of Education, Science and Technological Development, Republic of Serbia and the Centre of Excellence Non-Equilibrium Processes. IPB. S.Ž. and M.M. thank the Ministry of Education, Science and Technological Development of the Republic of Serbia for the financial support to the research through institutional funding and bilateral project between Serbia and Croatia (contract numbers 451-03-68/2022-14/200017 and 337-00-205/2019-09/15).

Conflicts of Interest: The authors declare no conflict of interest.

References

1. Özgür, Ü.; Alivov, Y.I.; Liu, C.; Teke, A.; Reshchikov, M.A.; Doğan, S.; Avrutin, V.; Cho, S.-J.; Morkoç, H. A Comprehensive Review of ZnO Materials and Devices. *J. Appl. Phys.* **2005**, *98*, 041301. [CrossRef]
2. Klingshirn, C.F. ZnO: Material, Physics and Applications. *ChemPhysChem* **2007**, *8*, 782–803. [CrossRef] [PubMed]
3. Singh, R.; Barman, P.B.; Sharma, D. Synthesis, Structural and Optical Properties of Ag Doped ZnO Nanoparticles with Enhanced Photocatalytic Properties by Photo Degradation of Organic Dyes. *J. Mater. Sci. Mater. Electron.* **2017**, *28*, 5705–5717. [CrossRef]
4. Chen, H.; Wan, J.; Wu, H.; Liu, C. Effective encapsulation of ZnO thin film transistors controlled by thermal energy. *Appl. Surf. Sci.* **2021**, *548*, 149253. [CrossRef]
5. He, J.; Xu, P.; Zhou, R.; Li, H.; Zu, H.; Zhang, J.; Qin, Y.; Liu, X.; Wang, F. Combustion Synthesized Electrospun InZnO Nanowires for Ultraviolet Photodetectors. *Adv. Electron. Mater.* **2022**, *8*, 2100997. [CrossRef]
6. Espitia, P.J.P.; Soares, N.D.F.F.; Coimbra, J.S.; de Andrade, N.J.; Cruz, R.S.; Medeiros, E.A. Zinc Oxide Nanoparticles: Synthesis, Antimicrobial Activity and Food Packaging Applications. *Food Bioprocess. Technol.* **2012**, *5*, 1447–1464. [CrossRef]
7. Jayaprakash, N.; Sureshb, R.; Rajalakshmi, S.; Rajae, S.; Sundaravadivel, E.; Gayathrif, M.; Sridharan, M. One Step Synthesis, Characterisation, Photocatalytic and Bio-Medical Applications of ZnO Nanoplates. *Mater. Technol.* **2020**, *35*, 112–124. [CrossRef]
8. Raza, W.; Faisal, S.M.; Owais, M.; Bahnemann, D.; Muneer, M. Facile Fabrication of Highly Efficient Modified ZnO Photocatalyst with Enhanced Photocatalytic, Antibacterial and Anticancer Activity. *RSC Adv.* **2016**, *6*, 78335–78350. [CrossRef]
9. Ashebir, M.E.; Tesfamariam, G.M.; Nigussie, G.Y.; Gebreab, T.W. Structural, Optical, and Photocatalytic Activities of Ag-Doped and Mn-Doped ZnO Nanoparticles. *J. Nanomater.* **2018**, *2018*, 9425938. [CrossRef]
10. Ma, H.; Williams, P.L.; Diamond, S.A. Ecotoxicity of Manufactured ZnO Nanoparticlese—A Review. *Environ. Pollut.* **2013**, *172*, 76–85. [CrossRef] [PubMed]
11. Blažeka, D.; Car, J.; Klobučar, N.; Jurov, A.; Zavašnik, J.; Jagodar, A.; Kovačević, E.; Krstulović, N. Photodegradation of Methylene Blue and Rhodamine b Using Laser-Synthesized Zno Nanoparticles. *Materials* **2020**, *13*, 4357. [CrossRef] [PubMed]
12. Qi, K.; Cheng, B.; Yu, J.; Ho, W. Review on the Improvement of the Photocatalytic and Antibacterial Activities of ZnO. *J. Alloys Compd.* **2017**, *727*, 792–820. [CrossRef]
13. Hosseini, S.M.; Sarsari, I.A.; Kameli, P.; Salamati, H. Effect of Ag Doping on Structural, Optical, and Photocatalytic Properties of ZnO Nanoparticles. *J. Alloys Compd.* **2015**, *640*, 408–415. [CrossRef]
14. Ebrahimi, R.; Hossienzadeh, K.; Maleki, A.; Ghanbari, R.; Rezaee, R.; Safari, M.; Shahmoradi, B.; Daraei, H.; Jafari, A.; Yetilmezsoy, K.; et al. Effects of Dopig Zinc Oxide Nanoparticles with Transition Metals (Ag, Cu, Mn) on Photocatalytic Degradation of Direct Blue 15 Dye under UV and Visible Light Irradiation. *J. Environ. Health Sci. Eng.* **2019**, *17*, 479–492. [CrossRef]
15. Kumar, S.; Singh, V.; Tanwar, A. Structural, Morphological, Optical and Photocatalytic Properties of Ag-Doped ZnO Nanoparticles. *J. Mater. Sci. Mater. Electron.* **2016**, *27*, 2166–2173. [CrossRef]
16. Nigussie, G.Y.; Tesfamariam, G.M.; Tegegne, B.M.; Weldemichel, Y.A.; Gebreab, T.W.; Gebrehiwot, D.G.; Gebremichel, G.E. Antibacterial Activity of Ag-Doped TiO_2 and Ag-Doped ZnO Nanoparticles. *Int. J. Photoenergy* **2018**, *2018*, 5927485. [CrossRef]
17. Sharma, N.; Kumar, J.; Thakur, S.; Sharma, S.; Shrivastava, V. Antibacterial Study of Silver Doped Zinc Oxide Nanoparticles against Staphylococcus Aureus and Bacillus Subtilis. *Drug Invent. Today* **2013**, *5*, 50–54. [CrossRef]
18. Liu, Y.; Wei, S.; Gao, W. Ag/ZnO Heterostructures and Their Photocatalytic Activity under Visible Light: Effect of Reducing Medium. *J. Hazard. Mater.* **2015**, *287*, 59–68. [CrossRef]
19. Alammar, T.; Mudring, A.V. Facile Preparation of Ag/ZnO Nanoparticles via Photoreduction. *J. Mater. Sci.* **2009**, *44*, 3218–3222. [CrossRef]
20. Chauhan, R.; Kumar, A.; Chaudhary, R.P. Photocatalytic Studies of Silver Doped ZnO Nanoparticles Synthesized by Chemical Precipitation Method. *J. Sol.-Gel Sci. Technol.* **2012**, *63*, 546–553. [CrossRef]
21. Gnanaprakasam, A.; Sivakumar, V.M.; Thirumarimurugan, M. A Study on Cu and Ag Doped ZnO Nanoparticles for the Photocatalytic Degradation of Brilliant Green Dye: Synthesis and Characterization. *Water Sci. Technol.* **2016**, *74*, 1426–1435. [CrossRef] [PubMed]
22. Muñoz-Fernandez, L.; Sierra-Fernandez, A.; Milošević, O.; Rabanal, M.E. Solvothermal Synthesis of Ag/ZnO and Pt/ZnO Nanocomposites and Comparison of Their Photocatalytic Behaviors on Dyes Degradation. *Adv. Powder Technol.* **2016**, *27*, 983–993. [CrossRef]

23. Karunakaran, C.; Rajeswari, V.; Gomathisankar, P. Enhanced Photocatalytic and Antibacterial Activities of Solgel Synthesized ZnO and Ag-ZnO. *Mater. Sci. Semicond. Process.* **2011**, *14*, 133–138. [CrossRef]
24. Abinaya, C.; Mayandi, J.; Osborne, J.; Frost, M.; Ekstrum, C.; Pearce, J.M. Inhibition of Growth of S. Epidermidis by Hydrothermally Synthesized ZnO Nanoplates. *Mater. Res. Express* **2017**, *4*, 075401. [CrossRef]
25. Whang, T.J.; Hsieh, M.T.; Chen, H.H. Visible-Light Photocatalytic Degradation of Methylene Blue with Laser-Induced Ag/ZnO Nanoparticles. *Appl. Surf. Sci.* **2012**, *258*, 2796–2801. [CrossRef]
26. Dermenci, K.B.; Genc, B.; Ebin, B.; Olmez-Hanci, T.; Gürmen, S. Photocatalytic Studies of Ag/ZnO Nanocomposite Particles Produced via Ultrasonic Spray Pyrolysis Method. *J. Alloys Compd.* **2014**, *586*, 267–273. [CrossRef]
27. Height, M.J.; Pratsinis, S.E.; Mekasuwandumrong, O.; Praserthdam, P. Ag-ZnO Catalysts for UV-Photodegradation of Methylene Blue. *Appl. Catal. B Environ.* **2006**, *63*, 305–312. [CrossRef]
28. Yang, G. *Laser Ablation in Liquids*, 1st ed.; Pan Stanford Publishing: Singapore, 2012.
29. Anugrahwidya, R.; Yudasari, N.; Tahir, D. Optical and Structural Investigation of Synthesis ZnO/Ag Nanoparticles Prepared by Laser Ablation in Liquid. *Mater. Sci. Semicond. Process.* **2020**, *105*, 104712. [CrossRef]
30. Ahmed, S.M.; Imam, H. Characterization and Photocatalytic Activity of Eu:ZnO & Au/Eu:ZnO Nanoparticles Prepared by Laser Ablation in Water. *Mater. Sci. Semicond. Process.* **2020**, *115*, 105128. [CrossRef]
31. Sahoo, A.; Miryala, M.; Dixit, T.; Klimkowicz, A.; Francis, B.; Murakami, M.; Rao, M.S.R.; Krishnan, S. Femtosecond Pulse Ablation Assisted Mg-ZnO Nanoparticles for UV-Only Emission. *Nanomaterials* **2020**, *10*, 1326. [CrossRef]
32. Chelnokov, E.; Rivoal, M.; Colignon, Y.; Gachet, D.; Bekere, L.; Thibaudau, F.; Giorgio, S.; Khodorkovsky, V.; Marine, W. Band gap tuning of ZnO nanoparticles via Mg oping by femtosecond laser ablation in liquid environment. *Appl. Surf. Sci.* **2012**, *258*, 9408–9411. [CrossRef]
33. Krstulović, N.; Blažeka, D.; Car, J.; Maletić, D.; Rakić, M. Method of Production of Two-Component Nanoparticles Using Laser. Croatia Patent P20211098A, 9 July 2021.
34. Moulder, J.F.; Stickle, W.F.; Sobol, P.E.; Bomben, K.D. *Handbook of X-ray Photoelectron Spectroscopy: A Reference Book of Standard Spectra for Identification and Interpretation of XPS Data*; Chastain, J., Ed.; Physical Electronics Inc.: Eden Prairie, MN, USA, 1995.
35. Lupan, O.; Chow, L.; Ono, L.K.; Cuenya, B.R.; Chai, G.; Khallaf, H.; Park, S.; Schulte, A. Synthesis and Characterization of Ag- or Sb-Doped ZnO Nanorods by Facile Hydrothermal Route. *J. Phys. Chem. C* **2010**, *114*, 12401–12408. [CrossRef]
36. Ntwaeaborwa, O.M.; Mofokeng, S.J.; Kumar, V.; Kroon, R.E. Structural, optical and photoluminescence properties of Eu^{3+} doped ZnO nanoparticles. *Spectrochim. Acta Part A Mol. Biomol. Spectrosc.* **2017**, *182*, 42–49. [CrossRef]
37. Mustapha, S.; Ndamitso, M.M.; Abdulkareem, A.S.; Tijani, J.O.; Shuaib, D.T.; Mohammed, A.K.; Sumaila, A. Comparative study of crystallite size using Williamson-Hall and Debye-Scherrer plots for ZnO nanoparticles. *Adv. Nat. Sci. Nanosci. Nanotechnol.* **2019**, *10*, 045013. [CrossRef]
38. Krstulović, N.; Salamon, K.; Budimlija, O.; Kovač, J.; Dasović, J.; Umek, P.; Capan, I. Parameters optimization for synthesis of Al-doped ZnO nanoparticles by laser ablation in water. *Appl. Surf. Sci.* **2018**, *440*, 916–925. [CrossRef]
39. Gruzintsev, A.N.; Volkov, V.T.; Yakimov, E.E. Photoelectric properties of ZnO films doped with Cu and Ag acceptor impurities. *Semiconductors* **2003**, *37*, 259–262. [CrossRef]
40. Narath, S.; Koroth, S.K.; Shankar, S.S.; George, B.; Mutta, V.; Wacławek, S.; Černík, M.; Padil, V.V.T.; Varma, R.S. Cinnamomum Tamala Leaf Extract Stabilized Zinc Oxide Nanoparticles: A Promising Photocatalyst for Methylene Blue Degradation. *Nanomaterials* **2021**, *11*, 1558. [CrossRef]
41. Tjeng, L.H.; Meinders, M.B.J.; van Elp, J.; Ghijsen, J.; Sawatzky, G.A.; Johnson, R.L. Electronic structure of Ag_2O. *Phys. Rev. B* **1990**, *41*, 3190. [CrossRef]
42. Rakkesh, R.A.; Durgalakshmi, D.; Balakumar, S. Beyond Chemical Bonding Interaction: An Insight into the Growth Process of 1D ZnO on Few-Layer Graphene for Excellent Photocatalytic and Room Temperature Gas Sensing Applications. *ChemistrySelect* **2018**, *3*, 7302–7309. [CrossRef]
43. Car, J.; Blažeka, D.; Bajan, T.; Krce, L.; Aviani, I.; Krstulović, N. A quantitative analysis of colloidal solution of metal nanoparticles produced by laser ablation in liquids. *Appl. Phys. A* **2021**, *127*, 838. [CrossRef]
44. Lefort, A.; Akbi, M.; Parizet, M.-J. Experimental Determination of Work Function of Silver Alloys. In Proceedings of the XVI International Symposium on Discharges and Electrical Insulation in Vacuum, Moscow, Russia, 23–30 May 1994; Volume 2259, pp. 486–490. [CrossRef]
45. Hussain, B.; Aslam, A.; Khan, T.M.; Creighton, M.; Zohuri, B. Electron Affinity and Bandgap Optimization of Zinc Oxide for Improved Performance of Zno/Si Heterojunction Solar Cell Using PC1D Simulations. *Electron.* **2019**, *8*, 238. [CrossRef]
46. Sabry, R.S.; Rahmah, M.I.; Aziz, W.J. A systematic study to evaluate effects of stearic acid on superhydrophobicity and photocatalytic properties of Ag-doped ZnO nanostructures. *J. Mater. Sci. Mater.* **2020**, *31*, 13382–13391. [CrossRef]
47. Kareem, M.A.; Bello, I.T.; Shittu, H.A.; Sivaprakash, P.; Adedokun, O.; Arumugam, S. Synthesis, characterization, and photocatalytic application of silver doped zinc oxide nanoparticles. *Clean. Mater.* **2022**, *3*, 100041. [CrossRef]
48. Shelar, S.G.; Mahajan, V.K.; Patil, S.P.; Sonawane, G.H. Effect of doping parameters on photocatalytic degradation of methylene blue using Ag doped ZnO nanocatalyst. *SN Appl. Sci.* **2020**, *2*, 820. [CrossRef]
49. Riaz, A.; Ashraf, A.; Taimoor, H.; Javed, S.; Akram, M.A.; Islam, M.; Mujahid, M.; Ahmad, I.; Saeed, K. Photocatalytic and Photostability Behavior of Ag- and/or Al-Doped ZnO Films in Methylene Blue and Rhodamine B under UV-C Irradiation. *Coatings* **2019**, *9*, 202. [CrossRef]

50. Pascariu, P.; Cojocaru, C.; Samoila, P.; Airinei, A.; Olaru, N.; Rusu, D.; Rosca, I.; Suchea, M. Photocatalytic and antimicrobial activity of electrospun ZnO:Ag nanostructures. *J. Alloys Compd.* **2020**, *834*, 155144. [CrossRef]
51. Kakhki, R.M.; Tayebee, R.; Ahsani, F. New and highly efficient Ag doped ZnO visible nano photocatalyst for removing of methylene blue. *J. Mater. Sci. Mater. Electron.* **2017**, *28*, 5941–5952. [CrossRef]
52. Yıldırım, Ö.A.; Unalan, H.E.; Durucan, C. Highly Efficient Room Temperature Synthesis of Silver-Doped Zinc Oxide (ZnO:Ag) Nanoparticles: Structural, Optical, and Photocatalytic Properties. *J. Am. Ceram. Soc.* **2013**, *96*, 766–773. [CrossRef]
53. Divband, B.; Khatamian, M.; Eslamian, G.R.K.; Darbandi, M. Synthesis of Ag/ZnO nanostructures by different methods and investigation of their photocatalytic efficiency for 4-nitrophenol degradation. *Appl. Surf. Sci.* **2013**, *284*, 80–86. [CrossRef]
54. Wang, R.; Xin, J.H.; Yang, Y.; Liu, H.; Xu, L.; Hu, J. The Characteristics and Photocatalytic Activities of Silver Doped ZnO Nanocrystallites. *Appl. Surf. Sci.* **2004**, *227*, 312–317. [CrossRef]

nanomaterials

Article

Synthesis of Silver, Gold, and Platinum Doped Zinc Oxide Nanoparticles by Pulsed Laser Ablation in Water

Rafaela Radičić, Dejan Maletić, Damjan Blažeka, Julio Car and Nikša Krstulović *

Institute of Physics, Bijenička cesta 46, 10000 Zagreb, Croatia
* Correspondence: niksak@ifs.hr

Abstract: In this paper, we propose a simple two-step method for the synthesis of Ag, Au, and Pt-doped ZnO nanoparticles. The method is based on the fabrication of targets using the pulsed laser deposition (PLD) technique where thin layers of metals (Ag, Pt, Au) have been deposited on a metal-oxide bulk substrate (ZnO). Such formed structures were used as a target for the production of doped nanoparticles (ZnO: Ag, ZnO: Au, and ZnO: Pt) by laser ablation in water. The influence of Ag, Au, and Pt doping on the optical properties, structure and composition, sizing, and morphology was studied using UV-Visible (UV-Vis) and photoluminescence (PL) spectroscopies, X-ray diffraction (XRD), X-ray photoelectron spectroscopy (XPS), scanning electron microscopy (SEM), and transmission electron microscopy (TEM), respectively. The band-gap energy decreased to 3.06, 3.08, and 3.15 for silver, gold, and platinum-doped ZnO compared to the pure ZnO (3.2 eV). PL spectra showed a decrease in the recombination rate of the electrons and holes in the case of doped ZnO. SEM, TEM, and AFM images showed spherical-shaped nanoparticles with a relatively smooth surface. The XRD patterns confirm that Ag, Au, and Pt were well incorporated inside the ZnO lattice and maintained a hexagonal wurtzite structure. This work could provide a new way for synthesizing various doped materials.

Keywords: zinc oxide (ZnO); doped ZnO; silver (Ag) doped ZnO; gold (Au) doped ZnO; platinum (Pt) doped ZnO; pulsed laser deposition (PLD); pulsed laser ablation in liquid (PLAL); nanoparticles

check for updates

Citation: Radičić, R.; Maletić, D.; Blažeka, D.; Car, J.; Krstulović, N. Synthesis of Silver, Gold, and Platinum Doped Zinc Oxide Nanoparticles by Pulsed Laser Ablation in Water. *Nanomaterials* **2022**, *12*, 3484. https://doi.org/10.3390/nano12193484

Academic Editors: Maurizio Muniz-Miranda, Sergei Kulinich and Alberto Villa

Received: 1 September 2022
Accepted: 27 September 2022
Published: 5 October 2022

1. Introduction

In nanotechnology, nanoparticles—particles in the range of 1 to 100 nm in diameter—have a significant role due to their exceptional magnetic, electrical, mechanical, optical, and electronic properties with respect to the bulk materials [1]. These unique properties allow the use of nanoparticles in energy harvesting [2], sensing [3], optics [4], photocatalysis [5], cosmetics [6], medicine [7], and biology [8]. Metal oxide nanoparticles excel as the most used nanomaterials due to their various properties, such as being adsorbents to heavy metals or having unique opto-electrical properties, catalytic sensitivity, and selective activity [9].

Beside pure metallic nanoparticles, two-component (alloyed) and metal-oxide nanoparticles represent advanced functional materials, which have high impact in a wide variety of applications in science and technology [10]. Such nanoparticles can be fabricated directly from alloyed targets by PLAL in a form of core-shell nanoparticles [11], alloyed nanoparticles [12], or as hybrid nanostructures where PLAL nanoparticles are adsorbed on the support or nanostructured surfaces [13,14].

Among metal oxide nanoparticles, zinc oxide (ZnO) is one of the most prominent and widely used materials for gas and chemical sensors [15], optical and electrical devices [16], solar cells [17], water treatment [18], antimicrobial activity [19], food packaging [20], and drug delivery [21]. ZnO is an inorganic n-type semiconductor with a direct bandgap of 3.37 eV and binding energy of 60 meV at room temperature. It has unique physicochemical properties, such as piezoelectricity [22], pyroelectric effects [23], good electron transport [24], and photo- and sono-catalytic activities [25]. ZnO strongly absorbs UVA (315–400 nm) and

UVB (280–315 nm) light [19], which is why it is one of the most effective sun protectors available. At ambient conditions, ZnO has a hexagonal wurtzite structure with intrinsic defects—O vacancies and Zn interstitials—resulting in n-type conductivity. Introducing a new element in the crystal structure of ZnO leads to the enhancement of the electrical and optical properties and broadens the area of its application [26]. For n-type doping, we can use group-III (Al, Ga, In), as substitutional elements for Zn, and group-VII (Cl, I), as substitutional elements for O. The big challenge is to obtain p-type doping in wide-gap semiconductors such as ZnO because of the native defects, hydrogen impurities, low solubility of the dopant, and deep impurity level [27]. Known acceptors for p-type doping are Group-I elements (Li, Na, K), Group-V elements (N, P, As), silver, copper, and Zn vacancies.

Various methods are developed for ZnO doping, such as chemical vapor deposition (CVP) [28], sol-gel [29], atomic layer deposition [30], pulsed laser deposition (PLD) [31], a wet chemical method [32], etc. Drawbacks of chemical methods are the usage of various chemicals in the synthesis process, toxic by-products, stabilizers, and capping agents, while high-vacuum methods can be complicated to handle and expensive. Pulsed laser ablation in liquid (PLAL) gained a lot of attention due to its fast production of nanoparticles with production rates of several grams per hour [33], simplicity, and effectiveness. In the PLAL technique, a pulsed laser beam ablates a metal plate immersed in a liquid where plasma is formed on the surface of the metal plate in the focus of the high-power laser beam. There is an energy exchange from the plasma to the liquid, where a cavitation bubble forms. Eventually, particles are released from the cavitation bubble into the surrounding liquid. Produced nanoparticles have high purity (ligand-free), and their size and shape depend on the ablation parameters (laser wavelength and fluence, repetition rate, ablation time, and liquid environment) [34]. Furthermore, there is no limit on the type of produced nanoparticles because every metal target can be ablated. Since there are no toxic by-products, the method can be classified as eco-friendly.

According to the literature, researchers successfully produced doped ZnO using a nanosecond or femtosecond pulsed laser in a liquid environment. Sahoo et al. [35] generated Mg-doped ZnO nanoparticles in ethanol using a Ti: Sapphire femtosecond laser. The Mg: ZnO target was prepared by grinding together the MgO and ZnO powders. After that, the mixture was compressed and sintered at 1200 °C for 24 h. Also, Chelnokov et al. [36] produced Mg-doped ZnO nanoparticles where the target was prepared from mixtures of Zn and Mg acetylacetonates. The mixture was manually mixed and heated for one hour at 130 °C to evaporate water and then calcined for three hours at 350 °C to destroy organics. Lastly, the mixture was compressed and sintered for two days at 700 °C. The Mg: ZnO nanoparticles were synthesized in ethanol by Ti: Sapphire femtosecond laser. Qin et al. [37] generated Cu-doped ZnO quantum dots using an ns-Nd: YAG laser in Polyvinylpyrrolidone (PVP) aqueous solution. The Zn/Cu composite targets were synthesized by a chemical replacement method. Yudasari et al. [38] employed an ns-Nd: YAG laser for Fe-doped ZnO nanoparticle production using the Zn and Fe targets. Firstly, the Zn plate was ablated in pure water. Then, the Zn plate was replaced with a Fe plate. Lastly, Fe: ZnO nanoparticles were generated by ablating the Fe plate in the ZnO colloidal solution. With this method, Anugrahwidya et al. [39] produced Ag-doped ZnO nanoparticles, and Khashan et al. [40] synthesized indium-doped ZnO. Krstulović et al. [41] used ns-Nd: YAG laser for ZnO: Al_2O_3 target ablation in MiliQ water and, consequently, produced Al-doped ZnO nanoparticles. To our knowledge, PLAL was not used for Au and Pt-doped ZnO nanoparticle synthesis.

In this work, we present a newly developed synthesis method for Ag, Au, and Pt-doped ZnO that combines the PLD and the PLAL processes. With PLD, we created ZnO-X (X-Au, Ag, Pt) targets for the ablation process in water using ns-Nd: YAG laser. The advantage of this target synthesis is simplicity and fast production compared to the previous methods.

2. Experimental Procedure

2.1. Material Preparation

The X: ZnO (X-Ag, Au, Pt) doped nanoparticles were synthesized in a two-step process shown in Figure 1. Firstly, we deposited a thin layer of Ag, Au, and Pt (purity > 99.9%, GoodFellow, Huntingdon, UK) on ZnO ceramic (purity > 99.99%, GoodFellow, Huntingdon, UK) substrates using the pulsed laser deposition (PLD) method in order to obtain targets for the PLAL process (Figure 1a). The deposition was performed in a vacuum (10^{-4} mbar) while the target and substrate were rotated to avoid the drilling of the target and to ensure homogeneous film deposition on the substrate. The laser pulse number was set to 2000 for all samples. In the second step, ZnO-X (X-Ag, Au, Pt) targets were used in the PLAL process for obtaining X: ZnO (X-Ag, Au, Pt) doped nanoparticle solutions (Figure 1c,d). The targets were immersed 2.5 cm under water in a glass beaker filled with 25 mL MiliQ water. The ablation process was carried out by an Nd: YAG (Quantel, Brilliant, Les Ulis, France) laser with the wavelength and pulse output energy of 1064 nm and 300 mJ, respectively. The pulse duration and repetition rate were 5 ns and 5 Hz, while the ablation time was 6 min and 40 s (2000 pulses). The energy delivered to the sample was approximately 120 mJ per pulse, and the fluence of a single laser pulse was 79 J/cm^2. The laser beam was focused on the target using a cylindrical concave lens with a focal length of 10 cm. The incident angle of the laser beam was 90°. During the ablation, the targets were continuously scanned to avoid drilling. The detailed schematics and procedure of the two-step synthesis of doped nanoparticles can be found here [42]. Also, we measured the weight of ZnO substrates before and after the PLD and PLAL synthesis using a microbalance (XPR6UD5, Mettler Toledo, Columbus, OH, USA) to obtain the masses of deposited metal layers and ablated nanoparticles, respectively.

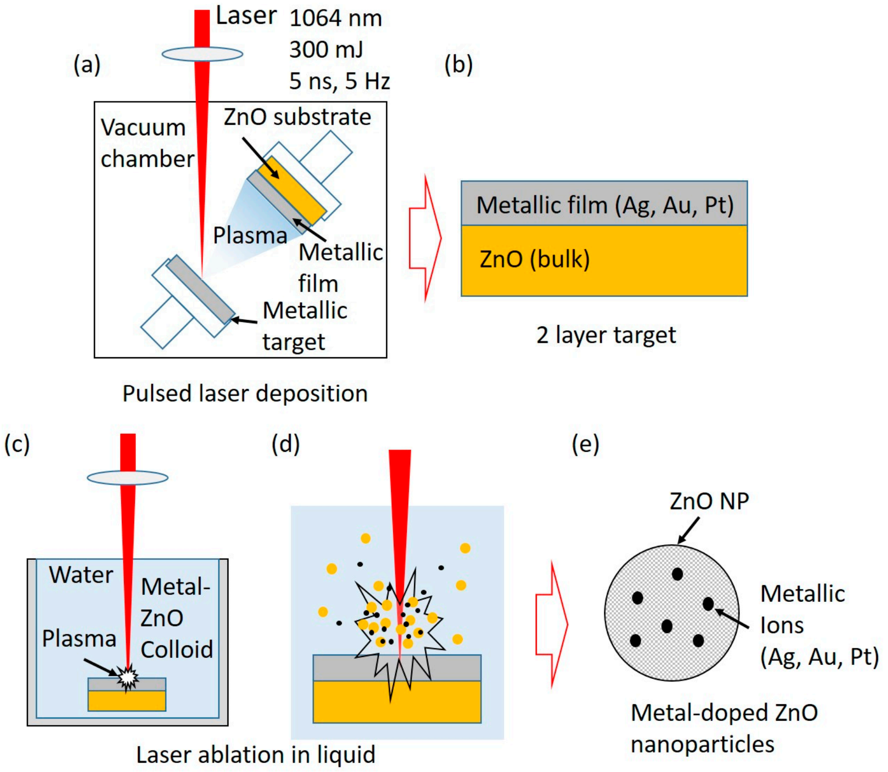

Figure 1. Two-step synthesis method of Ag, Au, and Pt-doped ZnO nanoparticles. First step is (**a**) pulsed laser deposition (PLD) of Ag, Au, and Pt on the ZnO substrate. As result, (**b**) a two-layered target (ZnO-metallic film) is formed. In the second step, (**c**,**d**) a two-layer target is ablated in water, forming (**e**) Ag, Au, and Pt-doped ZnO NPs.

2.2. Material Characterization

The optical absorption properties of the X: ZnO (X-Ag, Au, Pt) nanoparticles in the colloidal solution were obtained via a UV-Vis spectrophotometer (Lambda 25, Perkin Elmer, Waltham, MA, USA) in the wavelength range from 220–800 nm. The UV-Vis absorption spectra were measured for nanoparticle colloidal solutions using a UV cuvette with a path length of 10 mm. Furthermore, optical properties were observed by photoluminescence (PL) spectroscopy. The photoluminescence measurements were obtained using a spectrofluorophotometer (RF-6000, Shimadzu, Kyoto, Japan) under an Xe lamp at the excitation energy of 3.54 eV (wavelength of 350 nm). Moreover, the colloidal solutions were dropped on silicon wafers and dried in a dryer (SP-25 Easy, Kambič, Semič, Slovenia) at 40 °C for 30 min for further characterization.

Structural analysis was carried out with the grazing incidence X-ray diffraction (GIXRD) technique. The measurements were performed in a diffractometer containing a Cu X-ray (λ = 1.5406 Å) tube and a W/C multilayer for monochromatization and beam shaping (D5000, Siemens, Karlsruhe, Germany). A curved position sensitive detector (RADICON) collected the diffracted spectra in the angular range 2θ = 30–85°. For all measurements, we used a fixed grazing incidence angle of $\alpha_i = 1.5°$. The following JCPDS cards were used for crystallographic analysis: JCPDS 36-1451 (ZnO), JCPDS 04-0783 (Ag), JCPDS 04-0784 (Au), and JCPDS 01-087-0640 (Pt).

The detailed morphology and size distribution of the nanoparticles were studied using a scanning electron microscope (SEM, Joel 7600F, Tokyo, Japan) and a transmission electron microscope (TEM, JEOL JEM-1400 Flash, Tokyo, Japan). The SEM measurements were obtained by dropping a colloidal solution on a 5×5 mm^2 Si wafer, while for the TEM images, samples were prepared by dropping one drop of a colloidal solution onto the TEM grid. All colloidal solutions were sonicated for 5 min before the dropping.

The chemical compositions were analyzed using an X-ray photoelectron spectroscope (PHI-TFA XPS, Physical Electronics Inc., Chanhassen, MN, USA) equipped with a monochromatic Al source at the photon energy of 1486.6 eV. The analyzed area and depth were 0.4 mm (in diameter) and 3–5 nm, respectively. The high-energy resolution spectrum was obtained with an energy analyzer, operating at a resolution of about 0.6 eV and pass energy of 29 eV. During data analysis, the spectrum was calibrated by setting the C 1s peak at 284.8 eV, characteristic of the C-C/C-H bonds. Quantification of surface composition was performed from XPS peak intensities, considering the relative sensitivity factors provided by the instrument manufacturer [43].

3. Results and Discussion

3.1. Mass and Atomic Fractions

Weighing the doped ZnO target before and after laser ablation reveals the mass and atomic fractions of dopants in the ZnO matrix. Table 1 shows masses of deposited Ag, Au, and Pt thin film on ZnO substrates. Pulsed laser deposition was the most effective for Ag thin film. The thickest film deposits in the case of silver. The amount of ablated material depends on the composition, geometry, and ablation threshold of the target, the focus and wavelength of the laser, the number of pulses, and the surrounding fluid in which the ablation takes place [34]. The pulsed laser ablation process was the most effective for Pt-doped ZnO nanoparticles, producing 1.925 mg in 6 min and 40 s. However, in this paper, we are focused on 2000 pulses (6 min and 40 s) for all three samples. From the obtained masses, we calculated the mass and atomic fractions of Ag, Au, and Pt in relation to the ZnO. The atomic fractions of Ag, Au, and Pt in ZnO were 2.32, 0.55, and 0.41%, respectively. Since the band-gap tuning of a semiconductor depends on the atomic fraction of impurity introduced into the crystal lattice, we can conclude that in this case, Ag would have the most effect on the band-gap narrowing.

Table 1. Mass measurements of deposited metal layers involved in ablation and ablated doped ZnO nanoparticles (NP). Also, the mass (w) and atomic (at.) fractions of Ag, Au, and Pt in the produced nanoparticles were calculated.

PLD		PLAL			w (%)	at. (%)
m (Ag)	0.036 mg	m (Ag: ZnO)	1.171 mg	Ag	3.37 ± 0.2	2.32 ± 0.2
m (Au)	0.024 mg	m (Au: ZnO)	1.798 mg	Au	1.33 ± 0.1	0.55 ± 0.1
m (Pt)	0.019 mg	m (Pt: ZnO)	1.925 mg	Pt	1.01 ± 0.1	0.42 ± 0.1

3.2. Optical Analysis

Using the UV-Vis spectrophotometer, we obtained the absorption spectra of the samples and extracted information about the optical band-gap energy. Figure 2 shows the UV-Vis absorption spectra of the pure and Ag, Au, and Pt doped ZnO nanoparticles in colloidal solution. We can distinguish characteristic ZnO peaks in the UV region between 300–400 nm due to intrinsic absorption when electrons transition from the valence band to the conduction band ($O_{2p} \rightarrow Zn_{3d}$) [44]. By introducing Ag, Au, and Pt into the ZnO lattice, we have a broad absorption peak at about 335, 331, and 328 nm, respectively. We observed a red-shift of the Ag: ZnO and Au: ZnO NP absorption peaks compared to the Pt: ZnO peak. This implies a narrower optical band-gap in the case of Ag- and Au-doped ZnO [45]. A red-shift of the absorption peak can be connected to the development of shallow levels inside the band-gap due to the presence of impurity atoms present in the ZnO lattice [46]. From Table 1, we can notice that the highest atomic content of dopant in ZnO is in the case of Ag. This strongly indicates that Ag-doped ZnO will have the narrowest band-gap. Moreover, we do not see characteristic peaks of the Ag, Au, and Pt in ZnO spectrums, signifying the fact that these metals are incorporated into the crystal lattice of ZnO. We have different intensities in absorbance due to different solution densities.

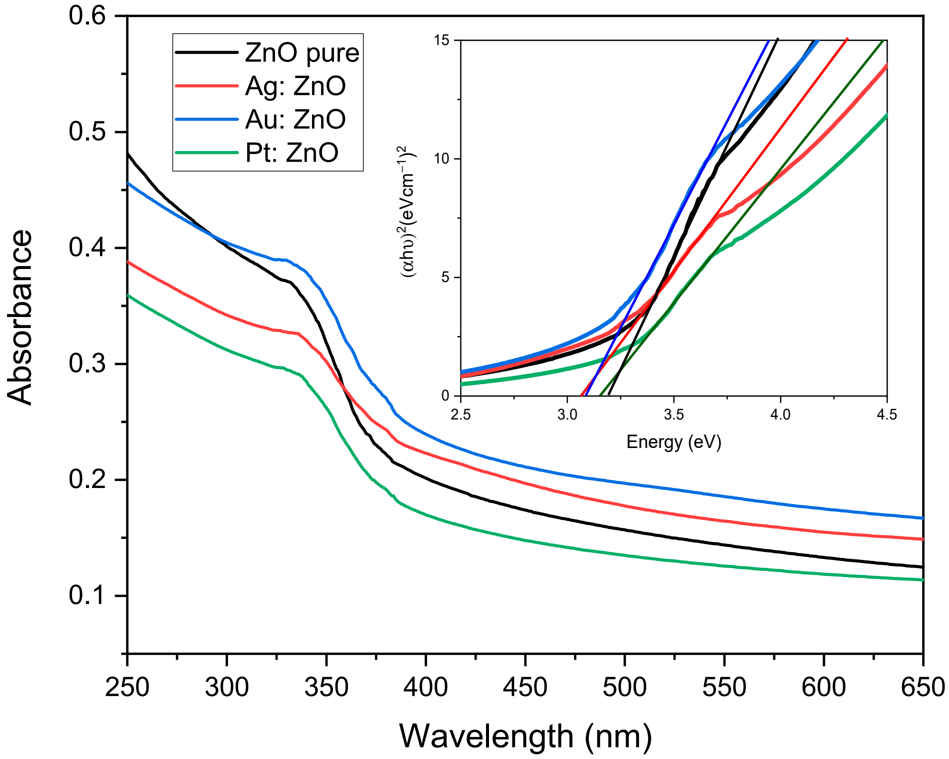

Figure 2. UV-Vis absorption spectra of the pure and Ag, Au, and Pt doped ZnO nanoparticles. The inset represents the Tauc plot of the same spectra showing the band-gap energies of 3.06 eV, 3.08 eV, 3.15 eV, and 3.20 eV for the Ag: ZnO, Au: ZnO, Pt: ZnO, and pure ZnO, respectively.

Direct band-gap energies were obtained by extrapolating the linear part in a plot $(\alpha h\nu)^2$ versus $E_g = h\nu$ (inset in Figure 2) following equation:

$$(\alpha h\nu)^2 = A\left(h\nu - E_g\right) \tag{1}$$

where α is the absorption coefficient, h is Planck's constant, $h\nu$ is the photon energy, A is a constant, and E_g is the optical band-gap. The estimated band-gap energies are 3.06 ± 0.02 eV, 3.08 ± 0.02 eV, 3.15 ± 0.03 eV, and 3.20 ± 0.04 eV for the Ag: ZnO, Au: ZnO, Pt: ZnO, and pure ZnO, respectively. There is a decrease in the band-gap energies in the case of the doped ZnO NPs showing changes in the nanocrystal electronic structure of the doped ZnO [46] and more efficient light absorption. The narrowest band-gap energy has Ag-doped ZnO NPs because of the highest atomic content inside ZnO. Also, our synthesized ZnO has lower band-gap energy compared to the literature value of 3.37 eV [27].

The photoluminescence (PL) spectra (Figure 3) obtained at room temperature offer an insight into the optical properties of the pure and doped ZnO NPs. Typical PL ZnO spectra consist of the peaks in the UV region related to the near-band-edge emission and the visible region attributed to the deep-level emissions. The peak at 3.26 eV (380 nm) for pure and doped ZnO is ascribed to the recombination of the electron and hole pairs (exciton recombination) aligning with the near-band edge of ZnO [47,48]. For doped ZnO NPs, the peak decreases compared to the pure ZnO, implying a decrease in the recombination rate of the electrons and holes. The emission peak at 3.12 eV (398 nm) can be attributed to the electronic transition from a lower energy excitonic state or to the Zn interstitial, which lies ~0.22 eV below the conduction band [49]. As it can be seen from the inset in Figure 3, the emission peak at 3.12 eV is well fitted with Zn_i interstitial [50]. Pure ZnO displays a yellow emission with a maximum at ~2.11 eV (~588 nm), which is related to the exciton transition between charged oxygen vacancy in the valence band and the photo-accelerated electrons [51]. To understand the origin of such a broad emission, the fit with several Gaussian components was performed. It was found that all peaks are related to the emission from ZnO, while the doped ZnO emission was too low to be fitted. In the inset in Figure 3, a deconvolution of the visible peak (yellow emission) for pure ZnO is shown [50]. It is deconvoluted into four Gaussian sub-peaks assigned to oxygen interstitial O_i, oxygen vacancy double charge $V_O{}^{++}$, oxygen vacancy single charge $V_O{}^{+}$, and oxygen vacancy V_O with the following shares in the total emission 26%, 42%, 24%, and 8%, respectively. The calculation of shares for $V_O{}^{++}$ and O_i is done by extrapolating Gaussian fits, as they are obstructed by the second order of initial irradiation, which appears below 1.9 eV (the peak is at 1.77 eV). It was widely accepted that $V_O{}^{++}$ is mainly responsible for the yellow emission, as is the case here where it dominates over the emission of other defects [52]. Doping ZnO with Ag, Au, and Pt decreases the visible emission, implying a low defect concentration. As said, the decrease in the PL peaks indicates a lower recombination rate of the excitons and improves their optical properties. This happens because dopants create band levels that act as traps for charge carriers, thus decreasing the recombination rate of the electrons and holes. Comparing PL intensities, Pt-doped ZnO NPs have the lowest recombination rate of the excitons. Since the exciton recombination rate decreases with the ZnO doping, a better photocatalytic power of ZnO in the degradation of organic pollutants is expected [53].

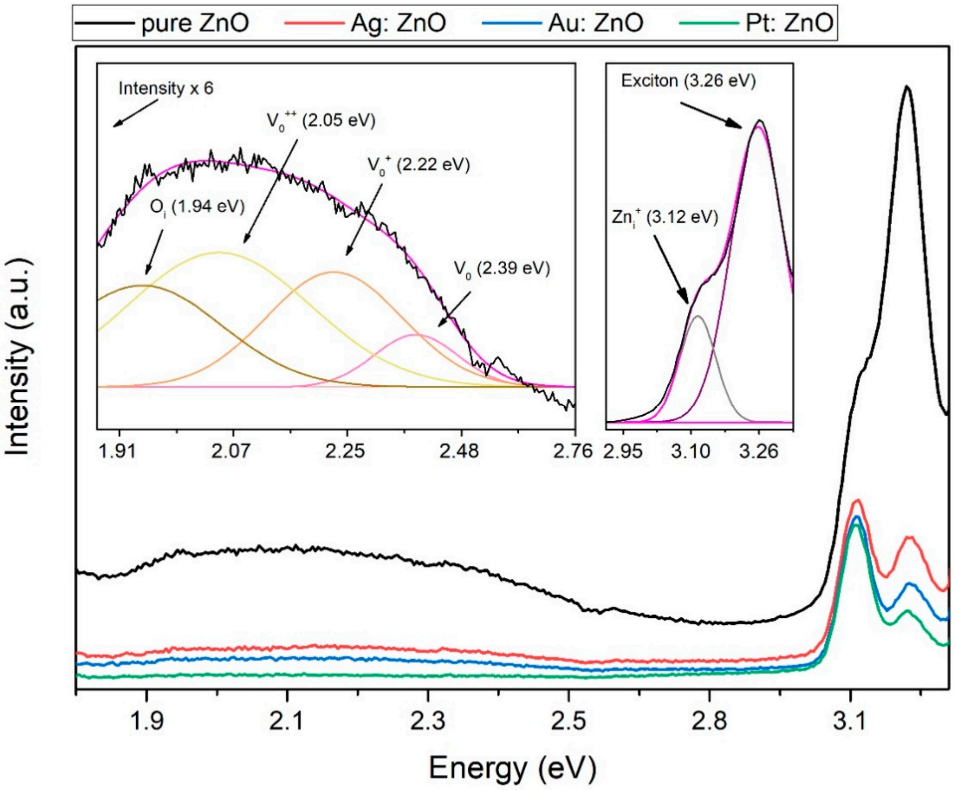

Figure 3. The photoluminescence (PL) spectra of pure and Ag, Au, and Pt doped ZnO NPs. In inset: Deconvolution plot in UV and visible part of PL spectrum (magenta line represent cumulative fit peak).

3.3. Structural Analysis

The XRD patterns reveal the crystal structure, purity, and crystallinity of the synthesized X: ZnO (X-Ag, Au, and Pt) nanoparticles. In Figure 4, all peaks are indexed as the hexagonal wurtzite structure of ZnO. The XRD peaks are relatively sharp indicating that X: ZnO nanoparticles are crystalline. Also, the XRD patterns are relatively broad because the crystals are randomly oriented, and we cannot exclude that a certain amount of amorphous ZnO and/or $Zn(OH)_2$ is present in the main phase [44]. There are no characteristic peaks of impurities in the pattern. The absence of Au, Ag, and Pt characteristic peaks in the X: ZnO nanoparticles excludes the existence of the Au-, Ag-, and Pt-based clusters within the detection limit. This strongly implies that Ag, Au, and Pt have been incorporated into the crystal structure of ZnO and that high-quality doped nanoparticles were produced.

The average crystallite size (*D*) was calculated using Debye–Scherrer's formula using data from the XRD patterns [54]:

$$D = \frac{0.9 \cdot \lambda}{\beta \cdot cos\theta} \tag{2}$$

where λ is the wavelength of the X-ray beam (1.5406 Å), β is the full width at half maximum (in radians), and θ is the angle between the plane and the incident ray (Bragg's angle, in radians). The calculated crystallite sizes are 50 nm, 24 nm, 25 nm, and 24 nm for pure ZnO, Ag: ZnO, Au: ZnO, and Pt: ZnO, respectively. Doped ZnO nanoparticles have smaller crystallites (half as small) compared to pure ZnO.

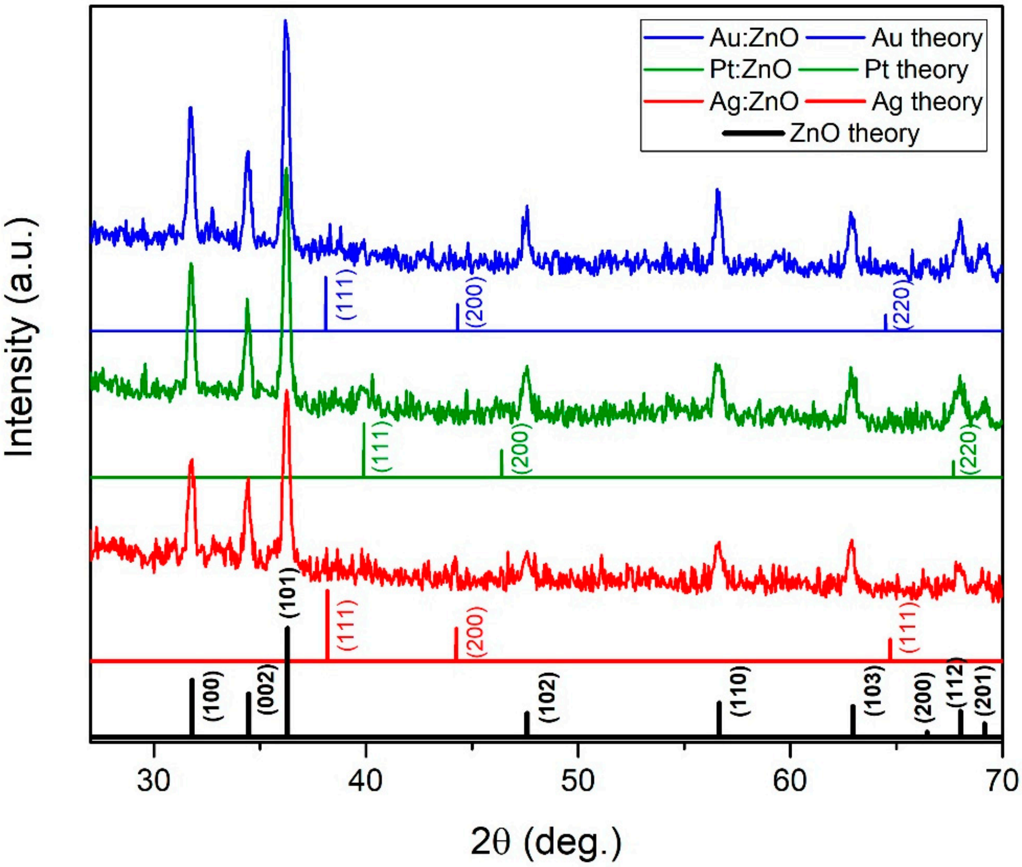

Figure 4. X-ray diffraction patterns of the Ag, Au, and Pt doped ZnO nanoparticles.

We observed shifts in the peaks of the hexagonal wurtzite structure (Figure 5) into smaller angles for the Ag: ZnO, Au: ZnO, and Pt: ZnO compared to the pure ZnO. These average shifts were 0.26° for Ag: ZnO, Au: ZnO, and Pt: ZnO. These shifts toward the smaller angles are attributed to the larger ionic radii of Ag^+ (1.15 Å), Au^+ (1.37 Å), and Pt^{2+} (0.8 Å) than Zn^{2+} (0.74 Å), which implies that Ag^+, Au^+, and Pt^{2+} substituted fraction of Zn^{2+} ions in the ZnO lattice. The sum of ionic radii (Ag + O, Au + O, Pt + O) is greater than the sum of ionic radii of Zn and O. Also, the bond lengths of Ag-O, Au-O, and Pt-O are longer than Zn-O in a hexagonal structure. This means that the unit cell should expand, and consequently, XRD peaks shift towards smaller angles. Similarly, Anugrahwidya et al. reported a shift in the main peak towards the smaller Bragg angles when Ag atoms substituted Zn atoms [39]. According to the literature, when a dopant has a bigger ionic radius than the matrix atom, then peaks shift towards smaller angles (e.g., Fe, Mn, In) [38,55,56]. On the contrary, when a dopant has a smaller ionic radius than the matrix atom, then peaks move towards higher values (e.g., Mg, Cu, Co, Ni) [35,37,55].

Lattice constants a (for (100) plane) and c (for (200) plane) can be calculated using the following formulae [54]:

$$a = \frac{\lambda}{\sqrt{3} \cdot sin\theta} \tag{3}$$

$$c = \frac{\lambda}{sin\theta} \tag{4}$$

From Table 2, it is apparent that the lattice constants a and c are larger for Ag-, Au-, and Pt-doped ZnO NPs compared to pure ZnO. With this calculation, we are confirming the lattice expansion of the doped ZnO NPs.

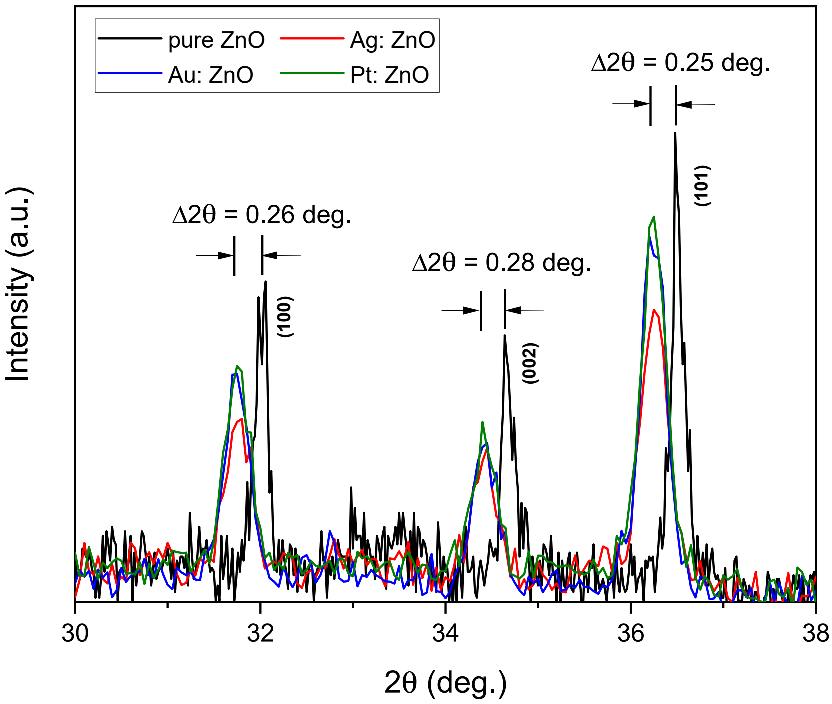

Figure 5. The Ag, Au, and Pt doped ZnO peak shifts compared to the pure ZnO peaks.

Table 2. Comparison of the calculated lattice constants a and c with the respected c/a ratio.

	a (Å)	**c (Å)**	**c/a (Å)**
pure ZnO	3.226	5.170	1.603
Ag: ZnO	3.250	5.207	1.602
Au: ZnO	3.252	5.206	1.601
Pt: ZnO	3.251	5.207	1.603

The strain and average crystallite size can be determined from the Williamson-Hall (W-H) and strain-size (S-S) plots (Figure 6). The W-H plot (Figure 6a) uses the following relation:

$$(\beta cos\theta) = \frac{0.94\lambda}{D} + \varepsilon(4sin\theta) \tag{5}$$

where ε is a microstrain. Crystallite size and microstrain are obtained from the intersection and slope value, respectively. The S-S plot (Figure 6b) is based on the relation:

$$(d_{hkl}\beta_{hkl}cos\theta)^2 = \frac{0.94\lambda}{D}\left(d_{hkl}^2\beta_{hkl}cos\theta\right) + \frac{\varepsilon^2}{4} \tag{6}$$

where d_{hkl} is interplanar spacing. Crystallite size and strain are obtained from the slope and intersection, respectively.

Table 3. Comparison of the obtained crystallite sizes (D) using the Debye–Scherer formula (D-S), Williamson-Hall (W-H), and size-strain (S-S) plots. Corresponding dislocation densities (δ) and strains (ε) are presented.

	$D_{D\text{-}S}$ (nm)	$D_{W\text{-}H}$ (nm)	$D_{S\text{-}S}$ (nm)	$\delta_{(D\text{-}S)} \times 10^{-3}$ (nm^{-2})	$\delta_{(W\text{-}H)} \times 10^{-4}$ (nm^{-2})	$\delta_{(S\text{-}S)} \times 10^{-4}$ (nm^{-2})	$\varepsilon_{(W\text{-}H)} \times 10^{-4}$	$\varepsilon_{(S\text{-}S)} \times 10^{-4}$
ZnO	50	44 ± 8	35 ± 6	0.04	0.05	0.08	1.4 ± 0.4	1.1 ± 0.7
Ag: ZnO	24	24 ± 5	25 ± 4	0.17	0.17	0.16	2.1 ± 0.1	0.2 ± 0.1
Au: ZnO	25	30 ± 7	24 ± 5	0.16	0.11	0.17	5.2 ± 2.3	0.8 ± 0.2
Pt: ZnO	24	39 ± 7	21 ± 6	0.17	0.06	0.23	1.5 ± 0.3	1.3 ± 0.4

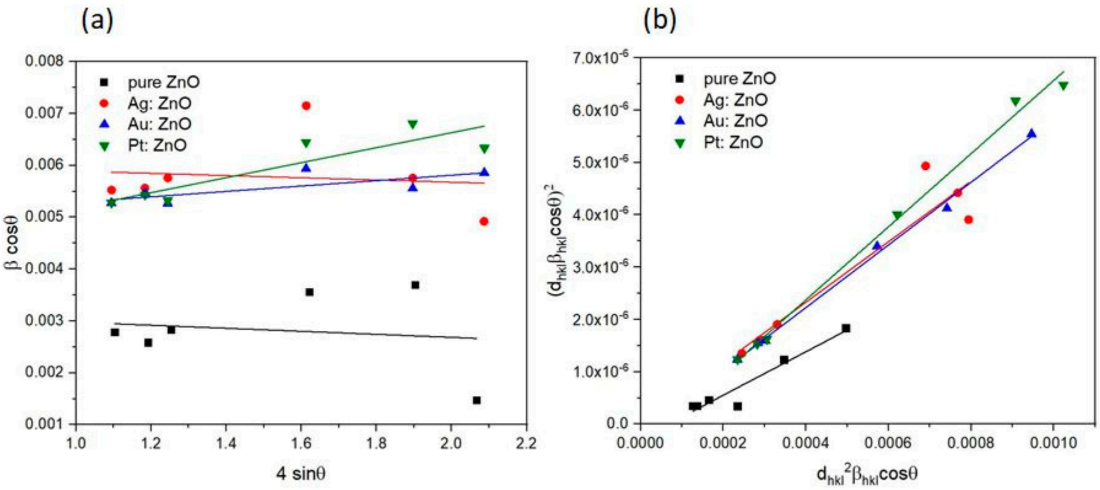

Figure 6. (**a**) Williamson-Hall and (**b**) size-strain analysis of pure and doped ZnO NPs. Using linear fit to the data, the crystallite size and strain are extracted and presented in Table 3.

Table 3 presents the values of the crystallite size, strain, and dislocation density. Dislocation density is obtained using the following formulae [52]:

$$\delta = \frac{1}{D^2} \tag{7}$$

From Table 3, it is apparent that the Ag:ZnO and Au:ZnO crystallite sizes obtained from three different methods are approximately the same, while for pure ZnO, a value between 35 and 50 nm is obtained. With Pt:ZnO, a larger crystallite size is obtained using the W-H method, which can give a larger number of crystallites because the broadening of the peak due to microstrains and crystallites is taken into account. Doped nanoparticles have a higher dislocation density than pure ZnO, which means that lattice defects occur and atoms in crystal cells are displaced from an ideal position due to the smaller crystallite size. The strains obtained for pure ZnO and Pt:ZnO are approximately the same, while for Ag:ZnO and Au:ZnO, there are deviations between the values.

3.4. Chemical Composition Analysis

To obtain further insight into the chemical composition and formation of doped ZnO nanoparticles, XPS analysis was applied to analyze the surface composition of such nanoparticles.

In Figure 7, wide XPS spectra are shown for ZnO nanoparticles doped with Ag, Au, and Pt. The presence of characteristic peaks can be identified for zinc (Zn 2p, Zn 3s, Zn 3p, Zn 3d, and Auger peaks Zn LMM), oxygen (O 1s and Auger peak O KLL), and carbon (C 1s). Peaks for Ag 3d, Au 4f, and Pt 4f can also be identified. Wide XPS spectra indicate that ZnO nanoparticles are doped and hence successfully synthesized.

The XPS high-resolution spectra are shown in Figure 8. Deconvolution of the Zn $2p_{3/2}$ peak (Figure 8a) reveals a gaussian distribution with a maximum at 1021.5 eV which corresponds to Zn^{2+} states in the ZnO crystal lattice [57]. Deconvolution of the O 1s (Figure 8b) peak results in two gaussian fits, first with a maximum at 529.6 eV and the second with a maximum at 531.4 eV. The first peak is related to a O^{2-} state that is built up in the ZnO crystal lattice, and the second peak is related to hydroxyl radical (O-H) [58]. Deconvolution of C 1s states (Figure 8c) results in two gaussian fits with maxima at 289.1 eV and 284.8 eV, related to C=O bonds and to C-C bonds, respectively [59]. Carbon occurs as a sample impurity, as samples were exposed to the atmosphere (C-H) after drying and before any analysis. The deconvolution of Ag 3d states (Figure 8d) resulted in two peaks at 373.5 eV and 367.4 eV related to $3d_{3/2}$ and $3d_{5/2}$ states, respectively. Those peaks are related to Ag-O bonding, as the same binding energies are characteristic for Ag_2O [60]. The absence of a pure metallic Ag state expected at 368.3 eV (marked in spectrum) implies that all silver is incorporated in the ZnO lattice rather than in a separate nanoparticle form. The deconvolution of the Au 4f state (Figure 8e) resulted in two overlapping peaks at 91.8 eV (related to the Zn $3p_{1/2}$ state) and at 85.8 eV (related to the Au $4f_{5/2}$ state). The absence of the Au $4f_{7/2}$ state at 84 eV (marked in spectrum) implies that there is no Au in the metallic state and hence that Au is incorporated into the ZnO lattice rather than being attached to the ZnO NP surface as a pure nanoparticle [61–63]. The deconvolution of Pt 4f states (Figure 8f) resulted in two peaks at 76.1 eV and 72.9 eV, related to $4f_{5/2}$ and $4f_{7/2}$ states, respectively. Those states are related to metallic Pt, but they also exhibit a shift of 1.9 eV towards higher binding energies than that of pure metallic Pt [64]. This may be an indication that a Pt-Zn alloy is formed [65] beside the Pt incorporation into the ZnO lattice, as was revealed with XRD. It is known that Zn and Pt can be mixed together in a variety of different alloy compositions [66].

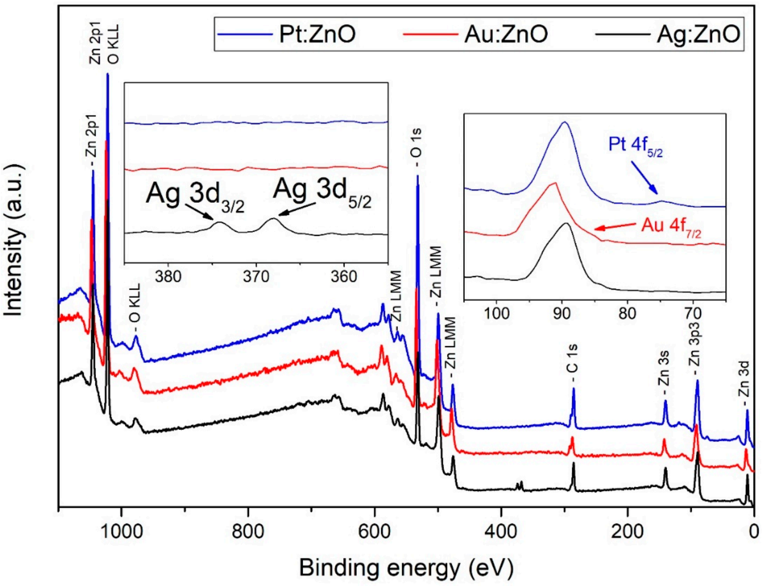

Figure 7. Wide XPS spectra of ZnO nanoparticles doped with Ag (black), Au (red), and Pt (blue). In insets: identification of Ag, Au, and Pt.

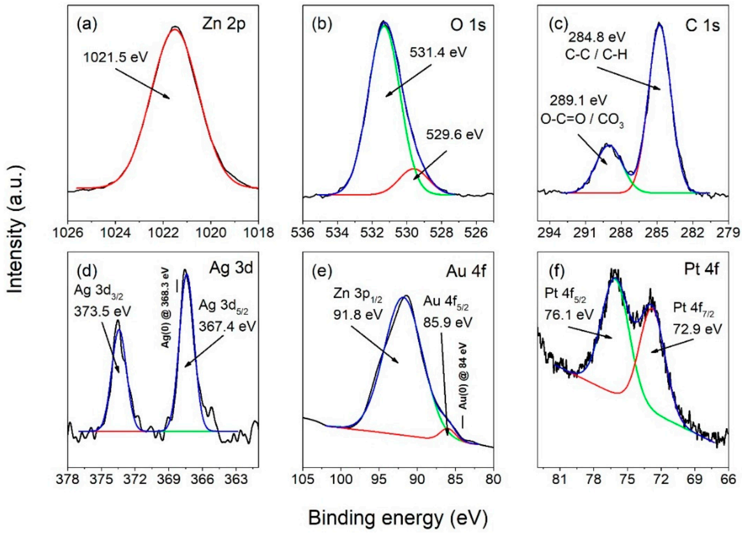

Figure 8. High resolution XPS spectra of doped ZnO nanoparticles with fitted spectra for (**a**) Zn 2p, (**b**) O 1s, (**c**) C 1s, (**d**) Ag 3d, (**e**) Au 4f, and (**f**) Pt 4f. Red and green curves represent fit peaks while blue curve represents cumulative fit peak.

3.5. Morphological Analysis

Morphological analysis (using TEM and SEM) of the samples revealed obtained nanoparticles and their size range. In Figure 9, TEM images for pure (a, b) and Pt-doped (c, d) ZnO NP are presented. The morphology of the nanoparticles is independent of the dopant material; therefore, we revealed TEM images of ZnO doped with gold (Figure 9c,d), which also describe the morphology of ZnO NPs doped with Ag and Pt. Figure 9a,c shows different-sized spherical nanoparticles and irregular material, which are formed during the laser ablation process. The surface morphology of the obtained NPs is shown in Figure 9b,d. The surface is relatively smooth with some roughness because the edges are not perfectly sharp. Figure 10 shows the SEM images of Ag-, Au-, and Pt-doped ZnO structures with their respective size distributions. Spherical nanoparticles from 50 nm up to 200 nm dominate in each sample. During the ablation process, some micro-sized particles and debris formed. Also, amorphous parts occurred, which agrees with the relatively broad XRD patterns. From SEM images, we determined the size distribution of nanoparticles. Size distribution is fitted as a log-normal function with maxima at diameters 51 nm, 71 nm, 73 nm, and 89 nm for the pure ZnO, Ag: ZnO, Au: ZnO, and Pt: ZnO, respectively. Pt-doped ZnO nanoparticles are slightly larger compared to the Ag- and Au-doped ZnO nanoparticles, while all doped ZnO NPs are larger than pure ZnO.

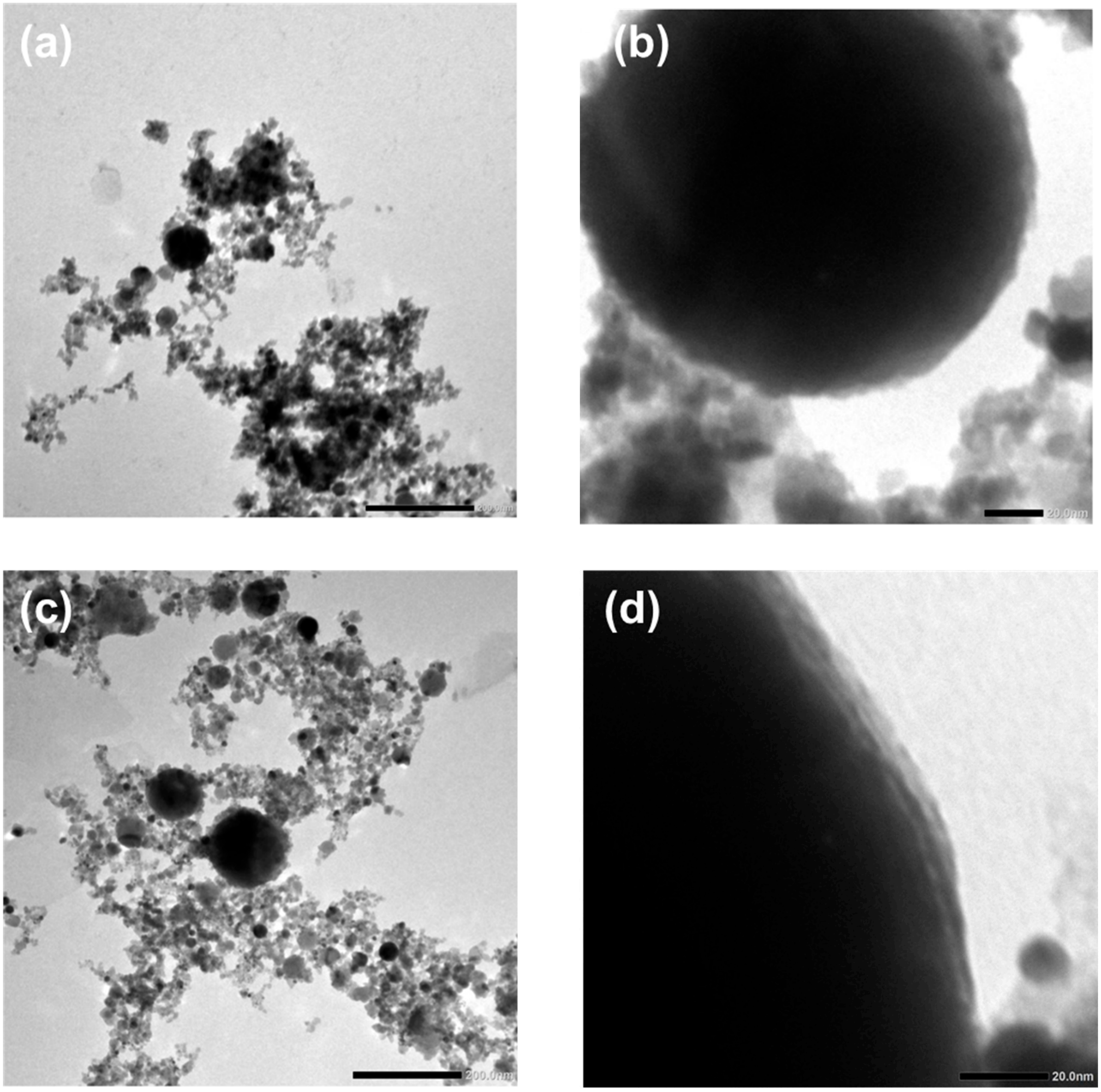

Figure 9. TEM images of (**a**,**b**) pure and (**c**,**d**) Pt-doped ZnO nanoparticles.

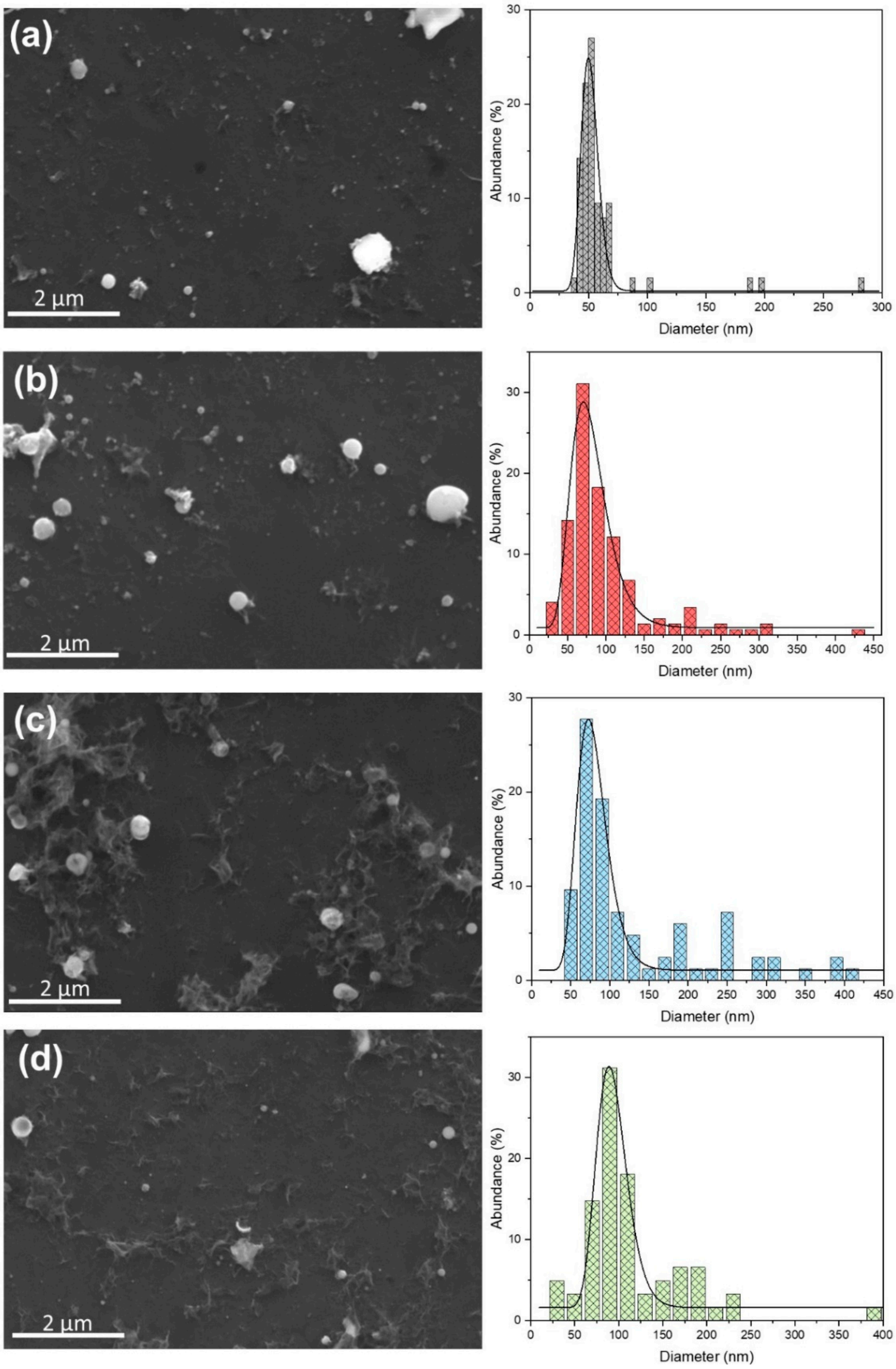

Figure 10. SEM images and size-distributions of (**a**) pure ZnO, (**b**) Ag-doped ZnO, (**c**) Au-doped ZnO, and (**d**) Pt-doped ZnO.

4. Conclusions

We demonstrated a novel two-step process using PLD and PLAL techniques for the production of Ag, Au, and Pt-doped ZnO NPs. The band-gap energies, calculated from the UV-Vis spectra, are 3.2 eV, 3.15 eV, 3.08 eV, and 3.06 eV for pure and silver, gold, and platinum-doped ZnO, respectively. The decrease in the band-gap energy implies changes in the nanocrystal electronic structure and more efficient light absorption. PL measurements showed that doped ZnO NPs have a lower recombination rate of the excitons compared to pure ZnO. Doped ZnO has no emission in the visible region compared to pure ZnO, implying low defect concentration. The XRD patterns showed that Ag-, Au-, and Pt-doped ZnO NPs maintained a hexagonal wurtzite structure without any Ag, Au, and Pt peaks. This, together with the fact that peaks are shifting towards smaller Bragg's angles, confirms that Ag, Au, and Pt are well incorporated inside the ZnO lattice. It is also confirmed with the XPS study (to some minor extent only Pt appears in metallic form). Synthesized doped ZnO NPs are spherical-shaped with smooth surfaces, while morphology is independent of the dopant material. This study could provide a new way for the quick and clean synthesis of various doped materials.

5. Patents

Krstulović, N.; Blažeka, D.; Car, J.; Maletić, D.; Rakić, M. Method of Production of Two-Component Nanoparticles Using Laser. Croatian Patent P20211098A, 9 July 2021.

Author Contributions: R.R.: synthesis of nanoparticles, analysis and discussion of results, and writing of manuscript; D.M.: synthesis of nanoparticles, analysis of results; D.B.: synthesis of nanoparticles; J.C.: analysis and discussion of results; N.K.: analysis and discussion of results, writing of manuscript, conceptual design of experiment, and project management. All authors have read and agreed to the published version of the manuscript.

Funding: This research was supported by the Croatian Science Foundation under the project PZS-2019-02-5276.

Institutional Review Board Statement: Not applicable.

Informed Consent Statement: Not applicable.

Data Availability Statement: Data available on request.

Acknowledgments: This work was supported by the Croatian Science Foundation under project HrZZ-PZS-2019-02-5276. D.M. is grateful to the Institute of Physics Belgrade, Ministry of Education, Science and Technological Development, Republic of Serbia, and The Centre of Excellence Non-Equilibrium Processes, IPB.

Conflicts of Interest: The authors declare no conflict of interest.

References

1. Huang, C.; Chen, X.; Xue, Z.; Wang, T. Effect of structure: A new insight into nanoparticle assemblies from inanimate to animate. *Sci. Adv.* **2020**, *6*, eaba1321. [CrossRef] [PubMed]
2. Fei Guo, C.; Sun, T.; Cao, F.; Liu, Q.; Ren, Z. Metallic nanostructures for light trapping in energy-harvesting devices. *Light Sci Appl.* **2014**, *3*, e161. [CrossRef]
3. Chowdhury, N.K.; Bhowmik, B. Micro/nanostructured gas sensors: The physics behind the nanostructure growth, sensing and selectivity mechanisms. *Nanoscale Adv.* **2021**, *3*, 73–93. [CrossRef]
4. Han, J.; Freyman, M.C.; Feigenbaum, E.; Yong-Jin Han, T. Electro-Optical Device with Tunable Transparency Using Colloidal Core/Shell Nanoparticles. *ACS Photonics* **2018**, *5*, 1343–1350. [CrossRef]
5. Blažeka, D.; Car, J.; Klobučar, N.; Jurov, A.; Zavašnik, J.; Jagodar, A.; Kovačević, E.; Krstulović, N. Photodegradation of Methylene Blue and Rhodamine B Using Laser-Synthesized ZnO Nanoparticles. *Materials* **2020**, *13*, 4357. [CrossRef]
6. Salvioni, L.; Morelli, L.; Ochoa, E.; Labra, M.; Fiandra, L.; Palugan, L.; Prosperi, D.; Colombo, M. The emerging role of nanotechnology in skincare. *Adv. Colloid Interface Sci.* **2021**, *293*, 102437. [CrossRef] [PubMed]
7. Patra, J.K.; Das, G.; Fraceto, L.F.; Campos, E.V.R.; Rodriguez-Torres, M.P.; Acosta-Torres, L.S.; Diaz-Torres, L.A.; Grillo, R.; Swamy, M.K.; Sharma, S.; et al. Nano based drug delivery systems: Recent developments and future prospects. *J. Nanobiotechnol.* **2018**, *16*, 71. [CrossRef]
8. Rastogi, A.; Zivcak, M.; Sytar, O.; Kalaji, H.M.; He, X.; Mbarki, S.; Brestic, M. Impact of Metal and Metal Oxide Nanoparticles on Plant: A Critical Review. *Front. Chem.* **2017**, *5*, 78. [CrossRef]
9. Naseem, T.; Durrani, T. The role of some important metal oxide nanoparticles for wastewater and antibacterial applications: A review. *Environ. Toxicol. Chem.* **2021**, *3*, 59–75. [CrossRef]
10. Zhang, J.; Chaker, M.; Ma, D. Pulsed Laser Ablation based Synthesis of Colloidal Metal Nanoparticles for Catalytic Applications. *J. Coll. Interface Sci.* **2017**, *489*, 138–149. [CrossRef]

11. Tymoczko, A.; Kamp, M.; Rehbock, C.; Kienle, L.; Cattaruzza, E.; Barcikowski, S.; Amendola, V. One-step synthesis of Fe–Au core–shell magnetic-plasmonic nanoparticles driven by interface energy minimization. *Nanoscale Horiz.* **2019**, *4*, 1326–1332. [CrossRef]
12. Oko, D.N.; Zhang, J.; Garbarino, S.; Chaker, M.; Ma, D.; Tavares, A.C.; Guay, D. Formic acid electro-oxidation at PtAu alloyed nanoparticles synthesized by pulsed laser ablation in liquids. *J. Power Sources* **2014**, *248*, 273–282. [CrossRef]
13. Marzun, G.; Streich, C.; Jendrzej, S.; Barcikowski, S.; Wagener, P. Adsorption of colloidal platinum nanoparticles to supports: Charge transfer and effects of electrostatic and steric interactions. *Langmuir* **2014**, *30*, 11928–11936. [CrossRef]
14. Zhang, J.; Chen, G.; Chaker, M.; Rosei, F.; Ma, D. Gold nanoparticle decorated ceria nanotubes with significantly high catalytic activity for the reduction of nitrophenol and mechanism study. *Appl. Catal. B Environ.* **2013**, *132–133*, 107–115. [CrossRef]
15. Galstyan, V.; Comini, E.; Baratto, C.; Faglia, G.; Sberveglieri, G. Nanostructured ZnO chemical gas sensors. *Ceram. Int.* **2015**, *41*, 14239–14244. [CrossRef]
16. Özgür, Ü.; Hofstetter, D.; Morkoç, H. ZnO Devices and Applications: A Review of Current Status and Future Prospects. *Proc. IEEE* **2010**, *98*, 1255–1268. [CrossRef]
17. Wibowo, A.; Marsudi, M.A.; Amal, M.I.; Ananda, M.B.; Stephanie, R.; Ardy, H.; Diguna, L.J. ZnO nanostructured materials for emerging solar cell applications. *RSC Adv.* **2020**, *10*, 42838–42859. [CrossRef] [PubMed]
18. Marković, M.K.; Peter, R.; Badovinac, I.J.; Šarić, I.; Perčić, M.; Radičić, R.; Marković, D.; Knez, M.; Ambrožić, G. 'Sandwich'-like hybrid ZnO thin films produced by a combination of atomic layer deposition and wet-chemistry using a mercapto silane as single organic precursor. *Nanotechnology* **2020**, *31*, 185603. [CrossRef]
19. Sirelkhatim, A.; Mahmud, S.; Seeni, A.; Kaus, N.H.M.; Ann, L.C.; Bakhori, S.K.M.; Hasan, H.; Mohamad, D. Review on Zinc Oxide Nanoparticles: Antibacterial Activity and Toxicity Mechanism. *Nano-Micro Lett.* **2015**, *7*, 219–242. [CrossRef] [PubMed]
20. Espitia, P.J.P.; Soares, N.F.F.; Coimbra, J.S.R.; Andrade, N.J.; Cruz, R.S.; Medeiros, E.A.A. Zinc Oxide Nanoparticles: Synthesis, Antimicrobial Activity and Food Packaging Applications. *Food Bioprocess Technol.* **2012**, *5*, 1447–1464. [CrossRef]
21. Rasmussen, J.W.; Martinez, E.; Louka, P.; Wingett, D.G. Zinc Oxide Nanoparticles for Selective Destruction of Tumor Cells and Potential for Drug Delivery Applications. *Expert Opin. Drug Deliv.* **2010**, *7*, 1063–1077. [CrossRef] [PubMed]
22. Bhatia, D.; Sharma, H.; Meena, R.S.; Palkar, V.R. A Novel ZnO Piezoelectric Microcantilever Energy Scavenger: Fabrication and Characterization. *Sens. Bio-Sens. Res.* **2016**, *9*, 45–52. [CrossRef]
23. Wang, Z.; Yu, R.; Pan, C.; Li, Z.; Yang, J.; Yi, F.; Wang, Z.L. Light-Induced Pyroelectric Effect as an Effective Approach for Ultrafast Ultraviolet Nanosensing. *Nat. Commun.* **2015**, *6*, 8401. [CrossRef] [PubMed]
24. Chi, D.; Huang, S.; Yue, S.; Liu, K.; Lu, S.; Wang, Z.; Qu, S.; Wang, Z. Ultra-Thin ZnO Film as an Electron Transport Layer for Realizing the High Efficiency of Organic Solar Cells. *RSC Adv.* **2017**, *7*, 14694–14700. [CrossRef]
25. Ahmad, M.; Ahmed, E.; Hong, Z.L.; Ahmed, W.; Elhissi, A.; Khalid, N.R. Photocatalytic, Sonocatalytic and Sonophotocatalytic Degradation of Rhodamine B Using ZnO/CNTs Composites Photocatalysts. *Ultrason. Sonochem.* **2014**, *21*, 761–773. [CrossRef] [PubMed]
26. Carofiglio, M.; Barui, S.; Cauda, V.; Laurenti, M. Doped Zinc Oxide Nanoparticles: Synthesis, Characterization and Potential Use in Nanomedicine. *Appl. Sci.* **2020**, *10*, 5194. [CrossRef] [PubMed]
27. Özgür, Ü.; Alivov, Y.I.; Liu, C.; Teke, A.; Reshchikov, M.A.; Doğan, S.; Avrutin, V.; Cho, S.-J.; Morkoç, H. A Comprehensive Review of ZnO Materials and Devices. *J. Appl. Phys.* **2005**, *98*, 041301. [CrossRef]
28. Zhao, D.; Li, J.; Sathasivam, S.; Carmalt, C.J. N-Type Conducting P Doped ZnO Thin Films via Chemical Vapor Deposition. *RSC Adv.* **2020**, *10*, 34527–34533. [CrossRef]
29. Munawaroh, H.; Wahyuningsih, S.; Ramelan, A.H. Synthesis and Characterization of Al doped ZnO (AZO) by Sol-gel Method. *IOP Conf. Ser. Mater. Sci. Eng.* **2017**, *176*, 012049. [CrossRef]
30. Lee, D.-J.; Kim, K.-J.; Kim, S.-H.; Kwon, J.-Y.; Xu, J.; Kim, K.-B. Atomic Layer Deposition of Ti-Doped ZnO Films with Enhanced Electron Mobility. *J. Mater. Chem. C* **2013**, *1*, 4761. [CrossRef]
31. Kaur, G.; Mitra, A.; Yadav, K.L. Pulsed laser deposited Al-doped ZnO thin films for optical applications. *Prog. Nat. Sci.* **2015**, *25*, 12–21. [CrossRef]
32. Rana, A.K.; Bankar, P.; Kumar, Y.; More, M.A.; Late, D.J.; Shirage, P.M. Synthesis of Ni-Doped ZnO Nanostructures by Low-Temperature Wet Chemical Method and Their Enhanced Field Emission Properties. *RSC Adv.* **2016**, *6*, 104318–104324. [CrossRef]
33. Streubel, R.; Barcikowski, S.; Gökce, B. Continuous Multigram Nanoparticle Synthesis by High-Power, High-Repetition-Rate Ultrafast Laser Ablation in Liquids. *Opt. Lett.* **2016**, *41*, 1486. [CrossRef] [PubMed]
34. Fazio, E.; Gökce, B.; De Giacomo, A.; Meneghetti, M.; Compagnini, G.; Tommasini, M.; Waag, F.; Lucotti, A.; Zanchi, C.G.; Ossi, P.M.; et al. Nanoparticles Engineering by Pulsed Laser Ablation in Liquids: Concepts and Applications. *Nanomaterials* **2020**, *10*, 2317. [CrossRef] [PubMed]
35. Sahoo, A.; Miryala, M.; Dixit, T.; Klimkowicz, A.; Francis, B.; Murakami, M.; Rao, M.S.R.; Krishnan, S. Femtosecond Pulse Ablation Assisted Mg-ZnO Nanoparticles for UV-Only Emission. *Nanomaterials* **2020**, *10*, 1326. [CrossRef] [PubMed]
36. Chelnokov, E.; Rivoal, M.; Colignon, Y.; Gachet, D.; Bekere, L.; Thibaudau, F.; Giorgio, S.; Khodorkovsky, V.; Marine, W. Band Gap Tuning of ZnO Nanoparticles via Mg Doping by Femtosecond Laser Ablation in Liquid Environment. *Appl. Surf. Sci.* **2012**, *23*, 9408–9411. [CrossRef]
37. Qin, W.J.; Sun, J.; Yang, J.; Du, X.W. Control of Cu-doping and optical properties of ZnO quantum dots by laser ablation of composite targets. *Mater. Chem. Phys.* **2011**, *130*, 425–430. [CrossRef]

38. Yudasari, N.; Suliyanti, M.M.; Imawan, C. Antibacterial Activity of Fe-Doped ZnO Nanoparticles Synthesised via Pulsed Laser Ablation in Liquid against *Staphylococcus Aureus*. *Adv. Nat. Sci. Nanosci. Nanotechnol.* **2020**, *11*, 025003. [CrossRef]
39. Anugrahwidya, R.; Yudasari, N.; Tahir, D. Optical and Structural Investigation of Synthesis ZnO/Ag Nanoparticles Prepared by Laser Ablation in Liquid. *Mater. Sci. Semicond. Process.* **2020**, *105*, 104712. [CrossRef]
40. Khashan, K.S.; Mahdi, M. Preparation of Indium-Doped Zinc Oxide Nanoparticles by Pulsed Laser Ablation in Liquid Technique and Their Characterization. *Appl. Nanosci.* **2017**, *7*, 589–596. [CrossRef]
41. Krstulović, N.; Umek, P.; Salamon, K.; Capan, I. Synthesis of Al-Doped ZnO Nanoparticles by Laser Ablation of ZnO:Al_2O_3 Target in Water. *Mater. Res. Express* **2017**, *4*, 105003. [CrossRef]
42. Krstulović, N.; Blažeka, D.; Car, J.; Maletić, D.; Rakić, M. Method of Production of Two-Component Nanoparticles Using Laser. Croatian Patent P20211098A, 9 July 2021.
43. Moulder, J.F.; Stickle, W.F.; Sobol, P.E.; Bomben, K.D. *Handbook of X-ray Photoelectron Spectroscopy: A Reference Book of Standard Spectra for Identification and Interpretation of XPS Data*; Chastain, J., Ed.; Physical Electronics Inc.: Eden Prairie, MN, USA, 1995.
44. Mintcheva, N.; Aljulaih, A.A.; Wunderlich, W.; Kulinich, S.A.; Iwamori, S. Laser-Ablated ZnO Nanoparticles and Their Photocatalytic Activity Toward Organic Pollutants. *Materials* **2018**, *11*, 1127. [CrossRef]
45. Kamarulzaman, N.; Kasim, M.F.; Rusdi, R. Band Gap Narrowing and Widening of ZnO Nanostructures and Doped Materials. *Nanoscale Res. Lett.* **2015**, *10*, 346. [CrossRef] [PubMed]
46. Reddy, A.J.; Kokila, M.K.; Nagabhushana, H.; Rao, J.L.; Shivakumara, C.; Nagabhushana, B.M.; Chakradhar, R.P.S. Combustion Synthesis, Characterization and Raman Studies of ZnO Nanopowders. *Spectrochim. Acta A Mol. Biomol. Spectrosc.* **2011**, *81*, 53–58. [CrossRef]
47. Li, W.; Wang, G.; Chen, C.; Liao, J.; Li, Z. Enhanced Visible Light Photocatalytic Activity of ZnO Nanowires Doped with Mn^{2+} and Co^{2+} Ions. *Nanomaterials* **2017**, *7*, 20. [CrossRef] [PubMed]
48. Shah, A.; Ahmad, M.; Rahmanuddin Khan, S.; Aziz, U.; Ali, Z.; Khan, A.; Mahmood, A. The Role of Al Doping on ZnO Nanowire Evolution and Optical Band Gap Tuning. *Appl. Phys. A* **2019**, *125*, 713. [CrossRef]
49. Khokhra, R.; Bharti, B.; Lee, H.-N.; Kumar, R. Visible and UV Photo-Detection in ZnO Nanostructured Thin Films via Simple Tuning of Solution Method. *Sci. Rep.* **2017**, *7*, 15032. [CrossRef] [PubMed]
50. Mhlongo, G.H.; Shingange, K.; Tshabalala, Z.P.; Dhonge, B.P.; Mahmoud, F.A.; Mwakikunga, B.W.; Motaung, D.E. Room temperature ferromagnetism and gas sensing in ZnOnanostructures: Influence of intrinsic defects and Mn, Co, Cu doping. *Appl. Surf. Sci.* **2016**, *390*, 804–815. [CrossRef]
51. Ahmad, I.; Shoaib Akhtar, M.; Ahmed, E.; Ahmad, M.; Keller, V.; Qamar Khan, W.; Khalid, N.R. Rare Earth Co-Doped ZnO Photocatalysts: Solution Combustion Synthesis and Environmental Applications. *Sep. Purif. Technol.* **2020**, *237*, 116328. [CrossRef]
52. Panigrahy, B.; Aslam, M.; Misra, D.S.; Ghosh, M.; Bahadur, D. Defect-Related Emissions and Magnetization Properties of ZnO Nanorods. *Adv. Funct. Mater.* **2010**, *20*, 1161–1165. [CrossRef]
53. Blažeka, D.; Radičić, R.; Maletić, D.; Živković, S.; Momčilović, M.; Krstulović, N. Enhancement of Methylene Blue Photodegradation Rate Using Laser Synthesized Ag-Doped ZnO Nanoparticles. *Nanomaterials* **2022**, *12*, 2677. [CrossRef]
54. Singh, A.; Vishwakarma, H.L. Study of structural, morphological, optical and electroluminescent properties of undoped ZnO nanorods grown by a simple chemical precipitation. *Mater. Sci.-Pol.* **2015**, *33*, 751–759. [CrossRef]
55. Ekambaram, S.; Iikubo, Y.; Kudo, A. Combustion Synthesis and Photocatalytic Properties of Transition Metal-Incorporated ZnO. *J. Alloy Compd.* **2007**, *433*, 237–240. [CrossRef]
56. Edinger, S.; Bansal, N.; Bauch, M.; Wibowo, R.A.; Újvári, G.; Hamid, R.; Trimmel, G.; Dimopoulos, T. Highly Transparent and Conductive Indium-Doped Zinc Oxide Films Deposited at Low Substrate Temperature by Spray Pyrolysis from Water-Based Solutions. *J. Mater. Sci.* **2017**, *52*, 8591–8602. [CrossRef]
57. Narath, S.; Koroth, S.K.; Shankar, S.S.; George, B.; Mutta, V.; Wacławek, S.; Černík, M.; Padil, V.V.T.; Varma, R.S. Tamala, Cinnamomum Leaf Extract Stabilized Zinc Oxide Nanoparticles: A Promising Photocatalyst for Methylene Blue Degradation. *Nanomaterials* **2021**, *11*, 1558. [CrossRef]
58. Gruzintsev, A.N.; Volkov, V.T.; Yakimov, E.E. Photoelectric properties of ZnO films doped with Cu and Ag acceptor impurities. *Semiconductors* **2003**, *37*, 259–262. [CrossRef]
59. Rakkesh, R.A.; Durgalakshmi, D.; Balakumar, S. Beyond Chemical Bonding Interaction: An Insight into the Growth Process of 1D ZnO on Few-Layer Graphene for Excellent Photocatalytic and Room Temperature Gas Sensing Applications. *Chem. Sel.* **2018**, *3*, 7302–7309. [CrossRef]
60. Tjeng, L.H.; Meinders, M.B.J.; van Elp, J.; Ghijsen, J.; Sawatzky, G.A.; Johnson, R.L. Electronic structure of Ag_2O. *Phys. Rev. B* **1990**, *41*, 3190. [CrossRef]
61. Vitale, F.; Fratoddi, I.; Battocchio, C.; Piscopiello, E.; Tapfer, L.; Russo, M.V.; Polzonetti, G.; Giannini, C. Mono- and bi-functional arenethiols as surfactants for gold nanoparticles: Synthesis and characterization. *Nanoscale Res. Lett.* **2011**, *6*, 103. [CrossRef] [PubMed]
62. Gogurla, N.; Kumar Sinha, A.; Santra, S.; Manna, S.; Kumar Ray, S. Multifunctional Au-ZnO Plasmonic Nanostructures for Enhanced UV Photodetector and Room Temperature NO Sensing Devices. *Sci. Rep.* **2014**, *4*, 6483. [CrossRef] [PubMed]
63. Sahoo, S.R.; Ke, S.-C. Spin-Orbit Coupling Effects in Au 4f Core-Level Electronic Structures in Supported Low-Dimensional Gold Nanoparticles. *Nanomaterials* **2021**, *11*, 554. [CrossRef] [PubMed]

64. Xia, Y.; Le, T.; Peng, J.; Ravindra, A.V.; Xu, L. Pt quantum dots decorated nest-like 3D porous ZnO nanostructures for enhanced visible-light degradation of RhB. *J. Porous Mater.* **2020**, *27*, 1339–1348. [CrossRef]
65. Naitabdi, A.; Boucly, A.; Rochet, F.; Fagiewicz, R.; Olivieri, G.; Bournel, F.; Benbalagh, R.; Sirotti, F.; Galleta, J.-J. CO oxidation activity of Pt, Zn and ZnPt nanocatalysts: A comparative study by in situ near-ambient pressure X-ray photoelectron spectroscopy. *Nanoscale* **2018**, *10*, 6566. [CrossRef] [PubMed]
66. Massalski, T.B. *Binary Alloy Phase Diagrams*; ASM International: Materials Park, OH, USA, 1990. [CrossRef]

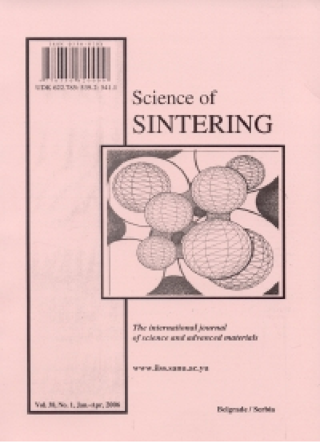

Science of Sintering 2025 OnLine-First Issue 00, Pages: 25-25
https://doi.org/10.2298/SOS250129025C
Full text (632 KB)

Plasma, UV radiation and ozone for microplastics degradation: Optical characterization of polystyrene, polyethylene and polypropylene degradation using FTIR and Raman spectroscopy

Ćurčić Milica *(Institute of Physics, University of Belgrade, Belgrade, Serbia), milicap@ipb.ac.rs*
Kolarž Predrag *(Institute of Physics, University of Belgrade, Belgrade, Serbia)*
Hadžić Branka *(Institute of Physics, University of Belgrade, Belgrade, Serbia)*
Stajčić Ivana *(Institute Vinca, University of Belgrade, Belgrade, Serbia)*
Lazarević Zorica *(Institute of Physics, University of Belgrade, Belgrade, Serbia)*
Maletić Dejan *(Institute of Physics, University of Belgrade, Belgrade, Serbia)*
Aničić Urošević Mira *(Institute of Physics, University of Belgrade, Belgrade, Serbia)*
Ilić Andjelija *(Institute of Physics, University of Belgrade, Belgrade, Serbia)*

This study investigated the changes in the optical properties of three types of microplastics-polypropylene (PP), polyethylene (PE), and polystyrene (PS)-when exposed to three different treatments: ozone, UV radiation, and plasma. Laboratory experiments were conducted to examine how each treatment affected the degradation of these polymers. The resulting changes in optical and structural characteristics were analyzed using FTIR and Raman spectroscopy. These techniques provided valuable insights into the behavior and persistence of microplastics under various treatments, revealing specific structural modifications at the molecular level.

Keywords: Microplastics, degradation, optical properties, Raman spectroscopy, FTIR spectroscopy

- Citation export
- Email this article

Submitted: 29.01.2025.

Accepted: 03.04.2025.

https://doi.org/10.2298/SOS250129025C

Plasma, UV Radiation and Ozone for Microplastics Degradation: Optical Characterization of Polystyrene, Polyethylene and Polypropylene Degradation using FTIR and Raman Spectroscopy

Milica Ćurčić[1*], Predrag Kolarž[1], Branka Hadžić[1], Ivana Stajčić[2], Zorica Lazarević[1], Dejan Maletić[1], Mira Aničić Urošević[1], Andjelija Ilić[1]

[1]Institute of Physics, University of Belgrade, Pregrevica 118, 11080 Belgrade, Serbia

[2]Institute Vinca, University of Belgrade, P.O. Box 522, 11001 Belgrade, Serbia

Abstract

This study investigated the changes in the optical properties of three types of microplastics—polypropylene (PP), polyethylene (PE), and polystyrene (PS)—when exposed to three different treatments: ozone, UV radiation, and plasma. Laboratory experiments were conducted to examine how each treatment affected the degradation of these polymers. The resulting changes in optical and structural characteristics were analyzed using FTIR and Raman spectroscopy. These techniques provided valuable insights into the behavior and persistence of microplastics under various treatments, revealing specific structural modifications at the molecular level.

Keywords: Microplastics, degradation, optical properties, Raman spectroscopy, FTIR spectroscopy

Degradacija mikroplastike plazmom, UV zračenjem i ozonom: optička karakterizacija degradacije polistirena, polietilena i polipropilena korišćenjem FTIR i Ramanove spektroskopije

Milica Ćurčić[1*], Predrag Kolarž[1], Branka Hadžić[1], Ivana Stajčić[2], Zorica Lazarević,[1] Dejan Maletić[1], Mira Aničić Urošević[1], Andjelija Ilić[1]

[1]Institute of Physics, University of Belgrade, Pregrevica 118, 11080 Belgrade, Serbia

[2]Institute Vinca, University of Belgrade, P.O. Box 522, 11001 Belgrade, Serbia

Abstract

Ova studija ispitivala je promene u optičkim svojstvima tri vrste mikroplastike—polipropilena (PP), polietilena (PE) i polistirena (PS)—kada su podvrgnuti različitim tretmanima: ozonu, UV zračenju i plazmi. Laboratorijski eksperimenti su sprovedeni kako bi se procenilo kako svaki od ovih tretmana utiče na degradaciju ovih polimera. Promene u optičkim i strukturnim svojstvima analizirane su korišćenjem FTIR-a i Raman spektroskopije. Ove metode su pružile dragocene uvide u ponašanje i postojanost mikroplastike pod različitim tretmanima, otkrivajući specifične strukturne modifikacije na molekularnom nivou.

Keywords: Mikroplastika, degradacija, optičke osobine, Ramanova spektroskopija, FTIR spektroskopija.

Plasma, UV Radiation and Ozone for Microplastics Degradation: Optical Characterization of Polystyrene, Polyethylene and Polypropylene Degradation using FTIR and Raman Spectroscopy

Milica Ćurčić[1*], Predrag Kolarž[1], Branka Hadžić[1], Ivana Stajčić[2], Zorica Lazarević,[1] Dejan Maletić[1], Mira Aničić Urošević[1], Andjelija Ilić[1]

[1]*Institute of Physics, University of Belgrade, Pregrevica 118, 11080 Belgrade, Serbia*

[2]*Institute Vinca, University of Belgrade, P.O. Box 522, 11001 Belgrade, Serbia*

*corresponding author:

1. Milica Ćurčić

Institute of Physics Belgrade, Pregrevica 118, Belgrade, Serbia

Phone: +381 11 3713 036

Email: milicap@ipb.ac.rs

1. Introduction

Plastics, particularly the types of plastics typically used in packaging, are materials known for their very long lifespans, despite often being produced for short-term use. Polystyrene (PS), polypropylene (PP) and polyethylene (PE) constitute the majority of single-use plastics, and their disposal can lead to environmental release, either directly through littering or indirectly due to the poor process controls [1, 2]. In 2016, it has been estimated that approximately 11% of the produced plastic waste ended up in aquatic environments [3]. Efforts are being made to reduce the amounts of plastic waste and to improve waste management, as well as to develop novel, biodegradable and chemically recyclable polymers [4-6]. However, many countries in the world lack the capacity to manage the plastic waste or produce advanced polymer materials [7]. Additionally, the projected overall increase in plastic production and the resulting environmental release indicate that merely improving waste management systems will not suffice to reduce pollution levels [3]. The existing environmental burden signifies an embedded toxicity debt, where the plastics already present will continue to impact the environment as they age, irrespective of future plastic inputs [8].

Microplastics, defined as particles larger than approximately 100 nm but smaller than 5 mm in diameter, have been detected worldwide. Recently, comprehensive data on their prevalence and distribution in natural environments have been increasingly reported in the scientific literature [1, 9-11]. The development of techniques for the intended degradation of microplastics is yet another topic of current interest [12-14]. However, in the field of monitoring microplastics, conventional sampling techniques for the detection and quantification of amounts of plastic particles are primarily adept at detecting microplastics and larger particles [6, 15]. As a result, there is a notable paucity of data on the environmental concentrations of nanoplastics, i.e., particles smaller than approximately 100 nm [16]. This data gap underscores the necessity to develop the advanced nanoplastics detection and quantification methods, to better handle the distinct and potentially significant environmental and health risks posed by their diminutive size. In light of these concerns, as well as the need for additional detailed studies of various degradation methods, we conducted experiments involving three types of microplastics—polystyrene, polyethylene, and polypropylene—subjecting them to extreme degradation conditions. Through separate exposures to plasma, UV radiation, and ozone, we aimed to break down the microplastics into smaller particles, potentially converting them into nanoplastics and further degrading them to a state where they are entirely destroyed. One of the main advantages of our approach is that it allows a comparison of the actual effects of various treatments; otherwise, with the combined treatments, the effects of each one might not be clearly discernable. The final objective of this study is to investigate whether these extreme degradation conditions can effectively reduce the size of microplastics and potentially significantly contribute to its elimination. The study results allow a better understanding of microplastics degradation processes and provide a pathway to assist in mitigating their environmental impact.

The degradation of polymers when exposed to the reactive gases including ozone has been studied in [17-19]. In [19], a study of the influence of destructive environmental factors on the transparency of polymer films, reflecting polymer structural changes, has been conducted using colorimetry and nuclear magnetic resonance relaxometry. The weathering of microplastics has also been shown to induce various polymer structural alterations, such as modifications to macromolecular groups, reduced molecular mass due to chain scission, changes in crystallinity content, and the formation of free radicals [20-22]. In general, UV irradiation can cause cracking, discoloration, and increased brittleness in polymers, primarily due to surface oxidation [23,24]. Additionally, by oxidizing polymer chains, UV irradiation can increase the material crystallinity, particularly in polystyrene (PS), making it more brittle and susceptible to mechanical abrasion [22]. Polyethylene (PE), one of the most popular and most widely used polymers in the world, can be extremely resistant to biodegradation due to its high molecular weight and its content of antioxidants and stabilizers [23]. Various methods, including the use of prooxidants and thermo- and photo-oxidation, have been devised to accelerate the PE degradation [23]. Although less frequently studied, thermal degradation has been observed to increase surface roughness and reduce tensile strength in thin films of high-density polyethylene (HDPE) exposed to near-boiling water temperatures (85–90°C) [25]. The combination of UV exposure and elevated temperatures can decrease the polymers resistance to thermal decomposition [26], and also, has been shown to sufficiently lower the molecular weight of HDPE to make it more prone to biodegradation [27]. These interactions highlight the complex nature of microplastic degradation and the importance of studying multiple degradation mechanisms simultaneously to fully understand their combined effects.

Plasma jet is rich in reactive oxygen and nitrogen species (RONS), including highly reactive species such as atomic oxygen (O), hydroxyl radicals (OH), excited oxygen molecules (O2-), nitric oxide (NO), and excited nitrogen molecules (N2+). Additionally, the plasma exhibited significant fluxes of ionized species, including N2+, O2+, and He+, which typically play a crucial role in surface chemistry modification. The plasma also emitted a broad spectrum of UV and visible radiation, which can contribute to photolytic processes of the microplastic surface. The plasma plume and the surface of the sample were maintained at a temperature close to the room temperature, thus minimizing thermal degradation of the microplastic sample. The interaction between the CAPJ and microplastic surfaces involved complex mechanisms driven by the diverse reactive species and energetic particles present in the plasma. The RONS, particularly OH radicals and atomic oxygen, are known for their high reactivity, leading to oxidative processes on the polymer surface. These processes can result in the cleavage of polymer chains, the formation of functional groups such as carbonyls, carboxyl's, and hydroxyls, and the overall increase in surface hydrophilicity. The ion bombardment, particularly from species such as N2+ and O2+, can induce localized physical etching, contributing to surface roughening and increase of the effective surface area. The UV and visible radiation emitted by the plasma also contribute to the degradation of microplastics. UV photons can break down chemical bonds in the polymer chains, initiating photodegradation pathways that work synergistically with the chemical effects induced by RONS and ions. This combined action of photolytic and oxidative mechanisms can lead to significant changes in the microplastic surface, including erosion, the formation of pits and cracks, and the reduction of polymer molecular weight.

Moreover, the near-room-temperature condition of the plasma plume is particularly advantageous for treating thermally sensitive materials. It allowed for the application of plasma treatment without inducing the thermal melting or significant thermal decomposition of microplastics, therefore ensuring that the observed effects are predominantly due to chemical interactions rather than the heat-induced processes.

Overall, the interaction between the CAPJ and the microplastic surfaces in this experiment highlights the potential of plasma technology for the degradation and transformation of polymeric materials. Since the cold plasma has been already recognized as a tool for the purification of wastewater [28, 29], its additional role as the environmental microplastics removal treatment could be implemented in a similar manner. The findings of this study provide insights into the mechanisms by which plasma treatment can be optimized for environmental applications, such as the breakdown of persistent microplastic pollutants.

We explored the alterations in optical properties for three types of microplastics—polypropylene (PP), polyethylene (PE), and polystyrene (PS). Laboratory experiments were designed to separately assess the impact of three distinct degradation treatments (ozone, UV radiation, plasma) on the breakdown mechanisms of each polymer. By analyzing the shifts in optical spectra, the research offers critical insights into the stability and degradation patterns of microplastics. The optical changes were identified through FTIR, Raman spectroscopy, and Field Emission Scanning Electron Microscopy (FESEM), which are among the most useful experimental analytical tools for microplastics characterization [2]. These techniques are capable of revealing molecular-level structural transformations, with FESEM providing detailed information on surface morphology and roughness, complementing the data obtained from FTIR and Raman spectroscopy. These spectroscopic techniques provided a comprehensive view of how each treatment uniquely affected the polymer structures.

2. Materials and methods

2.1. Preparation of samples and exposure to ozone and UV radiation

Plastic beads of three microplastic types—polypropylene (PP), polystyrene (PS), and polyethylene (PE), were used for the study. The plastic beads were manually cut into thin plastic sheets using clean stainless-steel scissors and then further trimmed into large microplastic fragments (<5 mm). All glassware was thoroughly cleaned by rinsing three times with deionized water followed by three rinses with acetone to ensure contamination-free conditions. The microplastics were subjected to the effects of UV radiation and ozone exposure. To better understand the degradation processes, the samples were individually exposed to UV light in a controlled chamber and to ozone for a specified duration. These treatments allowed for a comparative analysis of how each factor influenced the structural and chemical changes in the microplastics, providing insights into their respective impacts on weathering as well as intentionally planned degradation procedures. For the UV treatment, three samples (PS, PP and PE) were placed in a UV light chamber and exposed to germicide UV-C radiation (185 nm) using a Brenner UVP20001B bulb (power 150W) at a distance of 40 cm during one hour. For the ozone treatment, three samples were exposed to high ozone concentration of 30 ppm produced by OSS Thirty O^3 Ozone Generator, 30 000 mg/h for 45 minutes for each sample. Ozone concentration was measured by the Ozone meter AQ500 (Aqroqual).

2.2. Plasma treatment

Additionally, the interaction between a cold atmospheric plasma jet (CAPJ) and microplastic samples was investigated, focusing on the plasma-induced chemical and physical transformations at the microplastic surface. The jet was generated using a glass tube with an inner diameter (I.D.) of 1 mm and an outer diameter (O.D.) of 6 mm. Around the tube two copper foil electrodes were wrapped. These two electrodes, each 12 mm wide were spaced 12 mm apart, and were used to sustain the plasma discharge. Helium (He) was used as a working gas at a flow rate of 2 standard liters per minute (slm). The microplastic samples (PE, PP, PS) were positioned 10 mm below the plasma plume and exposed to plasma treatment for 45 min. The setup to produce the CAPJ is shown in Fig. 1. The plasma jet operated at 10 kV peak-to-peak voltage (Vpp), with a driving frequency of 80 kHz.

Figure 1. Setup used for plasma treatment.

The interaction between the CAPJ and microplastic surfaces involved complex mechanisms driven by the diverse reactive species and energetic particles present in the plasma.

3. Results and discussion

3.1. Field emission scanning electron microscopy (FESEM)

The structural analysis of microplastics with Fourier transform infrared spectroscopy (FTIR) was carried out on a Thermo Scientific Nicolet iS35 spectrometer manufactured in

Waltham, Massachusetts, United States. The analysis was conducted over a range spanning from 4000 to 400 cm^{-1}, employing a resolution of 4 cm^{-1}.

Surface roughness is a crucial parameter for evaluating the effects of surface treatment, as it can significantly influence various applications. Polystyrene (PS) was selected as a representative sample in this study due to its widespread commercial use, particularly in packaging, insulation, and disposable consumer goods. Understanding its degradation behavior is essential for addressing the environmental challenges posed by its persistence.

FESEM analysis was primarily focused on PS due to its well-defined structural changes upon degradation, making it a suitable model for evaluating surface morphology alterations. While similar degradation treatments were applied to polypropylene (PP) and polyethylene (PE), the structural contrast in their surface modifications was less pronounced under the imaging conditions used. Therefore, PS was chosen for detailed morphological analysis, as it exhibited the most significant changes, providing clearer insights into the effects of plasma treatment. Future studies will aim to optimize imaging conditions to enable a comprehensive morphological comparison of all three polymer types.

Figure 2 presents FESEM images of PS before and after degradation by plasma treatment. Compared to untreated PS (Figure 2a), the FESEM results clearly show that the surface roughness of PS increased significantly, and its structure underwent notable morphological changes after plasma treatment (Figure 2b). Among the tested treatments, plasma exposure resulted in the most pronounced degradation, as visible through the alterations in the surface morphology.

These findings highlight the aggressive nature of plasma in breaking down the polymer structure, leading to substantial roughening and surface irregularities. The analysis of these morphological changes underscores the potential of plasma treatment as an effective method for accelerating the degradation of PS, while also suggesting that combined approaches, such as UV and ozone, may offer a more balanced strategy for degrading microplastics while minimizing excessive surface roughening. These results provide critical insights into the degradation mechanisms of PS and its potential environmental impact.

Figure 2. FESEM images: a) PS before degradation and b) PS after degradation plasma.

3.2. FTIR spectroscopy

FTIR is one of the most commonly used methods for studying the degradation and stabilization of microplastics under various conditions because it offers some special attributes such as detection of orientation and stress, whereby it allows simultaneous measurements of degradation processes. FTIR spectra of PE, PP, and PS microplastics are presented in Fig. 3, Fig. 4, and Fig. 5. PE showed broad band at 3320.9 cm^{-1}, originating from absorbed moisture (Fig.3). Asymmetric and symmetric C-H stretch from -CH_2 appeared at 2912.7 cm^{-1} and 2845.3 cm^{-1}, respectively [31]. At 1472.0 cm^{-1} and 1461.5 cm^{-1} bending deformation was observed, while peak at 718.4 cm^{-1} belonged to -CH_2 rocking [30]. In PE/O_3 and PE/UV all of the peaks were retained with no appearance of new bonds, but with significantly higher peak intensities compared to the untreated PE, which is in accordance with the expectations.

Figure 3. FTIR spectra of PE and PE/Plasma, PE/O3, PE/UV.

Plasma is an efficient way to functionalize polymer surfaces as a result of the role of energetic species including charged particles, neutral radicals, excited species and UV radiation. The functionalization of plasma treated PE is achieved via free radical chains reactions, involving activation of the surface, formation of peroxides groups and generation of functionalized groups. However, in PE/PL spectrum, surface -OH groups were visible at 3340.3

cm^{-1}, generated from the local surface oxidation [31]. Furthermore, due to an air presence in the system, PE surface was modified with different functional groups, such as ester carbonyl group present at 1743.4 cm^{-1} formed by surface radicals' reaction with oxygen [32]. As a result of N_2 presence in air, at 1643.3 cm^{-1}, weak band from amide carbonyl group was also identified in the PE/Pl spectrum [33]. Bands at 1122.2 cm^{-1} and 1040.2 cm^{-1} originated from ether groups [34].

Polypropylene has a linear hydrocarbon structure composed only of carbon atoms in its main ring. PS has three stereochemical configurations: isotactic, syndiotactic, and atactic configurations. Isotactic PP is the most utilized type of polypropylene because it is easy to use, it has high heat resistance, it is physically not transparent, and it is resistant to chemical solvents (making it suitable or storing food and drinks). The most influential degradation process concerning polypropylene is photooxidative degradation, which requires exposure to sunlight and oxygen to produce polar carbonyl groups, esters, ketones, and acids, thereby improving the hydrophilic characteristic of polypropylene. Untreated and treated PP microplastic spectra are presented in Fig. 4. In all the spectra, asymmetric and symmetric -C-H stretch from CH_3 was detected at 2949.4 cm^{-1}, 2872.2 cm^{-1}, respectively, while the same stretches from $-CH_2$ appeared at 2917.4 cm^{-1} and 2836.1 cm^{-1} [35].

Figure 4. FTIR spectra of PP and PP/Plasma, PP/ UV, PP/O3.

Peaks in the region 990-800 belong to alkyl -C-H bending. After the treatment with O_3 and UV, there was significant increase in peak intensities, but without generation of new bonds, with the exception of -OH band centered around 3384.4 cm^{-1} in PP/O_3. On the other side, after the plasma treatment of PP, similar to PE/PL, C=O bond was observed at 1725.4 cm^{-1} in PP/PL.

N-H bending from primary amine appeared at 1603.1 cm^{-1} [32]. Plasma-formed ether groups appeared 1248.6 cm^{-1} and 1167.4 cm^{-1}.

Photodegradation of polystyrene, such as increased brittleness and discoloration, occurs similarly to polyethylene (PE) and polypropylene (PP) when exposed to the UV component of sunlight. Polystyrene loses its mechanical and tensile properties due to the effects of UV light and heat. UV radiation induces the production of radicals through oxidation, and these radicals cause the breakdown of polymer chains. Hydroxyl group in all PS microplastic spectra (Fig. 4.) is located at 3389.3 cm^{-1}. In the region 3084.8-3034.6 cm^{-1} -C-H stretch from aromatic benzene rings was observed, while asymmetric and symmetric aliphatic -C-H stretch from -CH_2 appeared at 2922.3 cm^{-1} and 2854.2 cm^{-1} [36]. The peaks at 1493.3 cm^{-1} and 1452.3 cm^{-1} originated from the deformational vibrations of in the benzene ring [37]. Similar as in PE and PP spectra, peak intensity change was observed in PS/O_3, PS/UV and PS/PL. However, newly formed bonds were not detected after plasma treatment.

Figure 5. FTIR spectra of PS and PS/Plasma, PS/UV, PS/O3.

3.3. Raman spectroscopy

The Raman spectra were taken in the backscattering configuration by Jobin Yvon T64000 spectrometer, equipped with nitrogen cooled charged coupled device detector. As an excitation source we used the 514.5 nm line of Ti:Sapphire laser, with the laser power 60mW. The measurements were performed in the spectrum range 70-3600cm^{-1}. Raman spectroscopy provides information about changes in the polarizability of chemical bonds during molecular vibrations. Specifically, vibrations of C–C, C=C bonds, and aromatic rings in polymers cause polarizability changes, making this technique suitable for the label-free identification of microplastic particles. While Raman spectroscopy offers several advantages, including submicron spatial resolution, it is highly susceptible to fluorescence interferences, which can be particularly prevalent in environmental samples [37]. These interferences might be attributed to degradation effects or adsorbed contaminants. Fluorescence emission can superimpose a broad background on the typically weaker Raman scattered signal, making reliable identification of particles challenging. Furthermore, the Raman spectra of colored and pigmented microplastic samples may be distorted by fluorescent emission or resonantly enhanced Raman signals from dyes, overshadowing the characteristic fingerprint signature of the plastic particle. In our case, Raman spectroscopy provided very satisfactory results in characterizing the optical properties of microplastics (PE, PS and PP).

Figure 6. Raman spectra of PE and PE/Plasma, PE/O3, PE/UV.

In Figure 6, the Raman spectrum of PE is shown, along with spectra of PE treated by O_3, UV, and plasma. The Raman bands between 1000 and 1500 cm^{-1} indicate photodegradation, as such reactions lead to chain scission and the formation of carbonyl and vinyl groups in the molecular structure of PE. The Raman spectrum of PE can be divided into three key regions: Region I (1040–1200 cm^{-1}) is primarily associated with C–C stretching; Region II (around 1300 cm^{-1}) features –CH_2- twisting; and Region III (1350–1500 cm^{-1}) is dominated by –CH_2- bending [38]. In Region I, the broad band at 1075 cm^{-1} is linked to the amorphous phase. In Region III, more specifically, the 1418 cm^{-1} peak corresponds to CH_2 bending and wagging and is characteristic of the orthorhombic phase. The 1440 cm^{-1} peak is attributed to CH_2 deformation in the amorphous trans regions, while the 1462 cm^{-1} peak arises from CH_2 bending in the amorphous regions of PE. In the spectrum of polyethylene (PE) subjected to plasma treatment, significant bond cleavage of carbon-carbon (C–C) and carbon-hydrogen (C–H) bonds in the polymer chains is observed. This is primarily due to the bombardment by ions in the plasma, which break these bonds, leading to molecular-level damage at the surface. The breaking of these bonds causes surface modification, notably increasing the roughness of the polyethylene at the nanoscale level. This process of bond breaking and surface etching is a consequence of the energetic ion bombardment characteristic of plasma treatments.

Figure 7 presents the Raman spectrum of PP, along with spectra of PP treated by O_3, UV, and plasma. The primary Raman bands for PP were observed near 399, 810, 841, 1153, 1330, 1371, and 1460 cm^{-1}. These bands were generally more intense than those detected in FTIR, with their intensities showing variations relative to the methyl-associated bands at 1371 and 1460 cm^{-1}. Specifically, the bands at 399, 810, 841, and 1330 cm^{-1} correspond to different CH and CH_2 deformation vibrations, while the bands at 974 and 999 cm^{-1} are attributed to CH_3 deformation vibrations. The bands at 1153 and 1168 cm^{-1} are linked to CC stretching vibrations [39].

Figure 7. Raman spectra of PP and PP/Plasma, PP/ UV, PP/O3.

When PP is exposed to O_3 and UV treatments, the spectral intensity experiences a significant reduction, signaling notable degradation of the material. This decrease in Raman signal intensity indicates that the structural integrity of the polymer has been substantially compromised due to these treatments. The degradation processes triggered by ozone and ultraviolet light lead to changes in the molecular structure of PP, weakening the polymer and thereby diminishing its Raman response. This observation emphasizes the vulnerability of PP to environmental stressors and highlights the extent of structural transformation under such conditions. Exposure of polypropylene to ozone leads to oxidative degradation, beginning with the scission of carbon-carbon (C–C) and carbon-hydrogen (C–H) bonds within the polymer chain. This degradation results in a weakened polymer structure, which causes a significant reduction in the mechanical properties of polypropylene. Continuous exposure to ozone over time accelerates the materials embrittlement, making polypropylene brittle and more prone to cracking.

Raman spectroscopy of polystyrene (PS), shown in Fig. 8, primarily reveals vibrational bands linked to the aromatic ring structure. In the spectral region around 3100 cm^{-1}, we observe C-H stretching vibrations within these aromatic rings. This region represents the stretching of carbon-hydrogen bonds in the phenyl groups, a key feature of polystyrenes chemical structure. Specifically, peaks in this area correspond to the symmetric and asymmetric stretching modes of these C-H bonds [39].

Figure 8. Raman spectra of PS and PS/Plasma, PS/UV, PS/O3.

These stretching modes show how hydrogen atoms in the phenyl groups move relative to the carbon atoms they are bonded to, highlighting the polymers chemical nature. If there is any bond scission (breaking of bonds) occurring, it can lead to a decrease or shift in the intensity of these peaks. Monitoring these changes is crucial as they can indicate whether degradation is affecting the polystyrenes molecular structure, which could result in a loss of its mechanical properties and overall material performance. The spectrum (Fig. 7.) shows a sharp increase in the intensity of the peak at 3100 cm^{-1} upon exposure to UV radiation. This increase in peak intensity indicates a change in the surface properties of the microplastics. UV degradation can lead to surface chemical modifications in polystyrene, where the formation of oxidized products or other chemical species enhances the active Raman vibrations. The chemical reactions that can explain what happens to polystyrene during the phases are shown:

1. **Photoinitiation and Radical Formation**

   UV radiation can cause the dissociation of C-H bonds in the polystyrene chain, leading to the formation of free radicals.

- Photoinitiation:

  $PS{-}C_6H_5{-}CH_2{-}CH_2{-}PS \rightarrow PS{-}C_6H_5{-}\cdot CH_2 + \cdot CH_2{-}PS$

  Where $\cdot CH_2$ represents the free radical generated by UV exposure.

2. **Formation of Oxygenated Products**

   The free radicals generated under UV exposure can react with oxygen from the environment, forming hydroxyl (-OH) and carbonyl (C=O) groups. These groups can contribute to increased intensity of the C-H vibrations.

- Radical reaction with oxygen:

  $\cdot CH_2 + O_2 \rightarrow CH_2OH$ or

  $\cdot CH_2 + O \rightarrow CH_2C{=}O$ (carbonyl group)

3. **Chain Scission and Oxidation**

   UV radiation can lead to chain scission of the polystyrene backbone, causing oxidation of the fragments and the formation of carbonyl or hydroxyl products.

- Chain scission and oxidation:

  $PS{-}C_6H_5{-}\cdot CH_2 + O_2 \rightarrow PS{-}C_6H_5{-}C{=}O$

4. **Reorganization of Aromatic Rings**

   UV radiation can also induce structural changes and reorganization in the phenyl groups (aromatic rings), resulting in enhanced C-H stretch vibrations within the phenyl rings, leading to the increased intensity of the peak at 3100 cm^{-1}.

- Reorganization of the phenyl group:

  $C_6H_5 \rightarrow C_6H_5^*$ (reorganized phenyl group with enhanced vibrations)

5. **Final Degradation Products**

   The ultimate degradation of polystyrene under UV exposure results in the formation of smaller molecules such as formaldehyde (HCHO), acetaldehyde (CH_3CHO), or other oxidation products.

- Final oxidation:

  $CH_2{-}CH{-}C_6H_5 \rightarrow CH_2OH + C_6H_5CHO + H_2O_2$

The conclusions regarding the mechanisms occurring during UV degradation of polystyrene are based on the results of our experiments conducted using Raman, FTIR, and UV-VIS spectroscopy. Based on the spectral changes recorded during UV treatment, we monitored key processes including the formation of free radicals, oxidation, polymer chain degradation, and the formation of smaller molecules.

Photoinitiation and Radical Formation: UV radiation causes the dissociation of C-H bonds in the polystyrene chain, leading to the formation of free radicals (·CH2). This process triggers the subsequent degradation pathway, which was confirmed through Raman spectroscopy, where an increase in specific peaks corresponding to the vibrations of free radicals was observed.

Formation of Oxygenated Products: The free radicals react with oxygen from the environment, forming hydroxyl (-OH) and carbonyl (C=O) groups. These new functional groups contribute to an increase in the intensity of C-H vibrations, which was also confirmed by experiments showing an increase in signals in the Raman and FTIR spectra, particularly in the 3100 cm^{-1} region.

Chain Scission and Oxidation: UV radiation can lead to the chain scission of the polystyrene backbone, causing oxidation of the fragments and the formation of carbonyl and hydroxyl products. This chain degradation process is clearly manifested in spectroscopic analyses, which show the presence of oxidation products such as aldehydes and alcohols.

Reorganization of Aromatic Rings: UV radiation can also induce structural changes in the phenyl groups (aromatic rings), resulting in enhanced C-H vibrations within these rings. The increased intensity of Raman peaks in the 3100 cm^{-1} region indicates this reorganization.

Final Degradation Products: Ultimately, the degradation of polystyrene under UV exposure leads to the formation of smaller molecules, such as formaldehyde (HCHO), acetaldehyde (CH_3CHO), and other oxidation products. These products were identified through spectroscopic techniques, where peaks indicating the formation of aldehydes and other smaller molecules were observed.

Based on these experiments, we conclude that UV radiation induces the formation of free radicals, oxidation, and polymer chain scission, leading to the formation of new functional groups and ultimately smaller molecules, including formaldehyde and acetaldehyde. These conclusions are not directly taken from the literature but are derived from our experimental data and the spectral changes observed during treatment.

4. Conclusion

In the future, plastics production is expected to continue its upward trend, further exacerbating the issue of plastics pollution, which can no longer be ignored. With the increasing severity of microplastics pollution, it has become essential to explore effective methods for its degradation. This study examined and compared the effects of ozone, UV radiation, and plasma on the degradation of three types of microplastics. The optical changes resulting from these degradation processes were detected and analyzed using Raman and FTIR spectroscopy.

The study specifically explained the effects and mechanisms of degradation, with a focus on polystyrene as one of the most common types of microplastics. FESEM revealed significant morphological changes in the surface of polystyrene after plasma treatment, including increased surface roughness and visible structural alterations. Among the tested treatments, plasma showed the most pronounced effect, highlighting its potential for breaking down microplastics efficiently.

A significant increase in the intensity of the peak at 3100 cm^{-1} in the Raman spectrum of polystyrene after exposure to UV radiation indicates substantial changes on the surface of the microplastic material. Additionally, the study presented the chemical reactions that thoroughly explain this process. Through these techniques, the study provided detailed insights into how each treatment method influenced the chemical and structural properties of the microplastics.

Therefore, the gained insights could be further utilized to optimize the microplastics treatment for known microplastics types or to plan more general degradation protocols, which could then synergistically use a combination of the above techniques to tackle a wider range of microplastics specimens. In conclusion, our study critically assessed several solutions for the management of microplastics. The main focus and motivation for this study lied in the need for sustainable development and large-scale application of microplastics degradation in the future, and the results presented herein provide valuable suggestions for environmental management and policymaking by governments and environmental agencies.

Acknowledgements

This work has been supported by The Science Fund of the Republic of Serbia, Green program of cooperation between science and industry, grant no. 5661. Any opinions, findings, conclusions or recommendations expressed are those of the authors and do not necessarily reflect the views of the funder.

References

[1] Alimi, O.S., Farner Budarz, J., Hernandez, L.M., Tufenkji, N., 2018. Microplastics and nanoplastics in aquatic environments: aggregation, deposition, and enhanced contaminant transport. Environ. Sci. Technol. https://doi.org/10.1021/acs.est.7b05559.

[2] Bandaru, S., Ravipati, M., Busi1, K.B., Phukan, P., Bag, S., Chandu, B., Dalapati, G.K., Biring, S., Chakrabortty, S., 2024. A review on the fate of microplastics: their degradation and advanced analytical characterization. J. Polym. Environ. 32, 2532–2550. https://doi.org/10.1007/s10924-023-03102-7.

[3] Borrelle, S.B., Ringma, J., Law, K.L., Monnahan, C.C., Lebreton, L., McGivern, A., Murphy, E., Jambeck, J., Leonard, G.H., Hilleary, M.A., Eriksen, M., Possingham, H. P., De Frond, H., Gerber, L.R., Polidoro, B., Tahir, A., Bernard, M., Mallos, N., Barnes, M., Rochman, C.M., 2020. Predicted growth in plastic waste exceeds efforts to mitigate plastic pollution. Science 369 (6510), 1515–1518. https://doi.org/10.1126/science.aba3656.

[4] Jayanth, D., Kumar, P.S., Nayak, G.C., Kumar, J.S., Pal, S.K., Rajasekar, R., 2018. A review on biodegradable polymeric materials striving towards the attainment of green environment. J. Polym. Environ. 26, 838–865. https://doi.org/10.1007/s10924-017-0985-6.

[5] Phadke, G., Rawtani, D., 2023. Bioplastics as polymeric building blocks: Paving the way for greener and cleaner environment. Eur. Polym. J. 199, 112453. https://doi.org/10.1016/j.eurpolymj.2023.112453.

[6] Valentini, F., Dorigato, A., Pegoretti, A., 2020. Evaluation of the role of devulcanized rubber on the thermo-mechanical properties of polystyrene. J. Polym. Environ. 28, 1737–1748. https://doi.org/10.1007/s10924-020-01717-8.

[7] Purohit, V.B., Pięta, M., Pietrasik, J., Plummer, C.M., 2024. Towards sustainability and a circular economy: ROMP for the goal of fully degradable and chemically recyclable polymers. Eur. Polym. J. 208, 112847. https://doi.org/10.1016/j.eurpolymj.2024.112847.

[8] Rillig, M.C., Kim, S.W., Kim, T.-Y., Waldman, W.R., 2021. The global plastic toxicity debt. Environ. Sci. Technol. 55 (5), 2717–2719. https://doi.org/10.1021/acs.est.0c07781.

[9] Nguyen, B., Claveau-Mallet, D., Hernandez, L.M., Xu, E.G., Farner, J.M., Tufenkji, N., 2019. Separation and analysis of microplastics and nanoplastics in complex environmental samples. Acc. Chem. Res. 52 (4), 858–866. https://doi.org/10.1021/acs.accounts.8b00602.

[10] Barchiesi, M., Chiavola, A., Di Marcantonio, C., Boni, M.R., 2021. Presence and fate of microplastics in the water sources: focus on the role of wastewater and drinking water treatment plants. J. Water Process Eng. 40, 101787 https://doi.org/10.1016/j. jwpe.2020.101787.

[11] Li, C., Busquets, R., Campos, L.C., 2020. Assessment of microplastics in freshwater systems: a review. Sci. Total Environ. 707, 135578 https://doi.org/10.1016/j. scitotenv.2019.135578.

[12] Sharma, S., Basu, S., Shetti, N.P., Nadagouda, M.N., Aminabhavi, T.M., 2021. Microplastics in the environment: Occurrence, perils, and eradication. Chem. Eng. J. 408, 127317. https://doi.org/10.1016/j.cej.2020.127317.

[13] Nakatani, H., Kyan, T., Urakawa, Y., 2021. Novel recycling system of polystyrene water debris with polymer photocatalyst and thermal treatment. J. Polym. Environ. 29, 1467–1476. https://doi.org/10.1007/s10924-020-01976-5.

[14] Ren, J., Li, J., Zhen, Y., Wang, J., Niu, Z., 2022. Removal of polyvinyl chloride microplastic by dielectric barrier discharge plasma. Sep. Purif. Technol. 290, 120832. https://doi.org/10.1016/j.seppur.2022.120832.

[15] Coyle, R., Hardiman, G., Driscoll, K.O., 2020. Microplastics in the marine environment: a review of their sources, distribution processes, uptake and exchange in ecosystems. Case Stud. Chem. Environ. Eng. 2, 100010. https://doi.org/10.1016/j. cscee.2020.100010.

[16] Gigault, J., El Hadri, H., Nguyen, B., Grassl, B., Rowenczyk, L., Tufenkji, N., Feng, S., Wiesner, M., 2021. Nanoplastics are neither microplastics nor engineered nanoparticles. Nat. Nanotechnol. 16(5), 501–507. https://doi.org/10.1038/s41565- 021-00886-4.

[17] Razumovskii, S.D., Kefeli, A.A., Zaikov, G.E., 1971. Degradation of polymers in reactive gases. Eur. Polym. J. 7(3), 275–285. https://doi.org/10.1016/0014-3057(71)90111-X.

[18] He, G-J., Zheng, T-T., Ke, D-M., Cao, X-W., Yin, X-C., Xu, B-P., 2015. Impact of rapid ozone degradation on the structure and properties of polypropylene using a reactive extrusion process. RSC Adv. 55(5), 44115–44120. https://doi.org/10.1039/C5RA06652B.

[19] Sinyavsky, N., Korneva, I., 2017. Study of optical properties of polymeric materials subjected to degradation. J. Polym. Environ. 25, 1280–1287. https://doi.org/10.1007/s10924-016-0908-y

[20] Zepp, R.G., Acrey, B., Davis, M.J.B., Andrady, A.L., Locklin, J., Arnold, R., Okungbowa, O., Commodore , A., 2023. Weathering effects on degradation of low-density polyethylene-nanosilica composite with added pro-oxidant. J. Polym. Environ. 31, 4184–4192. https://doi.org/10.1007/s10924-023-02864-4.

[21] Rajakumar, K., Sarasvathy, V., Thamarai Chelvan, A., Chitra, R., Vijayakumar, C.T., 2009. Natural weathering studies of polypropylene. J Polym Environ 17, 191–202. https://doi.org/10.1007/s10924-009-0138-7.

[22] Castro Monsores, K.G., de; Silva, A.O., da; Sant' Ana Oliveira, S., de; Weber, R.P., Filho, P.F., Monteiro, S.N., 2021. Influence of ultraviolet radiation on polystyrene. J. Mater. Res. Technol. 13, 359–365. https://doi.org/10.1016/j.jmrt.2021.04.035.

[23] Mierzwa-Hersztek, M., Gondek, K., Kopeć, M., 2019. Degradation of polyethylene and biocomponent-derived polymer materials: An overview. J. Polym. Environ 27, 600–611. https://doi.org/10.1007/s10924-019-01368-4.

[24] Jakubowicz, I., Enebro, J., Yarahmadi, N., 2021. Challenges in the search for nanoplastics in the environment—a critical review from the polymer science perspective. Polym. Test. 93, 106953. https://doi.org/10.1016/j. polymertesting.2020.106953.

[25] Ranjan, V.P., Joseph, A., Goel, S., 2021. Microplastics and other harmful substances released from disposable paper cups into hot water. J. Hazard. Mater. 404, 124118. https://doi.org/10.1016/j.jhazmat.2020.124118.

[26] Luo, H., Zhao, Y., Li, Y., Xiang, Y., He, D., Pan, X., 2020. Aging of microplastics affects their surface properties, thermal decomposition, additives leaching and interactions in simulated fluids. Sci. Total Environ. 714, 136862 https://doi.org/10.1016/j. scitotenv.2020.136862.

[27] Jeon, H.J., Kim, M.N., 2014. Degradation of linear low density polyethylene (LLDPE) exposed to UV-irradiation. Eur. Polym. J. 52, 146–153. https://doi.org/10.1016/j.eurpolymj.2014.01.007.

[28] Gururani, P., Bhatnagar, P., Bisht, B., Kumar, V., Chandra Joshi, N., Tomar, M.S., Pathak, B., 2021. Cold plasma technology: advanced and sustainable approach for wastewater treatment. Environ. Sci. Pollut. Res. 28, 65062–65082. https://doi.org/10.1007/s11356-021-16741-x.

[29] Aggelopoulos C.A., 2022. Recent advances of cold plasma technology for water and soil remediation: A critical review. Chem. Eng. J. 428, 131657. https://doi.org/10.1016/j.cej.2021.131657.

[30] Fan, C., Huang, Y-Z., Lin, J-N., Li, J., 2021. Microplastic constituent identification from admixtures by Fourier-transform infrared (FTIR) spectroscopy: The use of polyethylene terephthalate (PET), polyethylene (PE), polypropylene (PP), polyvinyl chloride (PVC) and nylon (NY) as the model constituents. Environ. Technol. Innov. 23, 101798. https://doi.org/10.1016/j.eti.2021.101798.

[31] Murthy, V.S.M.D., Vaidya, U., 2019. Improving the adhesion of glass/polypropylene (glass-PP) and high-density polyethylene (HDPE) surfaces by open air plasma treatment. International Journal of Adhesion and Adhesives, 1024355. https://doi.org/10.1016/j.ijadhadh.2019.102435.

[32] Onyshchenko, Y., Chan, K.V., De Geyter, N., Morent, R., 2021. Spectroscopic analysis of plasma modified polymer surfaces. Plasma Modification of Polyolefins. In: Engineering Materials. https://doi.org/10.1007/978-3-030-52264-3_6.

[33] Ataeefard, M., Moradian, S., Mirabedini, M., Ebrahim, M., Asiaban, S., 2008. Surface properties of low density polyethylene upon low-temperature plasma treatment with various gases. Plasma Chem. Plasma Process. https://doi.org/10.1007/s11090-008-9126-2.

[34] Wang, C.Y., Schön, M., Horn, T., Facklam, M., Dahlmann, R., Hopmann, C., He, G-J., 2022. Usage of atmosphere pressure plasma for rapid polyethylene functionalisation exhibiting only minor ageing. Eur. Polym. J. 181, 111669. https://doi.org/10.1016/j.eurpolymj.2022.111669.

[35] Khoironi, A., Hadiyanto, H., Anggoro, S., Sudarno, S., 2020. Evaluation of polypropylene plastic degradation and microplastic identification in sediments at Tambak Lorok coastal area, Semarang, Indonesia. Marine Pollution Bulletin 2020, 110868. https://doi.org/10.1016/j.marpolbul.2019.110868.

[36] Dong, Y., Gao, M., Song, Z., Qiu, W., 2020. As(III) adsorption onto different-sized polystyrene microplastic particles and its mechanism. Chemosphere 239, 124792. https://doi.org/10.1016/j.chemosphere.2019.124792.

[37] Pushpadass, H.A., Weber, R.W., Dumais, J.J., Hanna, M.A., 2010. Biodegradation characteristics of starch-polystyrene loose-fill foams in a composting medium. Bioresour. Technol. 101(19), 7258–7264. https://doi:10.1016/j.biortech.2010.04.039.

[38] Primpke, S., Godejohann, M., Gerdts, G, 2020. Rapid identifcation and quantifcation of microplastics in the environment by quantum cascade laser-based hyperspectral infrared chemical imaging. Environ. Sci. Technol. 54, 15893–15903. https://doi.org/10.1021/acs.est.0c05722.

[39] Smith, M., Love, D.C., Rochman, C.M., Neff, R.A., 2018. Microplastics in seafood and the implications for human health. Curr. Environ. Health Rep. 5, 375–386. https://doi.org/10.1007/s40572-018-0206-z.

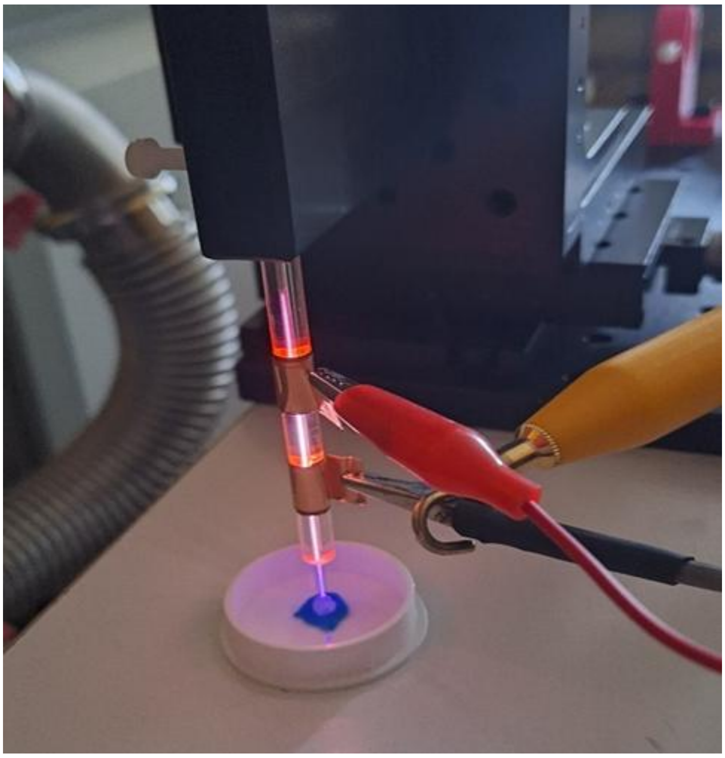

Figure 1. Setup used for plasma treatment.

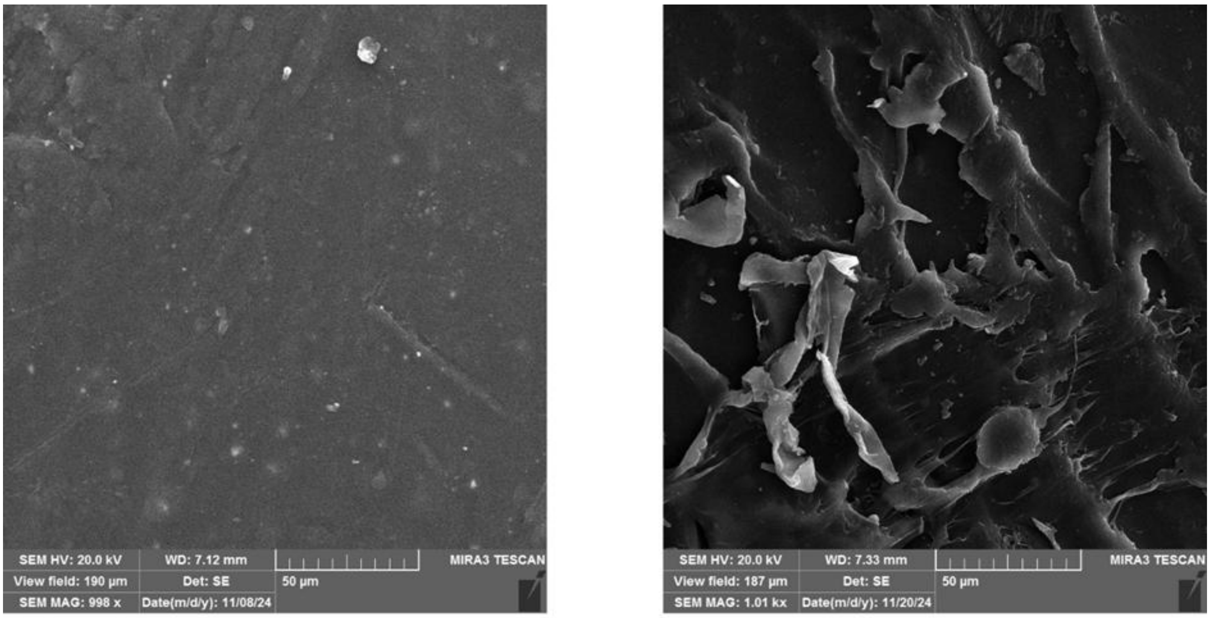

a) b)

Figure 2. FESEM images: a) PS before degradation and b) PS after degradation plasma.

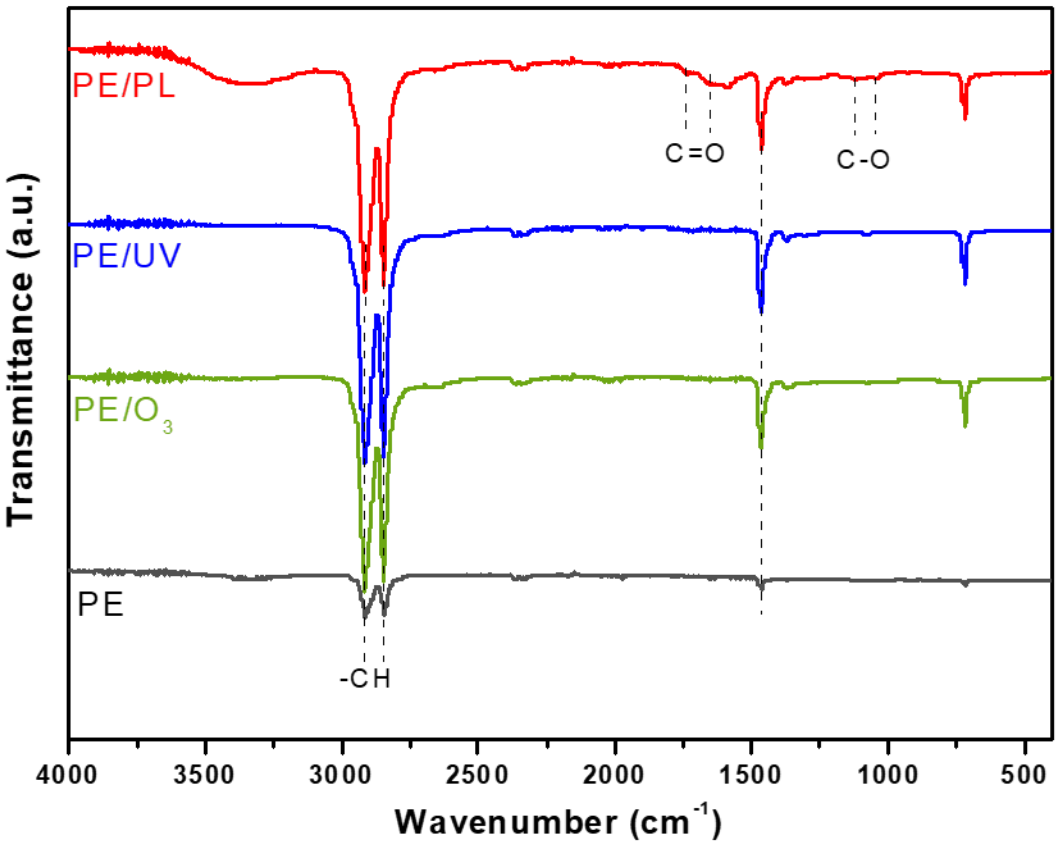

Figure 3. FTIR spectra of PE and PE/Plasma, PE/O3, PE/UV.

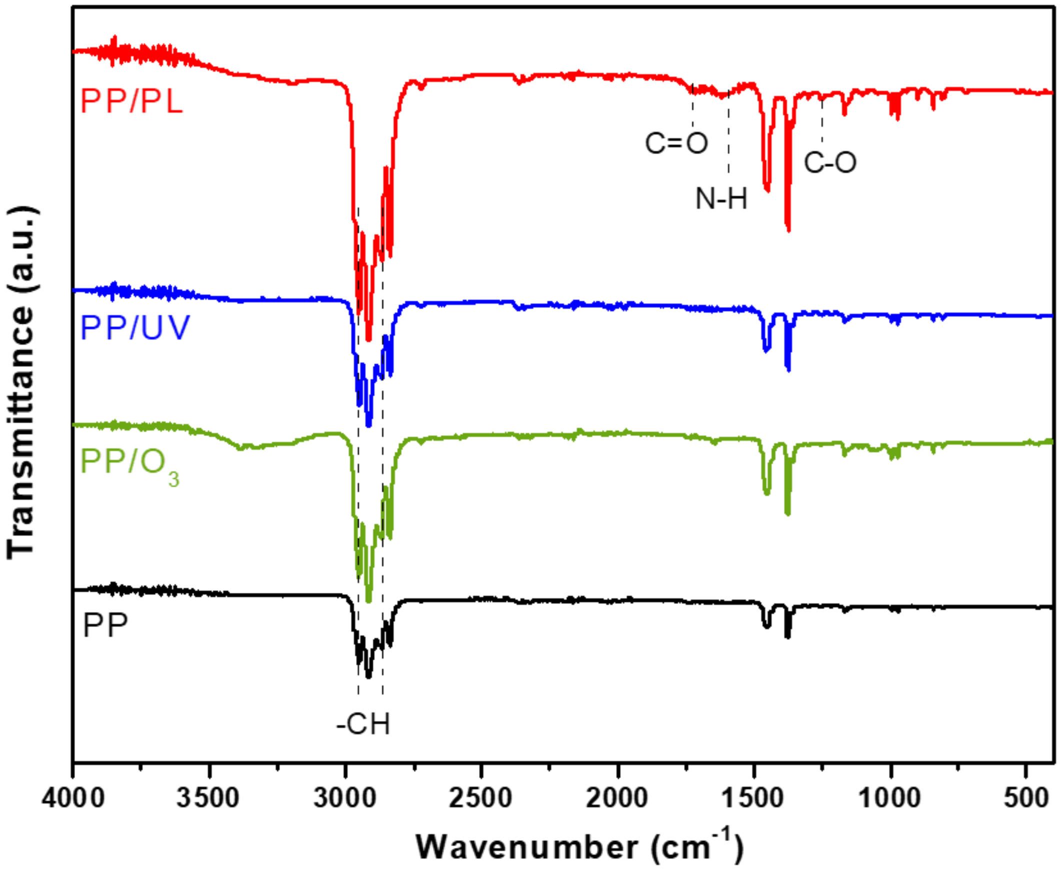

Figure 4. FTIR spectra of PP and PP/Plasma, PP/ UV, PP/O3.

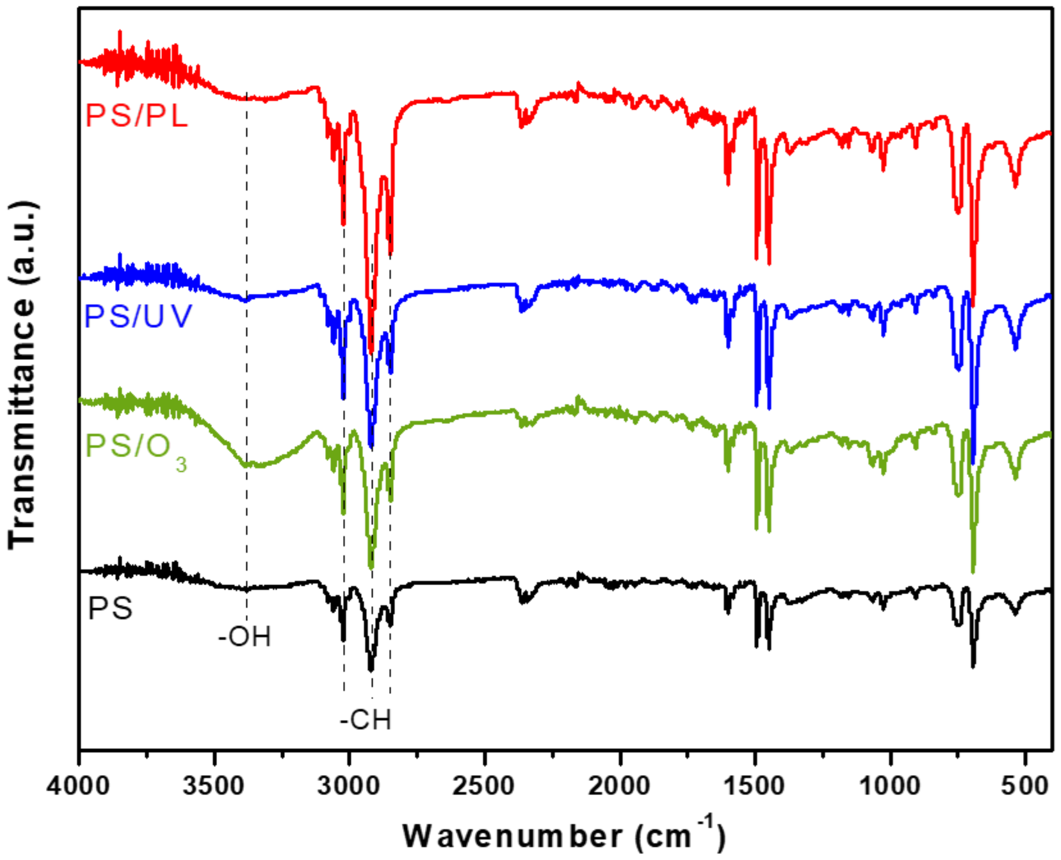

Figure 5. FTIR spectra of PS and PS/Plasma, PS/UV, PS/O3.

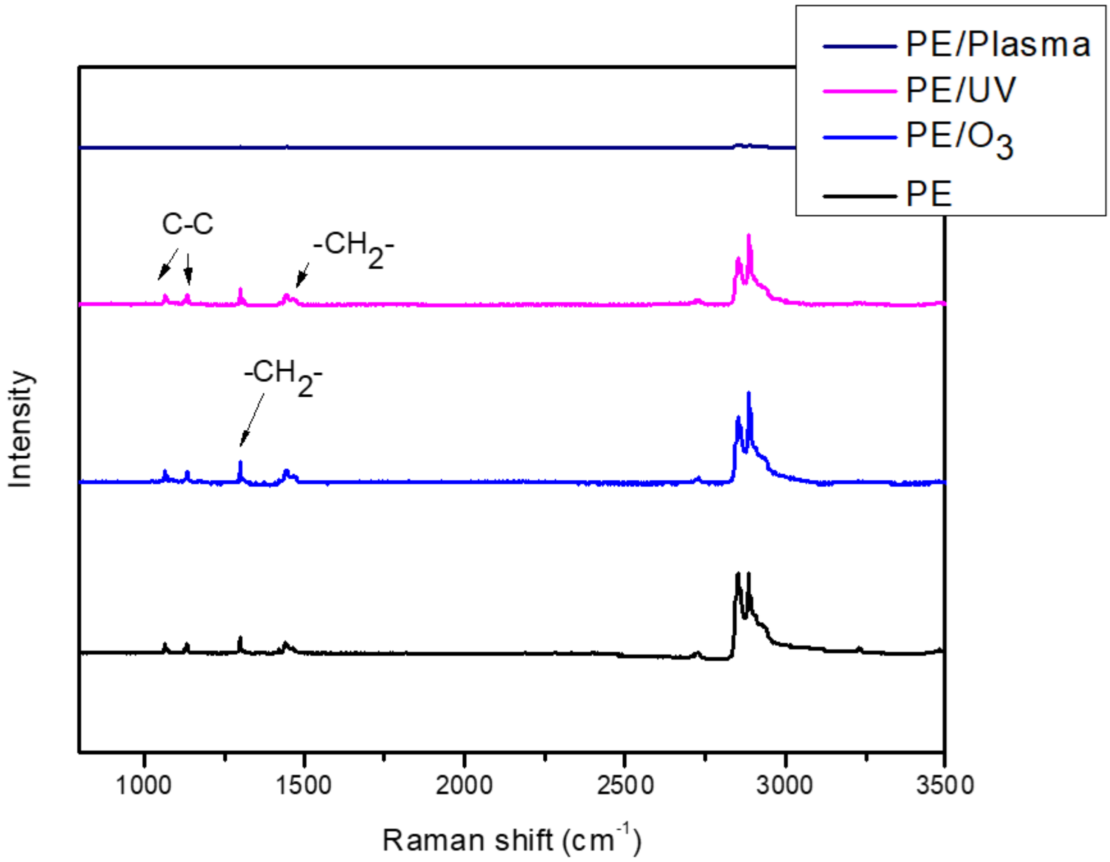

Figure 6. Raman spectra of PE and PE/Plasma, PE/O3, PE/UV.

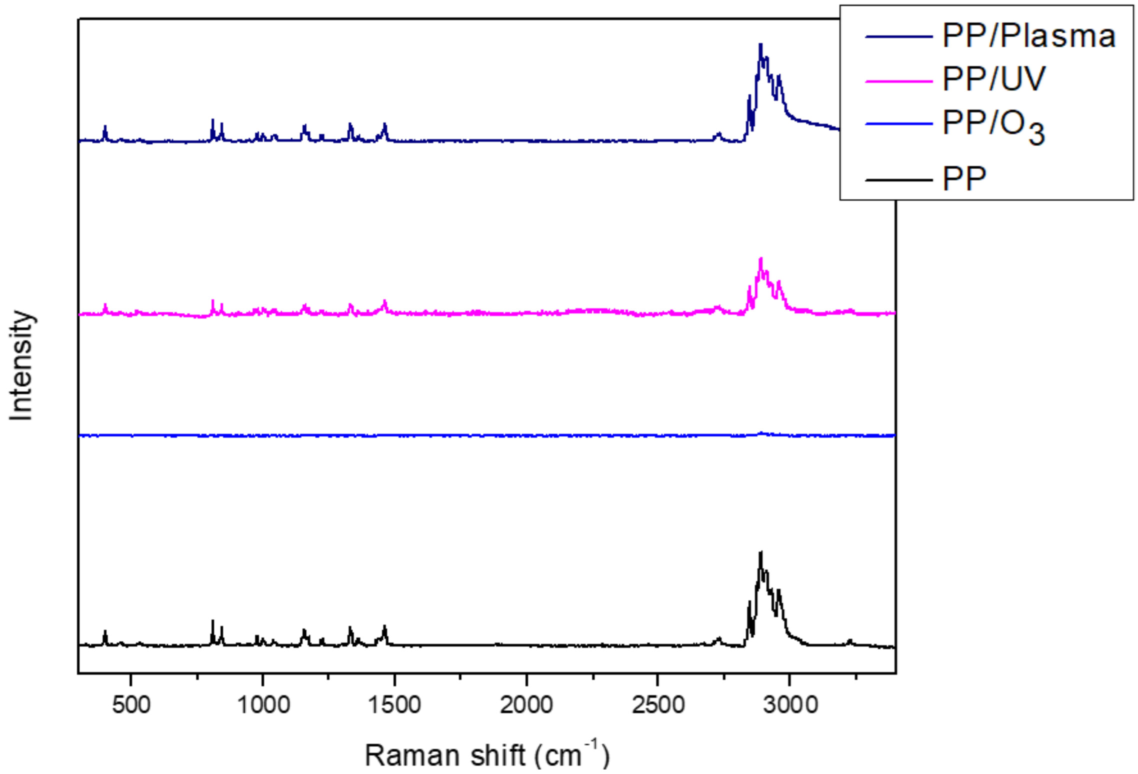

Figure 7. Raman spectra of PP and PP/Plasma, PP/ UV, PP/O3.

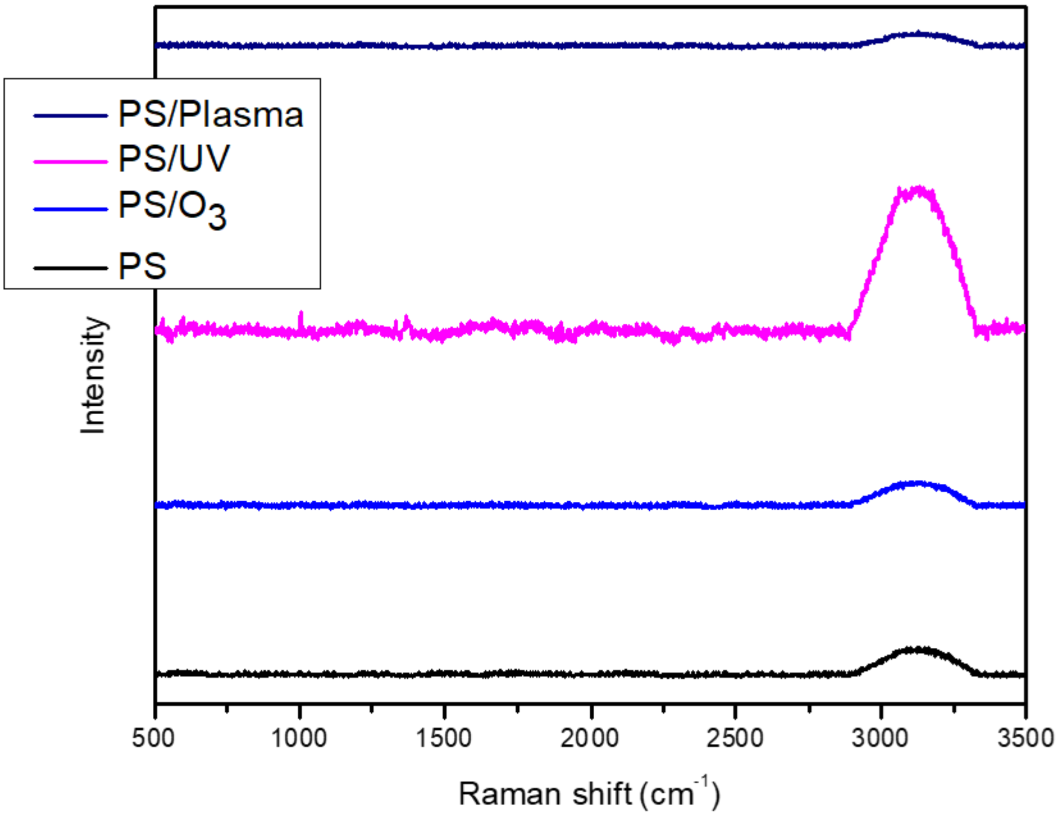

Figure 8. Raman spectra of PS and PS/Plasma, PS/UV, PS/O3.

Figure 1. Setup used for plasma treatment.

Figure 2. FESEM images: a) PS before degradation and b) PS after degradation plasma.

Figure 3. FTIR spectra of PE and PE/Plasma, PE/O3, PE/UV.

Figure 4. FTIR spectra of PP and PP/Plasma, PP/ UV, PP/O3.

Figure 5. FTIR spectra of PS and PS/Plasma, PS/UV, PS/O3.

Figure 6. Raman spectra of PE and PE/Plasma, PE/O3, PE/UV.

Figure 7. Raman spectra of PP and PP/Plasma, PP/ UV, PP/O3.

Figure 8. Raman spectra of PS and PS/Plasma, PS/UV, PS/O3.

processes

MDPI

Article

Comparison of the Bacterial Inactivation Efficiency of Water Activated by a Plasma Jet Source and a Pin-to-Pin Electrode Configuration Source

Radovan Čobanović [1,*], Dejan Maletić [2], Sunčica Kocić-Tanackov [1], Ivana Čabarkapa [3], Bojana Kokić [3], Predrag Kojić [1], Slobodan Milošević [4], Višnja Stulić [5], Tomislava Vukušić Pavičić [5] and Milan Vukić [6]

[1] Faculty of Technology, University of Novi Sad, Bulevar cara Lazara 1, 21000 Novi Sad, Serbia; suncicat@uns.ac.rs (S.K.-T.); kojicpredrag@uns.ac.rs (P.K.)
[2] Institute of Physics, University of Belgrade, Pregrevica 118, 11080 Belgrade, Serbia; dejan_maletic@ipb.ac.rs
[3] Institute of Food Technology, University of Novi Sad, Bulevar cara Lazara 1, 21000 Novi Sad, Serbia; ivana.cabarkapa@fins.uns.ac.rs (I.Č.); bojana.kokic@fins.uns.ac.rs (B.K.)
[4] Institute of Physics, Bijenička cesta 46, 10000 Zagreb, Croatia; slobodan@ifs.hr
[5] Department of Food Engineering, Faculty of Food Technology and Biotechnology, University of Zagreb, Pierottijeva 6, 10000 Zagreb, Croatia; vstulic@pbf.hr (V.S.); tomislava.vukusic.pavicic@pbf.unizg.hr (T.V.P.)
[6] Faculty of Technology Zvornik, University of East Sarajevo, Karakaj 34a, 75400 Zvornik, Bosnia and Herzegovina; milan.vukic@tfzv.ues.rs.ba
* Correspondence: radovan.cobanovic@splaboratorija.rs

Abstract: In this comparative study, the bacterial inactivation efficiency of plasma-activated water (PAW) generated by two distinct plasma reactors, one utilizing a nitrogen plasma jet electrode and the other a hybrid argon plasma reactor, was explored. The present study involved the assessment of antimicrobial activity against suspensions of three Gram-positive and three Gram-negative bacterial strains in their planktonic cell state. Bacterial suspensions were introduced into PAW five days after generation. Subsequently, the viability of the bacteria was assessed at various time intervals, specifically at 0.5, 1, 3, 5, 10, and 24 h, in order to evaluate the effect of inactivation. Structural changes in bacteria after PAW treatment were assessed using a scanning electron microscope (SEM). The physicochemical properties of PAW, including pH, conductivity, and concentrations of H_2O_2, NO_2^-, and NO_3^- during aging were measured. The present study demonstrated the effective inactivation of the tested bacterial strains by PAW. Gram-positive bacteria displayed greater resistance compared to Gram-negative species, with the lowest reductions in bacterial counts observed for *B. cereus*, and the highest for *Escherichia coli* O157:H7. Morphological damage was evident across all bacterial species examined. Physicochemical measurements showed slow decay of the reactive species in the aging process. This study illustrated the potential utility of PAW as an alternative disinfectant.

Keywords: bacteria inactivation efficiency; Gram-positive bacteria; Gram-negative bacteria; PAW; plasma activated water; plasma jet; hybrid plasma discharge; SEM imaging

Citation: Čobanović, R.; Maletić, D.; Kocić-Tanackov, S.; Čabarkapa, I.; Kokić, B.; Kojić, P.; Milošević, S.; Stulić, V.; Pavičić, T.V.; Vukić, M. Comparison of the Bacterial Inactivation Efficiency of Water Activated by a Plasma Jet Source and a Pin-to-Pin Electrode Configuration Source. *Processes* **2023**, *11*, 3286. https://doi.org/10.3390/pr11123286

Academic Editors: Tao Sun, Evgenia Benova and Frantisek Krcma

Received: 11 October 2023
Revised: 20 November 2023
Accepted: 21 November 2023
Published: 24 November 2023

1. Introduction

The threat of microbial contamination in food presents a growing concern for public health worldwide, and it has the potential to occur throughout all phases of food production and processing. The presence of spoilage microorganisms can negatively affect the nutritional value, color, texture, and edibility of food, which causes great economic losses [1], and the presence of pathogens can cause foodborne intoxication and toxicoinfections. The major etiological agents that account for the estimated 1.5 million gastrointestinal deaths each year are enterotoxigenic *Escherichia coli* (ETEC), rotavirus, *Vibrio cholerae*, and *Shigella* spp.; all are known to be endemic in the vast majority of developing countries. While standard assays can effectively identify *V. cholerae*, *Shigella*, and rotavirus, detecting ETEC poses greater challenges, which sometimes leads to its significance as a primary cause of infantile diarrhea or cholera-like illness in individuals of all age groups going unrecognized. Additionally, it can induce traveler's diarrhea in visitors to endemic areas. Indeed, ETEC stands out as the most significant among these four pathogens in causing diarrhea in infants, children, and adults, accounting for 280 million episodes and more than 400,000 deaths annually [2]. Due to the increasing consumer preference for fresh, safe, and nutritionally enriched food products, there has been a substantial surge in research on non-thermal food processing technologies such as high hydrostatic pressure, pulsed electric fields, ultrasound, and cold plasma [3,4]. Cold plasma has attracted a lot of attention recently concerning its usage in the food and agricultural industries, mainly for applications in food sterilization and preservation [4,5]. Plasma, the fourth state of matter, is a partially ionized gas and can be generated by applying high voltage to a gas phase at low, atmospheric, and high pressures or by focused laser beams in a laboratory. There has been a growing focus on innovative approaches to pathogen inactivation, specifically those involving cold atmospheric pressure plasma (CAPP), which refers to plasma generated at atmospheric pressure and near room temperature [6]. Within the plasma, a diverse array of species is abundant, encompassing atoms and molecules in both excited and ground states, along with positive and negative ions, electrons, radicals, and high-energy photons, all characterized by substantial concentrations and fluxes [7]. CAPP has demonstrated its efficacy in surface decontamination, primarily attributed to the presence of active species known for their efficient antimicrobial properties. Nonetheless, the markedly uneven surface texture of food products provides a multitude of concealed areas where microorganisms can thrive, subsequently heightening their resilience to cold plasma treatment. Plasma-activated water (PAW) was developed to solve this problem [8]. PAW, commonly produced by exposing CAPP discharge in water or above the water surface, is an alternative disinfection method [9]. Reactive species in PAW will vary depending on the kinds of gases and liquids utilized to create it. The concentration of the major stable and long-lived reactive species (NO_3^-, NO_2^-, H_2O_2, and pH) can be easily and rapidly measured using QUANTOFIX® test strips [10]. Upon contact with water, CAPP produces a significant concentration of reactive oxygen and nitrogen species (RONS), encompassing both long-lived species like nitrate ($NO3^-$), nitrite ($NO2^-$), hydrogen peroxide (H_2O_2), and ozone (O_3), as well as short-lived species such as hydroxyl ($^\bullet OH$), singlet oxygen ($^1O_2$), superoxide (O_2^-), nitric oxide ($^\bullet NO$), and peroxynitrite ($ONOO^-$) [11,12]. The concentrations of some of these reactive species can be preserved for longer times in PAW by adding Cu metal ions originating from copper foil and nanoparticles [13]. Due to the extensive variety of RONS, PAW has a high oxidation-reduction potential (ORP) and low pH, which provides synergistic effects in the reactivity [14]. Being both environmentally friendly and economically viable, PAW demonstrates remarkable and extensive antibacterial capabilities (Figure 1). This opens up fresh avenues for its application in the realms of food production, agriculture, and the field of biomedicine [8,12,15,16].

Numerous investigations have provided evidence that PAW is highly effective in deactivating a diverse spectrum of microorganisms, encompassing fungi, viruses, bacteria, bacterial spores, and biofilms [8,12,14,16–23]. In prior studies, researchers typically employed plasma-activated water from a single specified source and applied it to a limited number of microorganisms, while the novelty of the present research is reflected in the parallel application of two different plasma sources to several pathogenic species. A significant point to note in relation to food safety is that PAW has been shown to effectively deactivate foodborne pathogens on both food-contact surfaces and food itself, all while having no adverse effects on the environment or human health [23]. Successful examples of inactivating pathogens on different food matrices include strawberries [9], fresh-cut fruits, such as pears, apples, and kiwi [24–26], and chicken meat and skin [27]. Additionally, PAW was also reported to be able to extend the shelf life of shrimp [28], baby spinach leaves [29], eggs [30], and fresh beef [31]. The enhancement of seed germination and plant growth is another potential application of PAW. Reactive species produced from chemical donors play a significant role in the germination of seeds and the development of plants [32]. Altering the characteristics of water through non-thermal plasma and its application may influence the plant growth process, leading to improved agricultural product quality [33]. Moreover, the on-site, on-demand preparation of PAW diminishes the associated risks linked to the transportation and storage of chemicals employed in traditional sanitation procedures. Additionally, it offers a convenient and readily storable alternative to conventional disinfection solutions.

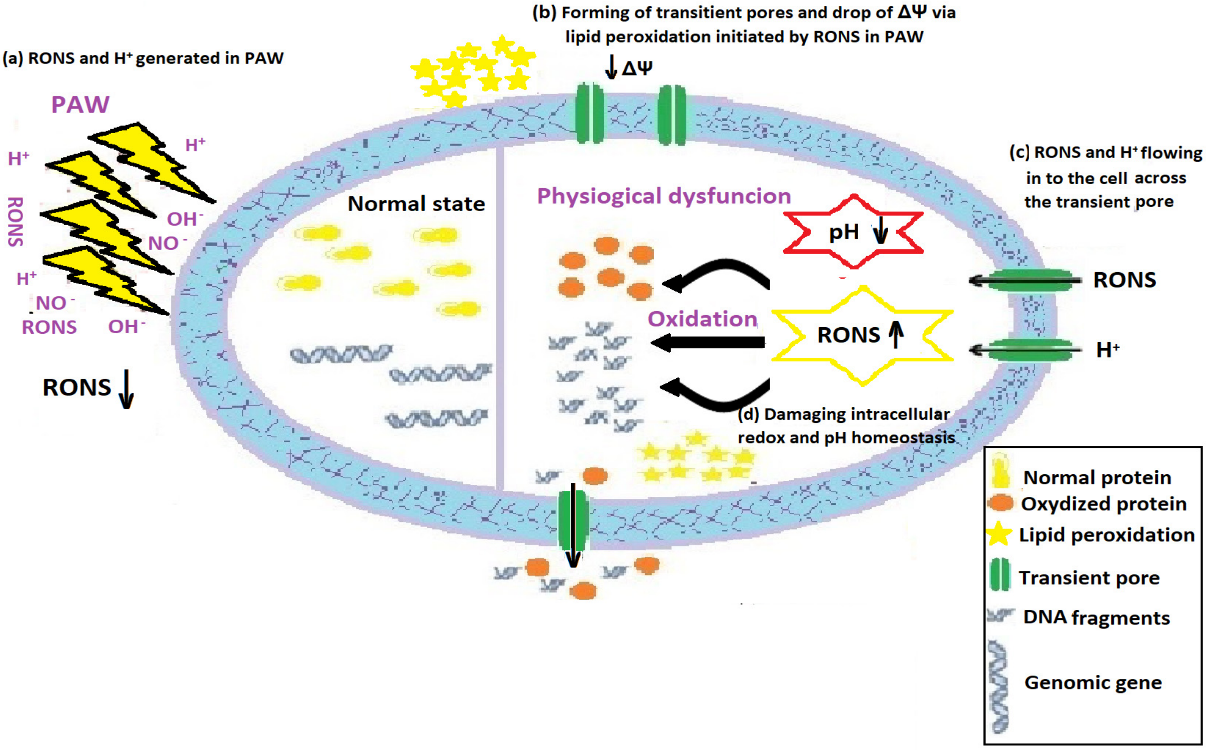

Figure 1. A schematic depiction of the plasma-induced apoptosis process that is divided into four distinct stages: (**a**) the generation of reactive oxygen and nitrogen species (RONS) within plasma-activated water (PAW) and the subsequent acidification of PAW due to plasma treatment of water; (**b**) induced cell permeabilization and disruption of the cell membrane potential caused by RONS within PAW reacting with the lipid bilayer; (**c**) the buildup of intracellular reactive oxygen species (ROS) and a reduction in intracellular pH; (**d**) DNA damage, accompanied by physiological dysfunctions resulting from the disruption of intracellular redox balance and pH homeostasis.

Despite recent advancements in PAW production technologies, several important factors still need further exploration. The effectiveness of PAW inactivation varies depending on how it is generated, and its ability to inactivate a broader range of microorganisms requires evaluation. Additionally, understanding the impact of storage stability on PAW, both in terms of its inactivation properties and physicochemical characteristics, is essential. To address these knowledge gaps, the current research focused on six representative bacterial species: *Escherichia coli* (nontoxigenic O157:H7), *Pseudomonas aeruginosa*, *Salmonella enteritidis*, *Listeria monocytogenes*, *Bacillus cereus*, and *Staphylococcus aureus*. This study investigated PAW's effectiveness in inactivating these bacteria when they are in a planktonic state. The reduction in microbial populations is described using a first-order model to explain the kinetics of microbial inactivation. Additionally, scanning electron microscope (SEM) images were taken to examine any changes in cell morphology following PAW treatment. The study also measured the concentrations of key stable reactive species (H_2O_2, NO_2^-, NO_3^-), pH, and conductivity. Furthermore, the degradation of PAW was monitored over a 40-day period.

2. Materials and Methods

2.1. Generation of Plasma-Activated Water

In this study, two types of PAW produced by two distinct plasma reactors were employed. With the first plasma reactor, an atmospheric pressure plasma jet (CAPP) [34], reactive species were produced in the plasma jet placed above the liquid surface. The second plasma reactor is a hybrid plasma reactor which combines plasma discharge in water and in the gas phase.

2.1.1. Atmospheric Pressure Plasma Jet

The plasma jet in a single-electrode configuration (Figure 2a) [35] used in this study was made of a quartz capillary with an inner diameter of 1 mm and outer diameter of 1.5 mm, as in the study by Gierczik et al. (2020) [36]. Inside the capillary, a 100 µm copper wire was placed and connected to the power supply. The capillary and the wire were both inserted into a Teflon body and connected to a gas tank via a mass flow controller (Alicat MC-5SLPM/D; Alicat Scientific, Tucson, AZ, USA). PAW was made using the 28 kHz frequency, 12 kV_{pp}, and N_2 gas (Messer 99.996% purity). The flow rate of the gas in the experiment was constant and set to 0.5 slm (standard liters per minute). The distilled water (Aqua Purificata GRAM MOL; Zagreb, Croatia) with an initial conductivity of 1.285 $\mu S\ cm^{-1}$ and pH = 7.13 was placed below the nozzle of the plasma jet. A thin plasma channel was formed between the electrode tip and the surface of the water. The gap between the plasma jet and the water was set to 5 mm, ensuring the production of high concentrations of reactive species in PAW. A distance of 5 mm was chosen to maximize the peroxide concentration [10]. The total volume of treated water was 215 mL, and the treatment time was 40 min [37]. The total volume of the water was split into two samples, 200 mL for the bacteria treatment and 15 mL for the PAW aging measurements. To preserve the concentrations of active species in the PAW, five metal magnesium pieces (15 mm in diameter each and a total mass of 2.15 g) were placed on the bottom of the glass beaker [38]. One hour after plasma treatment, the Mg plates were removed from the PAW, and the produced PAW was stored in a fridge at 5 °C. The total input power of the plasma jet was 2.7 W and the dissipated energy was 34.8 kJ/L [36]. During the treatment, the applied voltage was monitored with an HV probe (Tektronix P6015A; Beaverton, OR, USA) and oscilloscope (Hameg-instruments, Combiscope; Mainhausen, Germany), as well as emission spectra using an Avantes spectrometer (AvaSpec-ULS-RS-TEC; Apeldoorn, The Netherlands). The label for PAW produced using the plasma jet was PAW-Jet.

2.1.2. Hybrid Plasma Reactor

A HVG60/1 PL (Impel d.o.o., Zagreb, Croatia) instrument was used for plasma treatment. The experimental setup of the hybrid plasma reactor is shown in Figure 2b. The reactor consists of a glass vessel (1000 mL) and two electrodes. The electrode configuration is the so-called pin-to-pin electrode configuration. The lower high-voltage electrode (medical needle) was placed beneath the water surface. Through the high-voltage electrode, argon gas was blowing with a flow rate of 0.5 slm, making argon bubbles in the water. The second electrode is grounded and made of stainless steel. The grounded electrode was placed above the water surface. The electrode gap between the high-voltage and grounded electrodes was 3 cm. The voltage was adjusted to 40 kV, with a frequency of 90 Hz. The input power used for treatment was 10.8 W and the total energy consumed per treatment amounted to 10.8 kJ/L [36]. The same amount of distilled water was used (215 mL) and was also split into two samples of 200 mL and 15 mL for the PAW aging measurements. The treatment time was 15 min. The label for PAW produced using the hybrid plasma was PAW-Hybrid.

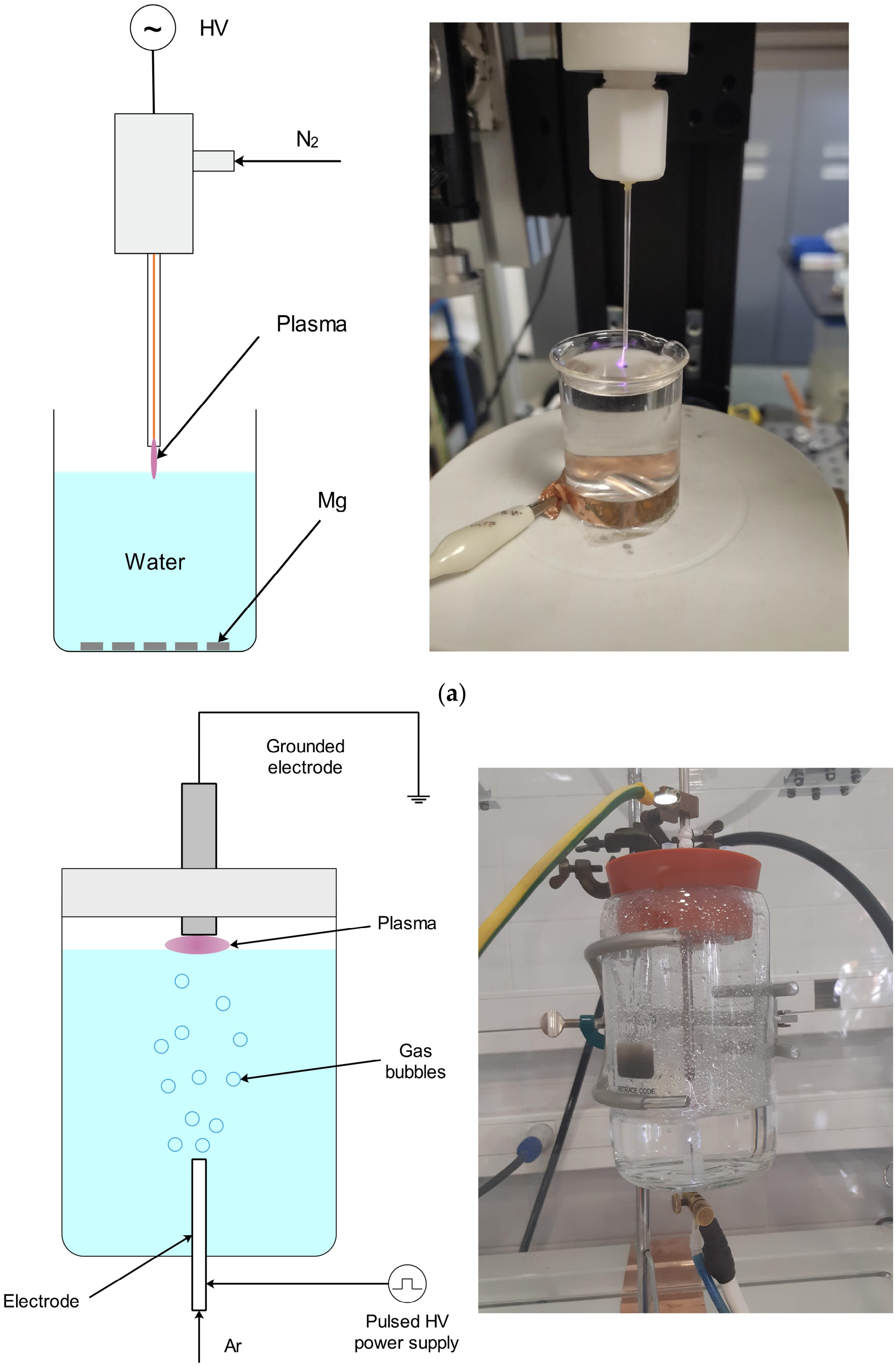

(**a**)

(**b**)

Figure 2. Schematics of the two experimental setups for PAW production: (**a**) plasma jet; (**b**) hybrid plasma reactor.

2.2. Physicochemical Properties of PAW

The reactive oxygen and nitrogen species (RONS) are generated in the gas phase and at the boundary between plasma and liquid, and captured by the liquid in the process of PAW production. The primary reactive species formed in plasma, such as hydroxyl radicals ($^{\bullet}OH$), superoxide radicals ($^{\bullet}O_2^-$), nitrate radicals ($^{\bullet}NO_3^-$), various ions (H^+, OH^+, H_3O^+, O^+, O_2^+, N^+, N_2^+, Ar^+, ArH^+), and water clusters can, through reactions, form secondary reactive and more stable molecules, such as hydrogen peroxide (H_2O_2), ozone (O_3), and other reactive species [39–42]. The mixture of these reactive species makes PAW a highly oxidative environment that can contribute to the inactivation of microorganisms by damaging their cellular components, including lipids, proteins, and nucleic acids. The disruption of these vital components hinders the microorganisms' growth and leads to their destruction.

Plasma-activated water was characterized by determining the chemical composition, conductivity, and pH value. The majority of reactive species are created in the plasma and can interact with water, changing its physical and chemical properties. In this experiment, the concentrations of H_2O_2, NO_2^-, and NO_3^-, and the pH of the samples were measured via a semi-quantitative method (measurement accuracy $\leq$ 10%) using QUANTOFIX® test strips, and the values were read using a QUANTOFIX® Relax unit (Macherey-Nagel, Düren, Germany). With the strips and reader, we were able to measure the PAW parameters with a sufficient temporal resolution during plasma treatment for the plasma jet. We also measured the degradation of PAW in time for 40 days. Using a Metrohm 914 pH/DO/Conductometer, the pH and conductivity of the distilled water before and after treatment were measured.

Inductively coupled plasma–mass spectrometry (ICP-MS) was employed to quantitatively determine the metal ion concentrations in accordance with EPA 6020A: standard [43]. The measurements were conducted using an ICP/MS instrument (PerkinElmer, Inc., Waltham, MA, USA).

2.3. Planktonic Bacterial Suspension Preparation of Gram-Positive and Gram-Negative Bacteria

Three Gram-negative bacterial strains, *Escherichia coli* ATCC 700728 (nontoxigenic O157:H7), *Pseudomonas aeruginosa* ATCC 9027, and *Salmonella enteritidis* ATCC 13076, and three Gram-positive bacterial strains, *Listeria monocytogenes* ATCC 19112, *Bacillus cereus* ATCC 11778, *Staphylococcus aureus* ATCC 6538, were selected as the representative microorganisms. Bacterial pure culture (KWIK-STIK unit) was obtained from the strain collection of Microbiologics, Inc. (St. Cloud, MN, USA). Each KWIK-STIK unit contained a lyophilized microorganism pellet, an ampoule of hydrating fluid, and an inoculating swab and was stored at 2 to 8 °C. One inoculating swab was streaked on tryptic soy agar (TSA; Merck KGaA, Darmstadt, Germany) and incubated for 24 h to obtain isolated colonies. The incubation temperature for all six microorganisms was 35 °C. The early stationary phase of each bacterium was reached by inoculation of a single colony in tryptic soy broth and incubation at 37 °C for 18 h. The bacterial suspensions were diluted by a factor of ten in a maximum recovery diluent (MRD; Sigma-Aldrich Co. LLC, St. Louis, MO, USA) and centrifuged at $6000\times\ g$ for 10 min. The obtained cell pellets were rinsed using sterile phosphate-buffered saline (PBS; Sigma-Aldrich Co. LLC, St. Louis, MO, USA). They were then resuspended and stored at 4 °C for later inactivation analysis, all carried out on the same day. The concentration of the bacterial suspension at the end was around 9 $\log_{10}$ CFU per mL, which was enumerated on TSA plates.

2.4. Influence of Different Exposure Times

A 1 mL aliquot of the washed bacterial suspension was introduced into 9 mL of PAW, which had been stored at 5 °C for five days. The mixture was thoroughly vortexed and then left at room temperature. To assess the influence of varying exposure durations of bacteria to PAW, time intervals of 0.5, 1, 3, 5, 10, and 24 h were chosen to measure the viable counts. For each bacterial species, a control experiment was set up in which 1 mL of the rinsed bacterial suspension was introduced into 9 mL of sterile deionized water, with no exposure to plasma treatment. These inactivation processes were individually replicated three times for each treatment.

2.5. Microbiological Analysis

To assess the effectiveness of PAW inactivation, 1 mL of treated samples was serially diluted in maximum recovery diluent (MRD; Sigma-Aldrich Co. LLC, St. Louis, MO, USA).

Using a sterile micropipette, 1 mL aliquots of appropriate dilutions were transferred to a sterile Petri dish and poured with approximately 20 mL of the tryptic soy agar (TSA; Merck KGaA, Darmstadt, Germany), previously cooled at 44 to 47 °C in a water bath. For *E. coli*, *L. monocytogenes*, *S. aureus*, *S. enteritidis*, and *P. aeruginosa*, the incubation temperature was maintained at 37 ± 1 °C, while for *B. cereus*, it was set to 30 ± 1 °C. The plates were incubated for 24 h, and the CFU was counted. The limit of detection was 1 log CFU mL^{-1}. The outcomes were presented as $\log_{10}$ colony-forming units (CFU) per milliliter (mL), and the effectiveness of PAW in inactivating microorganisms was computed using the following equation:

$$\text{Log}_{10}\ \text{reduction} = \text{Log}_{10}\ (\text{CFU}_{\text{Control}}) - \text{Log}_{10}\ (\text{CFU}_{\text{Treated}}) \tag{1}$$

2.6. Scanning Electron Microscope (SEM) Imaging

The morphological changes in cell structure were examined using scanning electron microscopy analysis with and without both PAW treatments. Based on the 5 days storage of PAW, cell cultures were examined after mixing with PAW after 24 h of exposure at room temperature. Samples were prepared using the method described by Zhao et al. (2020) [20]. Following centrifugation at 6000× *g* for 10 min at 4 °C, the supernatants were removed, and the resulting cell pellets were resuspended in 500 µL of a 25% glutaraldehyde (GA) solution. To ensure proper fixation, the samples were refrigerated at 4 °C overnight. The following day, the cells were centrifuged and resuspended in PBS. This process was repeated three times to eliminate GA. Subsequently, 10 µL of the solution was dispensed onto a sterilized slide and air-dried in a fume hood for 10–15 min. These slides were then placed into 12-well plates for dehydration using a sequence of increasing ethanol concentrations (50%, 60%, 70%, 80%, 90%, and 100%). The dehydration time for ethanol concentrations between 50% and 90% was set to 5 min, while for 100% ethanol, it was 15 min. As for the drying procedure, the slides were submerged in hexamethyldisilizane (HMDS) at concentrations of 33%, 50%, 66%, and 100%, successively. Afterward, they were stored at 4 °C in a dark environment overnight before being subjected to SEM analysis. The desiccated samples were subjected to gold coating using a Sputter Coater SCD 005, BALTEC SCAN, with a working distance (WD) of 50 mm, for a duration of 90 s at a current of 30 mA. Subsequently, they were examined via scanning electron microscopy using a JMS SEM 6460 LV, operating at an acceleration voltage of 25 kV, and varying the WD from 20 to 8 mm.

2.7. PAW Microbial Inactivation Kinetics

In this investigation, the PAW microbial inactivation curves were determined by the first-order kinetics [44]. The experimental data take the shape of an exponential decay curve model and could be represented using Equation (2).

$$y(t) = y_0 e^{-k\,t} \tag{2}$$

The number of viable cells ($y(t)$) during contact time with the PAW were output values, while the only fitted coefficient (k) was the inactivation rate of the microbial population. That is the slope of the survivors' viable cells versus time for the microbial population. The coefficient y_0 represents the initial value of the microbial cells before PAW treatment, and it is fixed.

The suitability of the constructed models was assessed by employing the coefficient of determination (COD) and reduced *chi-square* (χ^2). These frequently employed parameters can be computed in the following manner:

$$chi - square = \sum_{i=1}^{N} \frac{y_{exp,i} - y_{pre,i}}{N - n} \tag{3}$$

In this equation, $y_{exp,i}$ represents the experimental values, while $y_{pre,i}$ corresponds to the predicted values derived from the model (Equation (3)) for these specific measurements. N and n denote the number of observations and the number of constants, respectively. Furthermore, a 95% predicting band interval was used to represent uncertainty and noise in the predicting model values. The relative average error between the measurements was up to 5%.

3. Results

3.1. Inactivation Efficacy of PAW

The influence of the PAW-Jet and PAW-Hybrid treatments on the microbial cells is presented in Table 1. The effectiveness of the PAW treatments was observed through Log_{10} reduction using Equation (1). A wide range of initial microbial concentrations (from 10^7 to 10^9) was used in this study (Tables 2 and 3) with the aim of investigating PAW inactivation. The inactivation kinetics were described by a first-order model and the only fitted parameter was constant rate, which shows the rate of reduction in the microbial populations. Tables 2 and 3 show that PAW treatment was most effective for *Escherichia coli* O157:H7, with $k = 7.168$ and $k = 6.954$ obtained for the hybrid plasma reactor and electrode plasma jet, respectively. On the other hand, the microbial inactivation was slowest during the PAW treatment for *Bacillus cereus*, with $k = 3.072$ and $k = 3.792$ obtained for the hybrid plasma reactor and electrode plasma jet, respectively.

Table 1. Log viable counts of the bacterial species after different exposure times with PAWs.

Bacteria	Exposure Time (h)	NT	PAW-Jet	Log_{10} Reduction	PAW-Hybrid	Log_{10} Reduction
Listeria monocytogenes	0	9.28 ± 0.01	9.28 ± 0.01	0.00	9.28 ± 0.01	0.00
	0.5		8.29 ± 0.01	0.99	8.31 ± 0.00	0.97
	1		8.21 ± 0.02	1.07	8.23 ± 0.04	1.05
	3		8.15 ± 0.02	1.13	8.10 ± 0.03	1.18
	5		8.07 ± 0.01	1.21	8.00 ± 0.01	1.28
	10		7.17 ± 0.02	2.11	6.65 ± 0.03	2.63
	24		4.09 ± 0.13	5.19	3.88 ± 0.05	5.40
Escherichia coli O157:H7	0	9.34 ± 0.04	9.34 ± 0.04	0.00	9.34 ± 0.04	0.00
	0.5		7.82 ± 0.07	1.52	7.78 ± 0.08	1.56
	1		7.81 ± 0.03	1.53	7.66 ± 0.03	1.68
	3		7.61 ± 0.03	1.73	7.45 ± 0.04	1.89
	5		7.43 ± 0.08	1.91	7.27 ± 0.03	2.07
	10		6.11 ± 0.04	3.23	6.16 ± 0.02	3.18
	24		3.54 ± 0.06	5.80	3.63 ± 0.11	5.65
Salmonella enteritidis	0	9.16 ± 0.03	9.15 ± 0.06	0.01	9.15 ± 0.06	0.01
	0.5		8.04 ± 0.02	1.12	8.01 ± 0.01	1.15
	1		7.98 ± 0.02	1.18	7.99 ± 0.02	1.17
	3		7.82 ± 0.05	1.34	7.82 ± 0.05	1.34
	5		7.66 ± 0.04	1.50	7.09 ± 0.05	2.07
	10		6.24 ± 0.03	2.92	6.14 ± 0.01	3.02
	24		4.15 ± 0.03	5.01	3.90 ± 0.04	5.26
Staphylococcus aureus	0	8.71 ± 0.03	8.71 ± 0.03	0.00	8.71 ± 0.03	0.00
	0.5		7.68 ± 0.00	1.03	7.65 ± 0.02	1.06
	1		7.52 ± 0.06	1.19	7.50 ± 0.02	1.21
	3		7.42 ± 0.06	1.29	7.40 ± 0.07	1.31
	5		7.16 ± 0.03	1.55	7.11 ± 0.02	1.60
	10		5.90 ± 0.04	2.81	6.00 ± 0.03	2.71
	24		3.67 ± 0.03	5.04	3.71 ± 0.11	5.00
Pseudomonas aeruginosa	0	8.62 ± 0.02	8.62 ± 0.03	0.00	8.62 ± 0.03	0.00
	0.5		7.44 ± 0.06	1.18	7.62 ± 0.02	1.00
	1		7.38 ± 0.08	1.24	7.49 ± 0.04	1.13
	3		7.00 ± 0.01	1.62	7.35 ± 0.04	1.27
	5		6.80 ± 0.06	1.82	6.07 ± 0.03	2.55
	10		6.26 ± 0.04	2.36	5.71 ± 0.02	2.91
	24		3.59 ± 0.05	5.03	3.55 ± 0.05	5.07
Bacillus cereus	0	7.42 ± 0.03	7.42 ± 0.03	0.00	7.42 ± 0.03	0.00
	0.5		6.55 ± 0.09	0.87	6.73 ± 0.07	0.69
	1		6.34 ± 0.02	1.08	6.31 ± 0.02	1.11
	3		6.11 ± 0.03	1.31	6.12 ± 0.02	1.30
	5		5.65 ± 0.10	1.77	5.58 ± 0.03	1.77
	10		4.52 ± 0.07	2.90	5.21 ± 0.04	2.21
	24		3.15 ± 0.08	4.27	2.80 ± 0.05	4.62

NT: non-treated (control); the results are presented as mean ± standard deviation of 3 measurements.

Table 2. Summary of kinetic coefficients with statistics, which explain the trends of the examined PAW-Jet.

PAW-Jet	***Listeria monocytogenes***	***Escherichia coli* O157:H7**	***Salmonella enteritidis***	***Staphylococcus aureus***	***Pseudomonas aeruginosa***	***Bacillus cereus***
Y_0	1.92×10^9	2.28×10^9	1.40×10^9	5.27×10^8	4.18×10^8	2.68×10^7
k	-4.3 ± 0.8	-6.9 ± 0.9	-4.8 ± 0.8	-4.6 ± 0.6	-5.3 ± 0.5	-3.8 ± 0.4
Reduced Chi-Sqr	8.92×10^{15}	1.04×10^{15}	2.32×10^{15}	2.78×10^{14}	5.37×10^{13}	7.73×10^{11}
R-Square (COD)	0.98	0.99	0.99	0.99	0.99	0.99

Table 3. Summary of kinetic coefficients with statistics, which explain the trends of the examined PAW-Hybrid.

PAW-Hybrid	***Listeria monocytogenes***	***Escherichia coli* O157:H7**	***Salmonella enteritidis***	***Staphylococcus aureus***	***Pseudomonas aeruginosa***	***Bacillus cereus***
Y_0	1.92×10^9	2.28×10^9	1.40×10^9	5.27×10^8	4.18×10^8	2.68×10^7
k	-4.2 ± 0.7	-7.2 ± 0.7	-4.8 ± 0.7	-4.6 ± 0.6	-4.4 ± 0.6	-3.1 ± 0.2
Reduced Chi-Sqr	7.43×10^{15}	5.17×10^{14}	2.07×10^{15}	2.78×10^{14}	2.00×10^{14}	4.44×10^{11}
R-Square (COD)	0.98	0.99	0.99	0.99	0.99	0.99

The comparison between the experimental measurements and the results calculated by the model is provided in Tables 2 and 3. The quality of the model fit was assessed, and the results of residual analysis for the developed model are presented in these tables. The one-parameter first-order mathematical model presented for predicting PAW values during the storage period is characterized as simple, robust, and accurate, with all coefficients of determination exceeding 0.981. Moreover, the mathematical models for each bacterial species exhibited no significant lack of fit, indicating that all the models effectively represented the data. The high coefficient of determination (COD) indicates that the model accounted for the variations in the data and that the data fit well with the proposed model.

3.2. Scanning Electron Microscopy Images

The effects of PAW treatment on six representative bacteria and control using SEM are shown in Figure 3. The control samples without PAW treatment had smooth and intact bacterial surfaces (Figure 3A–F). Different types of morphological changes and damage, irrespective of the PAW generation method, were observed subsequent to the treatment with PAW (Figure 3G–L; Figure 3M–R, including distortion and holes on the cell surface, deformation, rupture of the outer layer, surface roughness, and a tendency to crack.

3.3. Physicochemical Properties and Aging of PAW

pH, conductivity, and concentrations of hydrogen peroxide H_2O_2, nitrites (NO_2^-), and nitrates (NO_3^-) were monitored for 40 days from the PAW production. The PAW application on the bacteria was on the fifth day after production. The evolution of the PAW is presented in Figure 4. Non-monotonic changes in the concentration of nitrite anions, hydrogen peroxide, and pH values are a consequence of measurement accuracy $\leq$ 10%. We used Mg plates immersed in the water sample during the treatment to stabilize the concentrations of active species and prolong the antibacterial properties of the PAW. Table 4 displays the concentrations of metal ions in the water samples following plasma treatment for PAW-Jet and PAW-Hybrid. It can be seen that the concentrations of the metals for PAW-Hybrid are significantly higher than for PAW-Jet mainly because the metal electrode for the hybrid plasma reactor is immersed in water and can release metal ions during PAW production. The sources of the Mg^{2+} ions in PAW-Jet are the Mg plates that are used for PAW stabilization to prolong its efficiency. The concentration of the Mg^{2+} ions in PAW-Jet is more than three times (3.36×) higher than in the PAW-Hybrid sample.

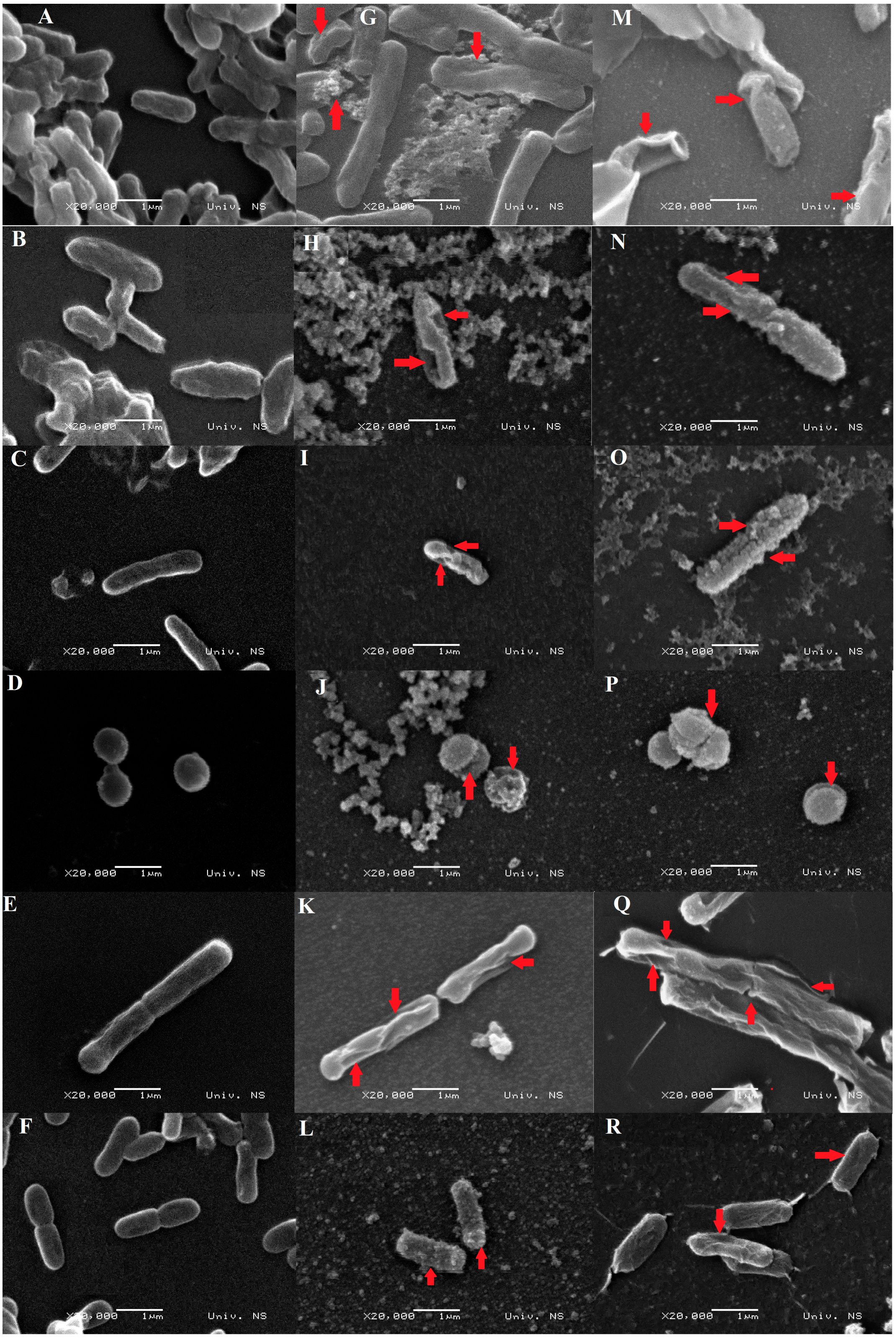

Figure 3. Scanning electron microscopy (SEM) images of the representative bacterial species from the control and both generation-method PAW treatments. (**A**–**F**) are the non-treated *Escherichia coli* (nontoxigenic O157:H7), *Salmonella enteritidis*, *Pseudomonas aeruginosa*, *Staphylococcus aureus*, *Bacillus cereus*, and *Listeria monocytogenes*, respectively; (**G**–**L**) are the corresponding bacteria treated with PAW-Jet and (**M**–**R**) are the corresponding bacteria treated with PAW-Hybrid. The damage to the cells is indicated by red arrows.

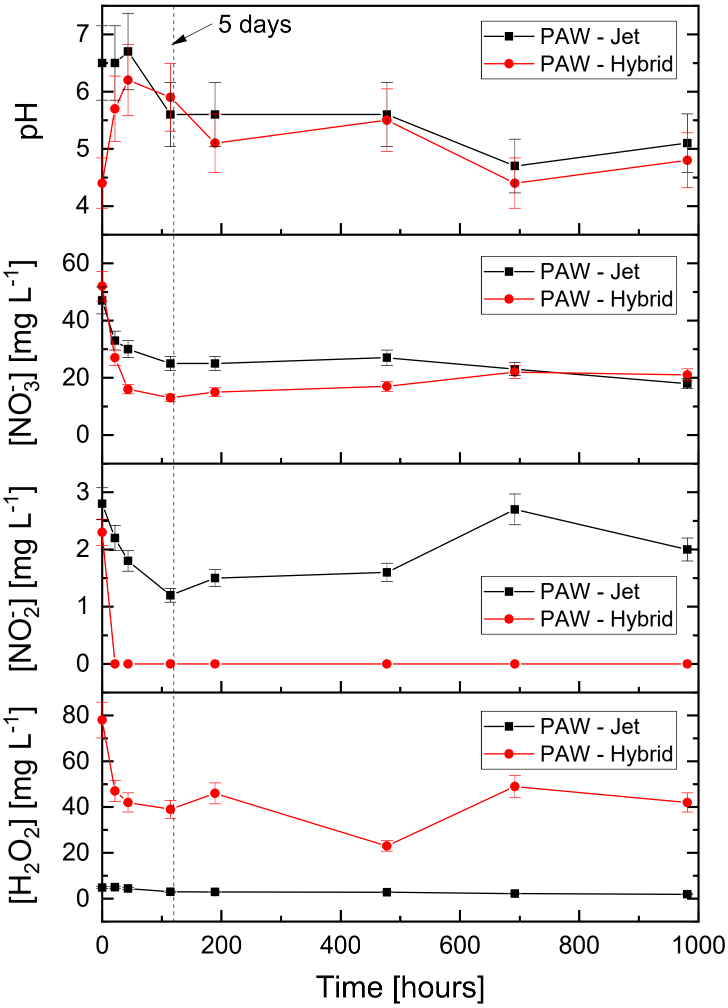

Figure 4. Aging of the PAW produced by two plasma sources, plasma jet and hybrid plasma reactor.

Table 4. The concentrations of metal ions in the water samples after plasma treatment.

Element (µg/L)	PAW-Jet	PAW-Hybrid
Ni	<1	87.9 ± 0.7
Pb	3.637 ± 0.009	4.21 ± 0.04
Fe	39.3 ± 0.9	429 ± 3
Sn	2.48 ± 0.07	1.0 ± 0.4
Na	1326 ± 7	1345 ± 12
Hg	<1	<1
Mn	<1	14.9 ± 0.4
Ca	1160 ± 34	3093 ± 13
B	10.9 ± 0.3	81.50 ± 0.06
Al	93.5 ± 0.5	30 ± 1
Se	NQ	<1
Ba	6.73 ± 0.03	8.2 ± 0.05
Mg	1882 ± 5	559 ± 4
Mo	<1	3.9 ± 0.4
As	91.2 ± 0.2	73.6 ± 0.5
K	5299 ± 4	6383 ± 32
Cr	7.28 ± 0.02	133 ± 6
Cd	<1	<1
Co	<1	2.7 ± 0.2
Zn	51.3 ± 0.3	80.0 ± 0.2
Sb	<1	<1
Cu	5.11 ± 0.09	19.9 ± 0.1
Be	<1	<1

The limit of quantification of the method is 1 µg/L; the results are presented as mean ± standard deviation of 2 measurements.

4. Discussion

The primary objective of this study was to assess the efficiency of PAW in combating six diverse bacterial species in their free-floating planktonic form. The investigation encompassed various factors, such as the use of two distinct plasma reactors, varying exposure durations, and the influence of different bacterial species on the inactivation capacity of PAW.

The findings indicated that longer plasma treatment and exposure times tended to enhance the inactivation efficacy. This was attributed to the fact that prolonged plasma treatment generated more reactive species, and longer exposure times allowed for increased interactions between these reactive species and the bacterial cells. To gain a deeper understanding of the inactivation mechanisms of PAW, SEM images of bacterial species were taken and an analysis of the physicochemical properties of PAW was conducted.

Depending on the chemical conditions, applied voltage, and the mode of generation, various reactive oxygen species (ROS) and reactive nitrogen species (RNS) may be produced. These combined ROS and RNS species, collectively referred to as RONS, are generated in plasma-activated water (PAW) and play a pivotal role in microbial inactivation. The production of these chemical species within PAW highlights the synergistic impact of high oxidation-reduction potential (ORP) and low pH, which exhibit antimicrobial properties [14]. The treatment of water with plasma caused a nonequilibrium dissociation of water molecules, resulting in the creation of short-lived species like hydroxyl ions (OH−) and solvated (hydrated) electrons (e_{solv}) [45,46]. The relevant reactions are as follows:

$$H_2O + e^- \rightarrow OH^\bullet + H^\bullet + e^- \quad (4)$$

$$H_2O + e^- \rightarrow OH^\bullet + H^+ + 2e^- \quad (5)$$

$$OH^\bullet + OH^\bullet \rightarrow H_2\,O_2 \quad (6)$$

$$H^\bullet + O_2 \rightarrow HO_2{}^\bullet \quad (7)$$

$$OH^- + H_2\,O_2 \rightarrow OOH^- + H_2O \quad (8)$$

$$*OOH \rightarrow * + O_2 + H^+ + e^- \quad (9)$$

where $*$ represents the active site of the catalyst

$$O_2 + e^- \rightarrow O^+ + O^\bullet + 2e^- \quad (10)$$

$$O_2 + O^\bullet \rightarrow O_3 \quad (11)$$

Regarding the mechanism by which ROS contribute to microbial inactivation, H_2O_2, hydroxyl ions ($^\bullet OH$), and ozone (O_3) are chemical species recognized as highly effective antimicrobial agents. It is well established that the hydroxyl radical ($^\bullet OH$) stands out as one of the most potent oxidizing agents within the category of oxygen-based oxidizers. It exhibits a notable ability to readily target unsaturated fatty acids on the cell membrane, and it can disrupt intracellular materials such as DNA [47–49]. The $^\bullet OH$ radicals initiate the process of lipid peroxidation by extracting hydrogen atoms from the unsaturated carbon bonds in fatty acids, resulting in the generation of malondialdehyde (MDA) as the ultimate product [50]. MDA serves as a commonly used marker for assessing lipid oxidation. Both $^\bullet OH$ and H_2O_2 possess the capability to disrupt the intramolecular bonds within peptidoglycan, potentially resulting in the breakdown of the cell wall. $^\bullet OH$ achieves this by extracting a hydrogen atom from the alpha carbon of the peptide bonds (-CO-NH-) in the peptidoglycan structure, which is linked to amino acids. Additionally, it is worth noting that the transport of ROS from PAW into microbial cells can cause internal damage by breaking down DNA, and the degradation of proteins and various internal cellular components [51].

As far as the RNS mechanism of microbial inactivation is concerned, the primary influence on microbial susceptibility is the reduction in the pH in PAW. The formation of compounds like HNO_3, HNO_2, and HNOOH within PAW leads to acidification, which is responsible for microbial inactivation. Peroxynitrite ions, also formed in PAW, play a pivotal role as potent oxidizers in reactions contributing to microbial inactivation. In the presence of air, the nitrogen and oxygen from the gaseous phase undergo dissociation to generate nitrogen oxide (NO), which then interacts with water to form acidic compounds. This process leads to a decrease in pH, creating an acidic environment. The rapid decrease in pH speeds up the process of nitrite disproportionation or the breakdown of nitrite into nitrates, along with the reaction of H_2O_2 with nitrites to form $ONOO^-$s [22,52]. Some of these reactions are as follows:

$$NO_2{}^- + H^+ \rightarrow HNO_2 \tag{12}$$

$$NO_2{}^\bullet + OH^\bullet \rightarrow HNO_3 \tag{13}$$

$$2HNO_2 \rightarrow NO^\bullet + NO_2{}^\bullet + H_2O \tag{14}$$

$$2NO_2 + H_2O \rightarrow NO_3{}^- + NO_2{}^- + 2H^+ \tag{15}$$

$$NO_2{}^- + H_2O_2 + H^+ \rightarrow ONOOH + H_2O \tag{16}$$

$$ONOOH \rightarrow NO_2{}^\bullet + OH^\bullet \tag{17}$$

$$ONOOH \rightarrow HNO_3 \rightarrow NO_3{}^- + H^+ \tag{18}$$

When it comes to the resistance of the used reference strains, our findings indicated that Gram-positive bacteria exhibited greater resistance to PAW-Jet and PAW-Hybrid than Gram-negative species, with the lowest reductions observed for *B. cereus* compared with the other two Gram-positive bacteria under identical conditions. Between the other two Gram-positive bacteria examined, *S. aureus* showed much more resistance to PAW than *L. monocytogenes.* The varying responses could be partly attributed to the bacteria's morphology. An inactivation study conducted by Arroyo et al. in 1999 [53] indicated that cocci-shaped bacteria are typically more challenging to deactivate in comparison to rod-shaped bacteria. This heightened difficulty in inactivation can be attributed to the spherical shape, which results in reduced surface area in contact with the surrounding medium. Concerning the results of the reduction in Gram-negative species in both treatments, PAW-Jet and PAW-Hybrid, the least resistance was shown by *Escherichia coli* O157:H7. Other plasma inactivation studies [12,39,53–58] are in accordance with our findings. The structural variances in the bacterial cell wall are responsible for this phenomenon. The Gram-positive bacteria have a thicker cell wall, measuring between 20 and 80 nm, compared to Gram-negative bacteria, which typically have a cell wall thickness ranging from 10 to 15 nm. Consequently, this increased thickness results in greater structural rigidity and enhanced protection for bacterial cells against the reactive species formed in PAW [53].

In an attempt to explore alterations in the morphological structure of bacteria after PAW treatment, a scanning electron microscope (SEM) was employed. The SEM provided a visual confirmation of alterations in cell structure following the application of PAW treatment. In the control group, the bacterial surface appeared smooth and remained undamaged. However, following PAW treatment, various morphological changes and signs of damage were evident. All tested bacterial cells underwent a transition toward a tendency to crack. Most of the *S. enteritidis* and *P. aeruginosa* cells had holes on the cell surface and some distortion. The rupture of the outer layer was clearly seen in *B. cereus* and *E. coli*. Deformation or shrinkage was present in *S. aureus* and surface roughness in *L. monocytogenes*. Similar to our research, numerous studies have illustrated alterations in bacterial morphology through SEM images following exposure to PAW treatment [18,20,54,56,59–61]. The images also depicted that PAW inflicted damage to the bacterial cell wall and internal structure, suggesting the potent bactericidal capabilities of PAW.

The process of PAW aging can be affected by elements such as temperature, the material of the container, and its exposure to light and air. Over time, the concentration of RONS, such as hydrogen peroxide (H_2O_2), ozone (O_3), and nitric oxide (NO), gradually decreases as these reactive species react with each other, with gas over the liquid and with the water matrix. Consequently, the oxidation-reduction potential (ORP) of PAW tends to decrease, and its pH can shift towards neutrality. As the PAW ages, it becomes less effective for certain applications that rely on high RONS concentrations. To extend the shelf life of PAW and maintain its efficacy, storage conditions and container materials are carefully considered. Dark, airtight containers at a low temperature of 5 °C are used to slow down the aging process and preserve the PAW's reactivity. Shen et al. (2016) [18] observed properties of PAW stored at different temperatures and reported that bactericidal ability increased with decreasing temperature, and that PAW should be stored at −80 °C to preserve its antibacterial characteristics. Instead of freezing PAW, we opted for the introduction of Mg discs to supply Mg^{2+} ions. This choice was made because it effectively prevents a significant drop in pH value, which in turn helps stabilize the concentration and mitigate the intense reactivity of the reactive species [62]. With this method, we have the ability to significantly prolong the lifespan of the PAW, allowing us to detect species after storing it for up to 40 days. In Figure 4, we presented the PAW aging process over a period of 40 days when stored in air flasks at a temperature of 5 °C, in a dark environment. The volume of the stored PAW was 15 mL in both cases (jet and hybrid). As we can see from the graphs, slow decay of the reactive species in the aging process is observed. The pH value before treatment was pH = 7.13; after treatment, it dropped to 6, and during the aging, the pH value was in the range from 5 to 6. The pH values for the samples without the Mg plates were slightly lower, in the range of 4–5. Changes in the pH value of the PAW are due to the dissolving of the stable molecules formed in plasma in water. The concentration of H_2O_2 is stable during the aging process. For PAW-Hybrid, the concentration of the H_2O_2 was 58 mg/mL compared to 5 mg/mL for PAW-Jet. On the day of application of the PAW, the concentrations were 42 and 3 mg/mL, respectively, for PAW-Hybrid and PAW-Jet. The concentration of nitrites is very sensitive to aging and diminishes very fast for lower pH values and higher H_2O_2 values. For example, for PAW-Hybrid, nitrites were already at zero a few hours after treatment, but for PAW-Jet, with lower starting values for H_2O_2 and larger pH values, due to the use of Mg^{2+} ions, nitrite concentrations could be preserved at about 1.5 mg/L for days. The concentrations of nitrates are similar, about 15 mg/L for both plasma reactors. Nitrates and nitrites are long-lived species that are secondary products in PAW formation. Nitrite can easily be transformed into H_2N_2 in a low-pH environment. The conductivity of the water before plasma treatment was 1.285 $\mu S\ cm^{-1}$ and after treatment rose to 43.5 $\mu S\ cm^{-1}$ for the hybrid plasma reactor and 31.49 $\mu S\ cm^{-1}$ for the plasma jet. During the aging of the PAW, the conductivity increased to about 54 $\mu S\ cm^{-1}$ after 16 days.

5. Conclusions

This study involved the selection of six representative bacterial species to assess the impact of variables such as plasma treatment time, exposure time, and bacterial species on the inactivation efficacy of PAW, with additional investigation of the bacterial inactivation mechanisms of PAW. The results demonstrated the notable antimicrobial properties of PAW, with the Gram-negative bacteria included in our study proving to be more susceptible to PAW than the Gram-positive species. Among the species examined, *B. cereus* was identified as the most resistant to PAW treatment. SEM images provided visual evidence of cell morphological damage resulting from PAW treatment. Additionally, an analysis of the physicochemical properties of PAW, including parameters such as pH, conductivity, and the presence of long-lasting reactive species like H_2O_2, NO_2^-, and NO_3^-, contributed to a more comprehensive understanding of the mechanisms involved in PAW-mediated inactivation.

Overall, this research highlights PAW as a promising disinfectant with significant potential applications within the food industry.

Author Contributions: Conceptualization, R.Č., B.K. and I.Č.; methodology, R.Č., D.M., I.Č., V.S., S.M. and T.V.P.; software, P.K. and M.V.; formal analysis, R.Č. and D.M.; investigation, R.Č., D.M., V.S., S.M. and T.V.P.; resources, R.Č., S.M., V.S. and T.V.P.; data curation, R.Č., D.M. and S.M.; writing—original draft preparation, R.Č. and D.M.; writing—review and editing, R.Č., S.K.-T., D.M., S.M., I.Č., M.V., V.S., T.V.P., P.K. and B.K.; visualization, R.Č.; supervision, S.M. All authors have read and agreed to the published version of the manuscript.

Funding: This article is based upon work from COST Action CA19110 PlAgri, supported by COST (European Cooperation in Science and Technology). This work was supported by the project Adaptation of vegetables to new agrometeorological conditions in Slavonia (AVACS), KK.05.1.1.02.0004. The project was financed by the European Union from the European Regional Development Fund. This work was also supported by the MSTDI Republic of Serbia under grant number 451-03-47/2023-01/200024 and also co-funded by the Republic of Croatia Ministry of Science and Education through the European Regional Development Fund through the project (KK.01.1.1.02.0001) "Equipping the semi-industrial practice for the development of new food technologies".

Data Availability Statement: Data are contained within the article.

Acknowledgments: The authors thank the support from the SP Laboratorija A.D. Bečej.

Conflicts of Interest: The authors declare no conflict of interest.

References

1. Amit, S.K.; Uddin, M.M.; Rahman, R.; Islam, S.M.R.; Khan, M.S. A Review on Mechanisms and Commercial Aspects of Food Preservation and Processing. *Agric. Food Secur.* **2017**, *6*, 51. [CrossRef]
2. Todd, E.C.D. Foodborne Diseases: Overview of Biological Hazards and Foodborne Diseases. In *Encyclopedia of Food Safety*; Elsevier: Amsterdam, The Netherlands, 2014; Volume 1, pp. 221–242. [CrossRef]
3. Augusto, P.E.D. Challenges, Trends and Opportunities in Food Processing. *Curr. Opin. Food Sci.* **2020**, *35*, 72–78. [CrossRef]
4. Hernández-Hernández, H.M.; Moreno-Vilet, L.; Villanueva-Rodríguez, S.J. Current Status of Emerging Food Processing Technologies in Latin America: Novel Non-Thermal Processing. *Innov. Food Sci. Emerg. Technol.* **2019**, *58*, 102233. [CrossRef]
5. Konchekov, E.M.; Gusein-zade, N.; Burmistrov, D.E.; Kolik, L.V.; Dorokhov, A.S.; Izmailov, A.Y.; Shokri, B.; Gudkov, S.V. Advancements in Plasma Agriculture: A Review of Recent Studies. *Int. J. Mol. Sci.* **2023**, *24*, 15093. [CrossRef]
6. Niemira, B.A. Cold Plasma Decontamination of Foods *. *Annu. Rev. Food Sci. Technol.* **2012**, *3*, 125–142. [CrossRef]
7. Misra, N.N.; Schlüter, O.; Cullen, P.J. Plasma in Food and Agriculture. In *Cold Plasma in Food and Agriculture: Fundamentals and Applications*; Elsevier: Amsterdam, The Netherlands, 2016; pp. 1–16. [CrossRef]
8. Thirumdas, R.; Kothakota, A.; Annapure, U.; Siliveru, K.; Blundell, R.; Gatt, R.; Valdramidis, V.P. Plasma Activated Water (PAW): Chemistry, Physico-Chemical Properties, Applications in Food and Agriculture. *Trends Food Sci. Technol.* **2018**, *77*, 21–31. [CrossRef]
9. Ma, R.; Wang, G.; Tian, Y.; Wang, K.; Zhang, J.; Fang, J. Non-Thermal Plasma-Activated Water Inactivation of Food-Borne Pathogen on Fresh Produce. *J. Hazard. Mater.* **2015**, *300*, 643–651. [CrossRef] [PubMed]
10. Kutasi, K.; Popović, D.; Krstulović, N.; Milošević, S. Tuning the Composition of Plasma-Activated Water by a Surface-Wave Microwave Discharge and a KHz Plasma Jet. *Plasma Sources Sci. Technol.* **2019**, *28*, 095010. [CrossRef]
11. Liu, Z.C.; Liu, D.X.; Chen, C.; Li, D.; Yang, A.J.; Rong, M.Z.; Chen, H.L.; Kong, M.G. Physicochemical Processes in the Indirect Interaction between Surface Air Plasma and Deionized Water. *J. Phys. D Appl. Phys.* **2015**, *48*, 495201. [CrossRef]
12. Ostrikov, K.K.; Zhou, R.; Zhou, R.; Wang, P.; Xian, Y.; Mai-Prochnow, A.; Lu, X.; Cullen, P.J.; Ostrikov, K.; Bazaka, K. Plasma-Activated Water: Generation, Origin of Reactive Species and Biological Applications. *J. Phys. D Appl. Physics.* **2020**, *53*, 303001. [CrossRef]
13. Kutasi, K.; Krstulović, N.; Jurov, A.; Salamon, K.; Popović, D.; Milošević, S. Controlling: The Composition of Plasma-Activated Water by Cu Ions. *Plasma Sources Sci. Technol.* **2021**, *30*, 045015. [CrossRef]
14. Zhang, Q.; Ma, R.; Tian, Y.; Su, B.; Wang, K.; Yu, S.; Zhang, J.; Fang, J. Sterilization Efficiency of a Novel Electrochemical Disinfectant against Staphylococcus Aureus. *Environ. Sci. Technol.* **2016**, *50*, 3184–3192. [CrossRef] [PubMed]
15. Kaushik, N.K.; Ghimire, B.; Li, Y.; Adhikari, M.; Veerana, M.; Kaushik, N.; Jha, N.; Adhikari, B.; Lee, S.J.; Masur, K.; et al. Biological and Medical Applications of Plasmaactivated. *Biol. Chem.* **2018**, *400*, 39–62. [CrossRef] [PubMed]
16. Kolb, J.F.; Mohamed, A.A.H.; Price, R.O.; Swanson, R.J.; Bowman, A.; Chiavarini, R.L.; Stacey, M.; Schoenbach, K.H. Cold Atmospheric Pressure Air Plasma Jet for Medical Applications. *Appl. Phys. Lett.* **2008**, *92*, 241501. [CrossRef]
17. Pan, J.; Sun, K.; Liang, Y.; Sun, P.; Yang, X.; Wang, J.; Zhang, J.; Zhu, W.; Fang, J.; Becker, K.H. Cold Plasma Therapy of a Tooth Root Canal Infected with Enterococcus Faecalis Biofilms in Vitro. *J. Endod.* **2013**, *39*, 105–110. [CrossRef]

18. Shen, J.; Tian, Y.; Li, Y.; Ma, R.; Zhang, Q.; Zhang, J.; Fang, J. Bactericidal Effects against S. Aureus and Physicochemical Properties of Plasma Activated Water Stored at Different Temperatures. *Sci. Rep.* **2016**, *6*, 28505. [CrossRef]
19. Wang, Q.; Salvi, D. Evaluation of Plasma-Activated Water (PAW) as a Novel Disinfectant: Effectiveness on *Escherichia coli* and *Listeria innocua*, Physicochemical Properties, and Storage Stability. *LWT* **2021**, *149*, 111847. [CrossRef]
20. Zhao, Y.M.; Ojha, S.; Burgess, C.M.; Sun, D.W.; Tiwari, B.K. Inactivation Efficacy and Mechanisms of Plasma Activated Water on Bacteria in Planktonic State. *J. Appl. Microbiol.* **2020**, *129*, 1248–1260. [CrossRef] [PubMed]
21. Guo, L.; Xu, R.; Gou, L.; Liu, Z.; Zhao, Y.; Liu, D.; Zhang, L.; Chen, H.; Kong, M.G.; Guo, C.L. Mechanism of Virus Inactivation by Cold Atmospheric-Pressure Plasma and Plasma-Activated Water. *Appl. Environ. Microbiol.* **2018**, *84*, 726–744. [CrossRef]
22. Zhao, Y.M.; Patange, A.; Sun, D.W.; Tiwari, B. Plasma-Activated Water: Physicochemical Properties, Microbial Inactivation Mechanisms, Factors Influencing Antimicrobial Effectiveness, and Applications in the Food Industry. *Compr. Rev. Food Sci. Food Saf.* **2020**, *19*, 3951–3979. [CrossRef]
23. Scholtz, V.; Pazlarova, J.; Souskova, H.; Khun, J.; Julak, J. Nonthermal Plasma—A Tool for Decontamination and Disinfection. *Biotechnol. Adv.* **2015**, *33*, 1108–1119. [CrossRef] [PubMed]
24. Chen, C.; Liu, C.; Jiang, A.; Guan, Q.; Sun, X.; Liu, S.; Hao, K.; Hu, W. The Effects of Cold Plasma-Activated Water Treatment on the Microbial Growth and Antioxidant Properties of Fresh-Cut Pears. *Food Bioproc. Tech.* **2019**, *12*, 1842–1851. [CrossRef]
25. Liu, C.; Chen, C.; Jiang, A.; Sun, X.; Guan, Q.; Hu, W. Effects of Plasma-Activated Water on Microbial Growth and Storage Quality of Fresh-Cut Apple. *Innov. Food Sci. Emerg. Technol.* **2020**, *59*, 102256. [CrossRef]
26. Zhao, Y.; Chen, R.; Liu, D.; Wang, W.; Niu, J.; Xia, Y.; Qi, Z.; Zhao, Z.; Song, Y. Effect of Nonthermal Plasma-Activated Water on Quality and Antioxidant Activity of Fresh-Cut Kiwifruit. *IEEE Trans. Plasma Sci.* **2019**, *47*, 4811–4817. [CrossRef]
27. Royintarat, T.; Choi, E.H.; Boonyawan, D.; Seesuriyachan, P.; Wattanutchariya, W. Chemical-Free and Synergistic Interaction of Ultrasound Combined with Plasma-Activated Water (PAW) to Enhance Microbial Inactivation in Chicken Meat and Skin. *Sci. Rep.* **2020**, *10*, 1559. [CrossRef]
28. Liao, X.; Su, Y.; Liu, D.; Chen, S.; Hu, Y.; Ye, X.; Wang, J.; Ding, T. Application of Atmospheric Cold Plasma-Activated Water (PAW) Ice for Preservation of Shrimps (*Metapenaeus ensis*). *Food Control* **2018**, *94*, 307–314. [CrossRef]
29. Vaka, M.R.; Sone, I.; Álvarez, R.G.; Walsh, J.L.; Prabhu, L.; Sivertsvik, M.; Fernández, E.N. Towards the Next-Generation Disinfectant: Composition, Storability and Preservation Potential of Plasma Activated Water on Baby Spinach Leaves. *Foods* **2019**, *8*, 692. [CrossRef]
30. Lin, C.M.; Chu, Y.C.; Hsiao, C.P.; Wu, J.S.; Hsieh, C.W.; Hou, C.Y. The Optimization of Plasma-Activated Water Treatments to Inactivate Salmonella Enteritidis (ATCC 13076) on Shell Eggs. *Foods* **2019**, *8*, 520. [CrossRef]
31. Zhao, Y.; Chen, R.; Tian, E.; Liu, D.; Niu, J.; Wang, W.; Qi, Z.; Xia, Y.; Song, Y.; Zhao, Z. Plasma-Activated Water Treatment of Fresh Beef: Bacterial Inactivation and Effects on Quality Attributes. *IEEE Trans. Radiat. Plasma Med. Sci.* **2020**, *4*, 113–120. [CrossRef]
32. Li, L.; Jiang, J.; Li, J.; Shen, M.; He, X.; Shao, H.; Dong, Y. Effects of Cold Plasma Treatment on Seed Germination and Seedling Growth of Soybean. *Sci. Rep.* **2014**, *4*, 5859. [CrossRef]
33. Park, D.P.; Davis, K.; Gilani, S.; Alonzo, C.A.; Dobrynin, D.; Friedman, G.; Fridman, A.; Rabinovich, A.; Fridman, G. Reactive Nitrogen Species Produced in Water by Non-Equilibrium Plasma Increase Plant Growth Rate and Nutritional Yield. *Curr. Appl. Phys.* **2013**, *13* (Suppl. 1), S19–S29. [CrossRef]
34. Zaplotnik, R.; Kregar, Z.; Bišćan, M.; Vesel, A.; Cvelbar, U.; Mozetič, M.; Milošević, S. Multiple vs. Single Harmonics AC-Driven Atmospheric Plasma Jet. *Europhys. Lett.* **2014**, *106*, 25001. [CrossRef]
35. Zaplotnik, R.; Bišćan, M.; Kregar, Z.; Cvelbar, U.; Mozetič, M.; Milošević, S. Influence of a Sample Surface on Single Electrode Atmospheric Plasma Jet Parameters. *Spectrochim. Acta Part B Spectrosc.* **2015**, *103–104*, 124–130. [CrossRef]
36. Gierczik, K.; Vukušić, T.; Kovács, L.; Székely, A.; Szalai, G.; Milošević, S.; Kocsy, G.; Kutasi, K.; Galiba, G. Plasma-Activated Water to Improve the Stress Tolerance of Barley. *Plasma Process. Polym.* **2020**, *17*, 1900123. [CrossRef]
37. Romanjek Fajdetić, N.; Benković-Lačić, T.; Mirosavljević, K.; Antunović, S.; Benković, R.; Rakić, M.; Milošević, S.; Japundžić-Palenkić, B. Influence of Seed Treated by Plasma Activated Water on the Growth of *Lactuca sativa* L. *Sustainability* **2022**, *14*, 16237. [CrossRef]
38. Kutasi, K.; Bencs, L.; Tóth, Z.; Milošević, S. The Role of Metals in the Deposition of Long-Lived Reactive Oxygen and Nitrogen Species into the Plasma-Activated Liquids. *Plasma Process. Polym.* **2023**, *20*, 2200143. [CrossRef]
39. Oehmigen, K.; Hähnel, M.; Brandenburg, R.; Wilke, C.; Weltmann, K.D.; Von Woedtke, T. The Role of Acidification for Antimicrobial Activity of Atmospheric Pressure Plasma in Liquids. *Plasma Process. Polym.* **2010**, *7*, 250–257. [CrossRef]
40. Lukes, P.; Dolezalova, E.; Sisrova, I.; Clupek, M. Aqueous-Phase Chemistry and Bactericidal Effects from an Air Discharge Plasma in Contact with Water: Evidence for the Formation of Peroxynitrite through a Pseudo-Second-Order Post-Discharge Reaction of H_2O_2 and HNO_2. *Plasma Sources Sci. Technol.* **2014**, *23*, 015019. [CrossRef]
41. Zhang, Z.; Xu, Z.; Cheng, C.; Wei, J.; Lan, Y.; Ni, G.; Sun, Q.; Qian, S.; Zhang, H.; Xia, W.; et al. Bactericidal Effects of Plasma Induced Reactive Species in Dielectric Barrier Gas–Liquid Discharge. *Plasma Chem. Plasma Process.* **2017**, *37*, 415–431. [CrossRef]
42. Hansch, M.A.C.; Mann, M.; Weltmann, K.D.; Von Woedtke, T. Analysis of Antibacterial Efficacy of Plasma-Treated Sodium Chloride Solutions. *J. Phys. D Appl. Phys.* **2015**, *48*, 454001. [CrossRef]
43. *EPA Method 6020A*; Inductively Coupled Plasma-Mass Spectrometry. U.S. EPA Office of Solid Waste (OSW) Methods Team: Washington, DC, USA, 2007.
44. Erkmen, O.; Bozoglu, T.F. *Food Microbiology: Principles into Practice*; John Wiley & Sons: West Sussex, UK, 2016; pp. 17–34.

45. Khlyustova, A.; Labay, C.; Machala, Z.; Ginebra, M.P.; Canal, C. Important Parameters in Plasma Jets for the Production of RONS in Liquids for Plasma Medicine: A Brief Review. In *Frontiers of Chemical Science and Engineering*; Higher Education Press: Beijing, China, 2019; pp. 238–252. [CrossRef]
46. Liang, Q.; Brocks, G.; Bieberle-Hütter, A. Oxygen Evolution Reaction (OER) Mechanism under Alkaline and Acidic Conditions. *J. Phys. Energy* **2021**, *3*, 026001. [CrossRef]
47. Ma, R.N.; Feng, H.Q.; Liang, Y.D.; Zhang, Q.; Tian, Y.; Su, B.; Zhang, J.; Fang, J. An Atmospheric-Pressure Cold Plasma Leads to Apoptosis in Saccharomyces Cerevisiae by Accumulating Intracellular Reactive Oxygen Species and Calcium. *J. Phys. D Appl. Phys.* **2013**, *46*, 285401. [CrossRef]
48. Kim, G.J.; Kim, W.; Kim, K.T.; Lee, J.K. DNA Damage and Mitochondria Dysfunction in Cell Apoptosis Induced by Nonthermal Air Plasma. *Appl. Phys. Lett.* **2010**, *96*, 021502. [CrossRef]
49. Zhou, R.; Zhou, R.; Zhuang, J.; Zong, Z.; Zhang, X.; Liu, D.; Bazaka, K.; Ostrikov, K. Interaction of Atmospheric-Pressure Air Microplasmas with Amino Acids as Fundamental Processes in Aqueous Solution. *PLoS ONE* **2016**, *11*, e0155584. [CrossRef]
50. Dolezalova, E.; Lukes, P. Membrane Damage and Active but Nonculturable State in Liquid Cultures of Escherichia Coli Treated with an Atmospheric Pressure Plasma Jet. *Bioelectrochemistry* **2015**, *103*, 7–14. [CrossRef]
51. Lukes, P.; Locke, B.R.; Brisset, J.-L. 7 Aqueous-Phase Chemistry of Electrical Discharge Plasma in Water and in Gas-Liquid Environments. *Plasma Chem. Catal. Gases Liq.* **2012**, *1*, 243–308.
52. Bruggeman, P.J.; Kushner, M.J.; Locke, B.R.; Gardeniers, J.G.E.; Graham, W.G.; Graves, D.B.; Hofman-Caris, R.C.H.M.; Maric, D.; Reid, J.P.; Ceriani, E.; et al. Plasma-Liquid Interactions: A Review and Roadmap. *Plasma Sources Sci. Technol.* **2016**, *25*, 053002. [CrossRef]
53. Arroyo, G.; Sanz, P.D.; Pré Stamo, G. Response to High-Pressure, Low-Temperature Treatment in Vegetables: Determination of Survival Rates of Microbial Populations Using Flow Cytometry and Detection of Peroxidase Activity Using Confocal Microscopy. *J. Appl. Microbiol.* **1999**, *86*, 544. [CrossRef]
54. Zhao, Y.M.; Ojha, S.; Burgess, C.M.; Sun, D.W.; Tiwari, B.K. Inactivation Efficacy of Plasma-Activated Water: Influence of Plasma Treatment Time, Exposure Time and Bacterial Species. *Int. J. Food Sci. Technol.* **2021**, *56*, 721–732. [CrossRef]
55. Laroussi, M.; Mendis, D.A.; Rosenberg, M. Plasma Interaction with Microbes. *New J. Phys.* **2003**, *5*, 41. [CrossRef]
56. Kamgang-Youbi, G.; Herry, J.M.; Meylheuc, T.; Brisset, J.L.; Bellon-Fontaine, M.N.; Doubla, A.; Naïtali, M. Microbial Inactivation Using Plasma-Activated Water Obtained by Gliding Electric Discharges. *Lett. Appl. Microbiol.* **2009**, *48*, 13–18. [CrossRef]
57. Ercan, U.K.; Smith, J.; Ji, H.F.; Brooks, A.D.; Joshi, S.G. Chemical Changes in Nonthermal Plasma-Treated N-Acetylcysteine (NAC) Solution and Their Contribution to Bacterial Inactivation. *Sci. Rep.* **2016**, *6*, 20365. [CrossRef]
58. Ursache, M.; Moraru, R.; Hnatiuc, E.; Nastase, V.; Mares, M. Comparative Assessment of the Relation between Energy Consumption and Bacterial Burden Reduction Using Plasma Activated Water. In Proceedings of the 2014 International Conference on Optimization of Electrical and Electronic Equipment (OPTIM), Cheile Gradistei, Romania, 22–24 May 2014; IEEE: New York, NY, USA, 2014; pp. 1036–1041. [CrossRef]
59. Liu, F.; Sun, P.; Bai, N.; Tian, Y.; Zhou, H.; Wei, S.; Zhou, Y.; Zhang, J.; Zhu, W.; Becker, K.; et al. Inactivation of Bacteria in an Aqueous Environment by a Direct-Current, Cold-Atmospheric-Pressure Air Plasma Microjet. *Plasma Process. Polym.* **2010**, *7*, 231–236. [CrossRef]
60. Ryu, Y.H.; Kim, Y.H.; Lee, J.Y.; Shim, G.B.; Uhm, H.S.; Park, G.; Choi, E.H. Effects of Background Fluid on the Efficiency of Inactivating Yeast with Non-Thermal Atmospheric Pressure Plasma. *PLoS ONE* **2013**, *8*, e66231. [CrossRef]
61. Xiang, Q.; Kang, C.; Niu, L.; Zhao, D.; Li, K.; Bai, Y. Antibacterial Activity and a Membrane Damage Mechanism of Plasma-Activated Water against Pseudomonas Deceptionensis CM2. *LWT* **2018**, *96*, 395–401. [CrossRef]
62. Vione, D.; Maurino, V.; Minero, C.; Borghesi, D.; Lucchiari, M.; Pelizzetti, E. New Processes in the Environmental Chemistry of Nitrite. 2. The Role of Hydrogen Peroxide. *Environ. Sci. Technol.* **2003**, *37*, 4635–4641. [CrossRef]

Apoptosis time window induced by cold atmospheric plasma: comparison with ionizing radiation

Gordana Joksić[1,]*, Ana Valenta Šobot[1], Jelena Filipović Tričković[1], Dejan Maletić[2], Nevena Puač[2], Gordana Malović[2], Zoran Lj. Petrović[2] and Saša Lazović[2]

[1]Department of Physical Chemistry,
Vinca Institute of Nuclear Sciences, University of Belgrade,
Mike Petrovica Alasa 12-14, 11001 Belgrade, Serbia
[2]Institute of Physics, University of Belgrade, Pregrevica 118,
11080 Belgrade, Serbia

In this study we evaluate apoptosis time window of primary fibroblasts treated with cold atmospheric plasma (CAP), power range 0.4–1.4 W, for 30 sec, using γ-H2AX phosphorylation assay and flow cytometry. In contrast to irradiation where maximum of γ-H2AX foci appeared 30 min after irradiation and apoptosis 24 h later irrespective of radiation dose, treatment with CAP (power of 0.4 and 0.6) induces maximum of γ-H2AX foci 2 h after treatment. Apoptosis occurred in a power-dependent manner, with time shift of 2–3 h. Besides power-dependent time shift in apoptosis induction, apoptosis time window is the same and lasts for 2 h.

Keywords: Apoptosis, cold atmospheric plasma, ionizing radiation, primary human fibroblasts, repair kinetics.

DOUBLE strand breaks (DSBs) represent the most significant damage of the DNA. In complex reactions between stressor, cellular DNA and repair processes, DNA lesion may be repaired back to the original state, or miss-repaired making chromosomal aberrations or inducing the frame of chromatin structure to activate other cell functions beyond canonical DNA damage response.

Phosphorylated histone H2AX (namely γ-H2AX) represents the first signal molecule in the pathway that activates DSBs repair[1]. The role of γ-H2AX foci is to amplify DSB signalling to facilitate cell-cycle arrest at distinct points of the cycle, consecutively enabling sufficient time for repair, namely to prevent entry of damaged cells into mitosis[2]. During the arrest, cells either activate a cascade of proteins needed to complete repair or commit suicide by apoptosis. Phosphorylation of histone H2AX takes place in both processes[3,4], representing a universal cellular response to DSBs. Although a body of evidence shows that DSBs could occur after exposure to different exogenous agents, it has also been reported that their molecular structure could be very complex and is strongly relates to their origin, suggesting that their repair and final fate of cell survival could be strictly related to their complexity[5,6].

Cold atmospheric plasma (CAP) produces different kinds of reactive oxygen and nitrogen species (hydroxyl radical ($^\bullet$OH), hydrogen peroxide (H_2O_2), ozone (O_3), atomic oxygen (O), superoxide anion (O_2^-), nitric oxide (NO) and peroxynitrite ($ONOO^-$)), consequently triggering various signalling pathways, including DNA repair, cell cycle control, apoptosis and other types of cell death[7,8]. In the present study, CAP was generated in a mixture of helium and surrounding air in order to produce reactive oxygen and nitrogen species that play an important role in the plasma–cell interactions. The NO species are generated in the gas phase through several different reaction pathways, including direct reactions involving atomic oxygen and nitrogen atoms, or nitrogen molecule and oxygen atoms. The formation of peroxynitrite is possible through several reaction pathways depending on the experimental conditions. It can be formed through reaction of nitrates with hydrogen peroxide or in the reactions with O_2^- and $OH^{\bullet -}$ (refs 9–11).

Our previous work has shown that the effects of plasma doses can be tuned to match the typical therapeutic doses of ionizing radiation, inducing mainly apoptosis of human primary cells[12]. In this study, we have used previously established experimental conditions to further examine the repair kinetics of plasma-induced DSBs as well as to get an approximate estimate of the time window when apoptotic outcome of the cells occurs. Repair kinetics was assessed using γ-H2AX phosphorylation assay and, in parallel, apoptosis was assessed by flow cytometry. The level of lipid peroxidation was also monitored.

Primary fibroblasts were obtained from skin biopsies of three healthy volunteers undergoing plastic surgery. All subjects signed informed consents regarding this study, which conformed to the Declaration of Helsinki and was approved by the Ethical Committee of the Vinca Institute of Nuclear Sciences, Belgrade, Serbia. A total of three primary fibroblast cell lines were established. Cells were grown in Chang Amnio medium (Irvine Scientific, USA) at 37°C in a humid atmosphere and 10% of CO_2. Each sample was set up in duplicate: one set was used for γ-irradiation while the other set was used for plasma treatment.

As shown in Figure 1, the plasma needle was placed above the samples and powered at 13.56 MHz. Helium flow rate of 1 SLM (standard litre per minute) was used for all treatments. Derivative probes were used to measure the power delivered to the plasma. Grounded electrode made of copper foil was placed beneath the sample-containing vessel. The distance between the needle tip and the samples was 5 mm. Plasma power of 0.4, 0.6 and 1.4 W was used in the experiment. Treatment duration was 30 sec for all three applied powers under standard laboratory conditions, i.e. relative humidity of 50% and

---

*For correspondence. (e-mail: gjoksic@vin.bg.ac.rs)

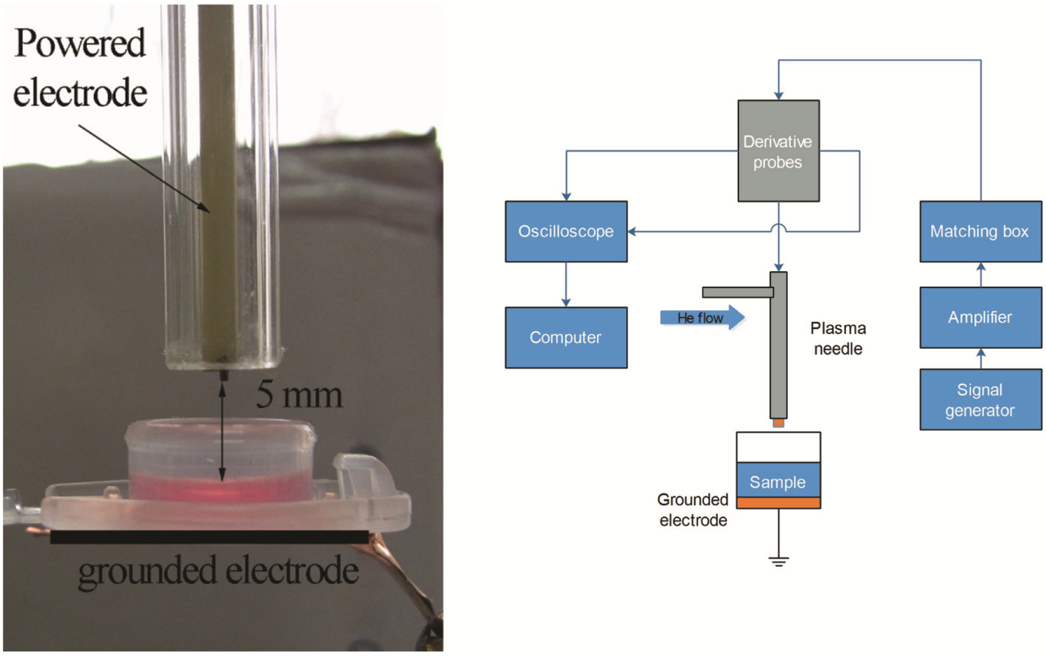

Figure 1. Plasma treatment experimental set-up: photograph and schematic diagram.

temperature of 23°C. The monolayer of cells was covered with 5 μl of Chang medium; then the cells were placed in an incubator for recovery. To assess the repair kinetics of induced damage slides were processed on different incubation times employing the γ-H2AX phosphorylation assays.

Samples were irradiated using ^{60}Co γ-ray source (the most explored therapeutic dose of 2 Gy at a dose rate 0.45 Gy/min). The dimensions of the radiation field were 20 × 20 cm and distance from the source was 74 cm. After irradiation, cells were returned to the tissue culture incubator, and processed according to the method of Rogakou *et al.*[13]. Thereafter, the cells were placed in an incubator for recovery. Slides were processed on different incubation times after the treatment (30 min, 2 h, 5 h and 24 h) employing γ-H2AX phosphorylation assay. Parallel samples were used for flow cytometry and lipid peroxidation analysis.

For immunostaining, exponentially growing cells were seeded on polylysine glass slides (Sigma-Aldrich, USA) and allowed to attach to the slide surface for 24 h before treatment with ionizing radiation or cold plasma. At various time points after the treatment (30 min, 2 h, 5 h and 24 h), the cells were fixed in 4% formaldehyde, permeabilized with 0.2% Triton X-100 and stained with the γ-H2AX primary antibody (Merck Millipore, USA) and a FITC-labelled secondary antibody (Sigma-Aldrich, USA). The slides were mounted with 4′,6′-diamidino-2-phenylindole (DAPI)-containing Vectashield solution (Vector Laboratories Ltd, UK), covered with coverslips and sealed. Foci positive for γ-H2AX were counted using an epifluorescent Axiomager A1 microscope (Carl Zeiss, Germany) and the computer software ISIS (Metasystem, Germany), according to the method of Kinner *et al.*[14].

For apoptosis assay, at each time point after irradiation and plasma treatment, cells were washed with pre-warmed phosphate buffer saline (PBS) at 37°C and fixed in 96% ethanol. Apoptosis was monitored by flow cytometry (Becton Dickinson, Germany). DNA content was assessed by measuring the UV fluorescence of propidium iodide-stained DNA (PI, 10 mg/ml, Sigma-Aldrich, USA). Apoptotic population and cell cycle analysis was performed using CellQuest software (Becton Dickinson, Germany), according to the method of Holmes *et al.*[15].

For lipid peroxidation by measuring thiobarbituric acid reactive substances (TBARS) spectrophotometrically, we followed the method of Janero[16]: 0.1 ml of pellet and 0.1 ml of medium of the same culture were used for analysis. Briefly, 0.4 ml of 50 mM *Tris*-HCl buffer containing 180 mM KCl and 10 mM EDTA was added to 0.1 ml of pellet lysate or defrosted medium, 0.5 ml of 2-thiobarbituric acid (Merck; 1 wt%/vol) in 0.05 M NaOH and 0.5 ml of HCl (25 wt%/vol in water). The mixture was heated in boiling water for 10 min, reaction was stopped by cooling samples on ice, and thereafter the chromogen was extracted in 3 ml of *n*-butanol in the organic phase separated by centrifugation at 5000 rpm for 10 min. The absorbance of the organic phase was measured spectrophotometrically (Tecan Sunrise absorbance microplate reader, Tecan Group Ltd, Switzerland) at 532 nm wavelength. The amount of lipid peroxidation was expressed as nmol of TBARS (malondialdehide, MDA equivalents)/mg of proteins, using a standard curve of 1,1,3,3-tetramethoxypropane. Proteins were

Table 1. Repair kinetics and apoptosis of human primary fibroblasts exposed to non-thermal plasma and ionizing radiation

Treatment	Analysis	0 min	0.5 h	2 h	5 h	24 h
Ionizing radiation	Number of f/c[a]	0.39	19.79	14.53	5.23	1.12
	% of >60 f/c	0.41	8.89	3.47	1.86	0.16
	% of apoptotic cells	9.1	37.25	33.42	25.16	51.51
	MDA[b] (nmol/mg of proteins)	0.54	0.68	0.55	0.33	0.67
CAP[c] power of 0.4 W	Number of f/c	1.39	16.22	39.85	21.8	0.16
	% of >60 f/c	0	1.72	3.9	2.85	0.59
	% of apoptotic cells	8.22	14.43	41.8	31.4	5.82
	MDA (nmol/mg of proteins)	0.54	0.68	0.69	0.8	0.67
CAP power of 0.6 W	Number of f/c	0.4	46.59	47.59	29.27	7.35
	% of >60 f/c	0	42.65	84.9	11.45	0
	% of apoptotic cells	9.14	58.5	68.14	27	0
	MDA (nmol/mg of proteins)	0.59	0.81	0.88	0.74	0.92
CAP power of 1.4 W	Number of f/c	4	13.55	7.88	0	0
	% of >60 f/c	0	36.15	76.08	0	0
	% of apoptotic cells	9.4	36.1	68	0	0
	MDA (nmol/mg of proteins)	0.79	1.47	1.45	1.23	1.3

[a]f/c, γ-H2AX focus per cell. [b]MDA, Malondialdehyde. [c]CAP, Cold atmospheric plasma.

determined according to Lowry *et al.*[17] using bovine serum albumin as standard.

Statistical analysis was performed using SPSS 10 for Windows. Differences between the groups were assessed using nonparametric Mann Whitney *U* test, while correlation between different parameters was assessed by Pearson correlation. Differences at $P < 0.05$ were accepted as the level of significance.

Table 1 and Figure 2 present results obtained in the experiment where cells were directly exposed to non-thermal plasma.

Previously established experimental parameters such as power delivered to plasma of 0.4, 0.6 and 1.4 W and exposure time of 30 sec, were used to study repair kinetics of DSBs (visualized by γ-H2AX histone), apoptosis and lipid peroxidation biomarker – MDA at different recovery periods after treatment. Results were compared with the effects of γ-rays (^{60}Co) – acute irradiation. The power of 0.4, 0.6 and 1.4 W corresponds to voltage 337, 357 and 393 V respectively. At exposure time of 30 sec calculated corresponding equivalent radiation dose ranged from 0.96 (0.4 W and 30 sec) to 2.2 Gy (ref. 12).

The baseline level of γ-H2AX in unexposed control cells was 3.9 per cell, whereas 30 min after plasma treatment (power of 0.4 W), the yield of γ-H2AX reached 16.2 foci per cell. Further increase in power (0.6 W) induced 46.6 foci per cell, whereas power of 1.4 W momentarily induced cell death seen as misshapen nuclei (Figure 2 *a* and *b*) or as a 'track' (Figure 2 *a*) where all the cells closest to the powered electrode were detached from the polylysine surface.

A maximum of foci induction after non-thermal plasma treatment with power of 0.4 and 0.6 W occurred 2 h after treatment (1.5 h later when compared with ionizing radiation), indicating that most of the treated cells will die via apoptosis (Table 1). Initial DNA damages are non-reparable and determine early apoptosis. This observation was confirmed by flow cytometry data, which showed that apoptosis occurred in a dose (power)-dependent manner, i.e. the highest power induced necrosis, power of 0.6 W induced apoptosis with maximum between 30 min and 2 h after treatment; whereas 0.4 W induced apoptosis 2 h after exposure and last continuously for up to 5 h (Table 1). Interestingly, besides power-dependent time shift in apoptosis induction, apoptosis time window was the same and lasted for 2 h.

A positive correlation between the number of cells carrying 60 signals per cell and percentage of cells displaying apoptotic granulation was found for cold plasma treatments with power of 0.4 and 0.6 W (Pearson correlation, $P < 0.01$, $r = 0.967$ and $P < 0.05$, $r = 0.934$ respectively). In samples treated with power of 1.4 W, high number of misshapen nuclei was observed, as well as elevated concentration of MDA. Bulky phosphorylation of γ-H2AX seen as more than 60 signals per nuclei, correlates with apoptotic fragmentation. It has been previously reported that H2AX phosphorylation that leads to apoptosis mainly occurred by DNA-PKcs[4], although phosphorylation of H2AX via c-Jun N terminal kinases (JNK) cannot be neglected due to UV irradiation in plasma source. However, DNA-PKcs are predominant kinases that phosphorylate H2AX when irrepairable lesions are induced, activating apoptosis, as revealed by the normal fibroblast cell lines that we used in the experiment. In cells irradiated with ionizing radiation, phosphorylation of H2AX occurs via ATM kinase that leads to activation of cascade molecules involved in DSBs repair. H2AX is the most important molecule in a switch between apoptosis versus repair response following DNA damage[18,19]. According to the results obtained in this

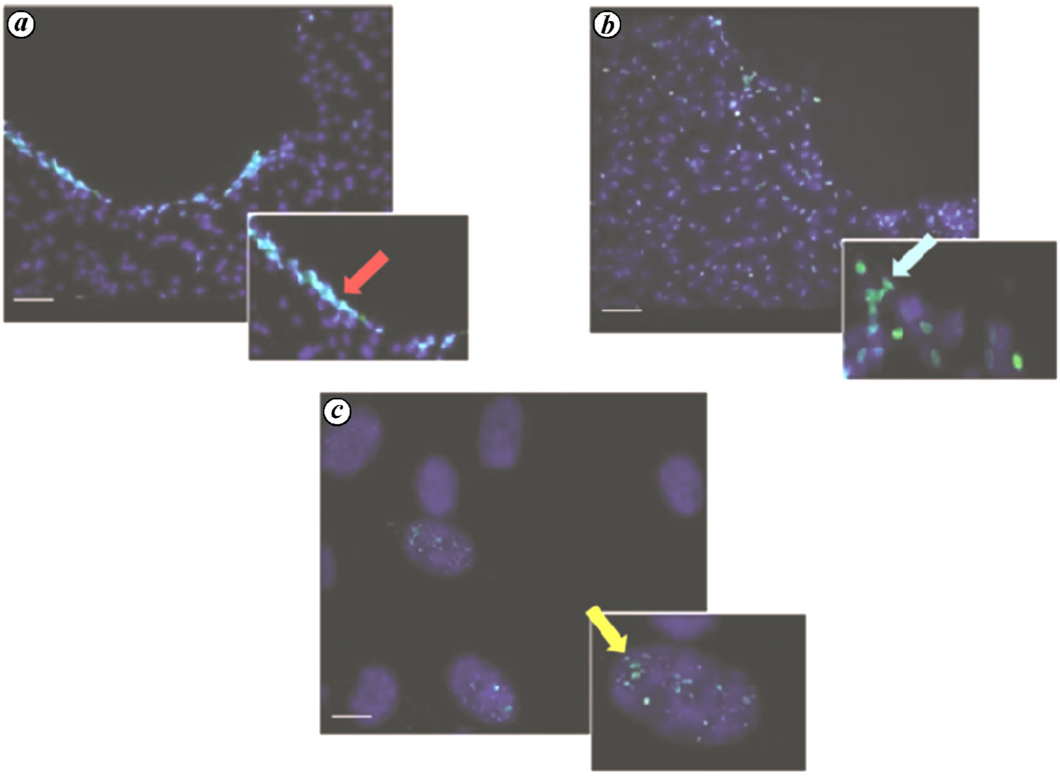

Figure 2. Photomicrographs of plasma and ionizing radiation-treated cells visualized by immunostaining. ***a***, ***b***, Cold plasma-treated samples, power 1.4 W. In (***a***), red arrow indicates detached cells seen as a 'track'. In (***b***), blue arrow indicates FITC-labelled necrotic cells; scale bar = 150 μm. ***c***, Ionizing radiation-treated cells. Yellow arrow indicates γ-H2AX foci in FITC-labelled cells; scale bar = 30 μm.

study, we can conclude that non-thermal atmospheric plasma power (0.4–0.6 W) predominantly induces apoptosis, whereas power of 1.4 W predominantly induces necrosis (Figure 2 *a* and *b*).

Treatment with ionizing radiation (^{60}Co γ-rays) induces maximum γ-H2AX foci formation 30 min after irradiation, 19.79 (Table 1, Figure 2 *c*). Induced DSBs are mostly repaired within 24 h. During recovery period, a portion of cells undergoes unsuccessful repair outcome, and is removed from the population via apoptosis. Apoptosis starts 30 min after irradiation (37.25%) and continuously occurs during the next 5 h almost at the same extent, suggesting that all cells that enter the S-phase of the cell cycle with unrepaired DSBs are directed towards apoptosis. The maximum pick of apoptosis takes place 24 h after irradiation (51.51%), restoring γ-H2AX foci mostly to the baseline level. Residual foci, after recovery period of 24 h, are the main side effects after irradiation with ionizing radiation, because unrepaired DSBs can interact with other lesions creating hybrid genes, deletion or duplication that can lead to genomic instability and transformation of cells[8,20].

In contrast to ionizing radiation, treatment with cold plasma power of 0.4 and 0.6 W induces maximum formation of γ-H2AX foci 2 h after treatment, accompanied by massive apoptosis of treated cells (Table 1). The highest power (1.4 W) induces necrosis of cells, characterized with misshapen, sparkling, partly detached nuclei, as seen microscopically. MDA levels were also elevated in these cells; they were statistically significant compared with other treatments ($P < 0.05$), indicating increased lipid peroxidation (Table 1). Lipid peroxidation, depending on its extent, may endorse cellular survival or lead to cell death. High peroxidation rates that overcome repair capacities result in cell death[21,22], which, accompanied with exhausted energetic capacities, directs cells to necrosis[23]. After recovery period of 24 h, the number of cells surviving after treatment with non-thermal plasma power of 1.4 W is low, suggesting that initially induced bulky lesions determine lethal fate of treated cells.

Non-thermal plasma is a promising method to be used for treatment of small tissue areas. The results of this study strongly indicate that non-thermal plasma treatment in the power range 0.4–0.6 W induces apoptosis, whereas further increase in power induces massive irreparable lesions which lead to necrosis. Power-dependent time shift in apoptosis is observed, while apoptosis time window remains the same and lasts for 2 h. Further studies on non-thermal plasma should be directed towards examining the possible bystander effects on the surroundings of target tissues, since extracellular liquid of treated tissues carries newly produced chemical compounds that can be stable for certain periods of time and induce adverse effects to the surrounding tissues acting as chemical messengers.

Conflict of interest: The authors declare no conflicts of interest.

1. Downs, J. A., Lowndes, N. F. and Jackson, S. P., A role for *Saccharomyces cerevisiae* histone H2A in DNA repair. *Nature*, 2000, **408**, 1001–1004.
2. Downs, J. A. *et al.*, Binding of chromatin-modifying activities to phosphorylated histone H2A at DNA damage sites. *Mol. Cell*, 2004, **16**, 979–990.
3. Rogakou, E. P., Nieves-Neira, W., Boon, C., Pommier, Y. and Bonner, W. M., Initiation of DNA fragmentation during apoptosis induces phosphorylation of H2AX histone at serine 139. *J. Biol. Chem.*, 2000, **275**, 9390–9395.
4. Yuan, J., Adamski, R. and Chen, J., Focus on histone variant H2AX: to be or not to be. *FEBS Lett.*, 2010, **584**, 3717–3724.
5. Schipler, A. and Iliakis, G., DNA double-strand break complexity levels and their possible contributions to the probability for error-prone processing and repair pathway choice. *Nucleic Acids Res.*, 2013, **41**, 7589–7605.
6. Shibata, A. *et al.*, Factors determining DNA double-strand break repair pathway choice in G2 phase. *EMBO J.*, 2011, **30**, 1079–1092.
7. Dezest, M. *et al.*, Mechanistic insights into the impact of cold atmospheric pressure plasma on human epithelial cell lines. *Sci. Rep.*, 2017, **7**, 41163.
8. Noda, A., Radiation-induced unrepairable DSBs: their role in the late effects of radiation and possible applications to biodosimetry. *J. Radiat. Res.*, 2018, **59**, ii114–ii120.
9. Bruggeman, P. J. *et al.*, Plasma–liquid interactions: a review and roadmap. *Plasma Sources Sci. Technol.*, 2016, **25**, 053002.
10. Lukes, P., Dolezalova, E., Sisrova, I. and Clupek, M., Aqueous-phase chemistry and bactericidal effects from an air discharge plasma in contact with water: evidence for the formation of peroxynitrite through a pseudo-second-order post-discharge reaction of H_2O_2 and HNO_2. *Plasma Sources Sci. Technol.*, 2014, **23**, 015019.
11. Seth, A. N., Wei, T., Eric, J. and Mark, J. K., Atmospheric pressure plasma jets interacting with liquid covered tissue: touching and not-touching the liquid. *J. Phys. D*, 2014, **47**, 475203.
12. Lazović, S. *et al.*, Plasma induced DNA damage: comparison with the effects of ionizing radiation. *Appl. Phys. Lett.*, 2014, **105**, 124101.
13. Rogakou, E. P., Pilch, D. R., Orr, A. H., Ivanova, V. S. and Bonner, W. M., DNA double-stranded breaks induce histone H2AX phosphorylation on serine 139. *J. Biol. Chem.*, 1998, **273**, 5858–5868.
14. Kinner, A., Wu, W., Staudt, C. and Iliakis, G., Gamma-H2AX in recognition and signaling of DNA double-strand breaks in the context of chromatin. *Nucleic Acids Res.*, 2008, **36**, 5678–5694.
15. Holmes, K. L., Otten, G. and Yokoyama, W. M., Flow cytometry analysis using the Becton Dickinson FACS Calibur. In *Current Protocols in Immunology* (eds Coligan, J. E. *et al.*), John Wiley, USA, 2002, vol. 49, pp. 5.4.1–5.4.22.
16. Janero, D. R., Malondialdehyde and thiobarbituric acid-reactivity as diagnostic indices of lipid peroxidation and peroxidative tissue injury. *Free Radic. Biol. Med.*, 1990, **9**, 515–540.
17. Lowry, O. H., Rosebrough, N. J., Farr, A. L. and Randall, R. J., Protein measurement with the Folin phenol reagent. *J. Biol. Chem.*, 1951, **193**, 265–275.
18. Cook, P. J., Ju, B. G., Telese, F., Wang, X., Glass, C. K. and Rosenfeld, M. G., Tyrosine dephosphorylation of H2AX modulates apoptosis and survival decisions. *Nature*, 2009, **458**, 591.
19. Xiao, A. *et al.*, WSTF regulates the H2AX DNA damage response via a novel tyrosine kinase activity. *Nature*, 2009, **457**, 57–62.
20. Fenech, M., The cytokinesis-block micronucleus technique: a detailed description of the method and its application to genotoxicity studies in human populations. *Mutat. Res.*, 1993, **285**, 35–44.
21. Ayala, A., Munoz, M. F. and Arguelles, S., Lipid peroxidation: production, metabolism, and signaling mechanisms of malondialdehyde and 4-hydroxy-2-nonenal. *Oxid. Med. Cell. Longev.*, 2014, **2014**, 360438.
22. Haghdoost, S., Sjolander, L., Czene, S. and Harms-Ringdahl, M., The nucleotide pool is a significant target for oxidative stress. *Free Radic. Biol. Med.*, 2006, **41**, 620–626.
23. Vairetti, M., Ferrigno, A., Bertone, R., Richelmi, P., Berte, F. and Freitas, I., Apoptosis vs necrosis: glutathione-mediated cell death during rewarming of rat hepatocytes. *Biochim. Biophys. Acta*, 2005, **1740**, 367–374.

ACKNOWLEDGEMENTS. We thank Dr Miroslav Demajo, Vinca Institute of Nuclear Science University of Belgrade for critically reading the manuscript. This work is financially supported by the Ministry of Education, Science and Technological Development of the Republic of Serbia, Grant No. 173046.

Received 5 October 2018; revised accepted 27 December 2018

doi: 10.18520/cs/v116/i7/1229-1233

Indole-3-acetic acid production by the cyanobacterium *Fisherella muscicola* NDUPC001

S. K. Mishra, Jyoti Singh, Astha Raj Pandey and N. Dwivedi*

Department of Botany, U.P. College (Autonomous),
Varanasi 221 002, India

Fisherella muscicola* NDUPC001 was isolated from agricultural fields of Varanasi, India. The cyanobacterial strain was characterized by morphological as well as molecular methods (16S rRNA gene with accession no. JX876898.2) and was deposited at NAIMCC (NBAIM), Mau, Uttar Pradesh, India (accession no. NAIMCC-C-000121). The cyanobacterial strain produced tryptophan-dependent indole-3-acetic acid (IAA), which was identified by thin-layer chromatography and quantitative determination was done by Salkowski's colorimetric method. The maximum amount of IAA production was 286.82 μg/ml on the 19th day in culture medium supplemented with 5 mg/ml of L-tryptophan. The cyanobacterial extract increased the length of radicle, plumule and number of adventitious roots of rice several times in comparison to control to state the IAA production by *Fisherel-

---

*For correspondence. (e-mail: drnagendra.dwivedi@gmail.com)